JAN KOCHANOWSKI UNIVERSITY

DOCTORAL SCHOOL

FACULTY OF NATURAL SCIENCES

PHYSICAL SCIENCES

HARADHAN ADHIKARY

CERN-THESIS-2023-378
10/04/2024

SEARCH FOR THE CRITICAL POINT OF STRONGLY INTERACTING MATTER

(PROTON INTERMITTENCY ANALYSIS BY NA61/SHINE AT CERN SPS)

Doctoral dissertation written
under the supervision of
prof. dr hab. Marek Gazdzicki

KIELCE 2023

This doctoral thesis was prepared within the research project of the MAESTRO grant financed by the National Science Centre, Poland, under grant no. 2018/30/A/ST2/0026 and in collaboration with the NA61/SHINE Collaboration at the CERN SPS

© Copyright by HARADHAN ADHIKARY, 2023
All Rights Reserved

Dedication

To my brother, Late Sudip Mukherjee, whom I lost due to COVID-19 during the Pandemic.
His constant selfless support was the driving force behind my Ph.D. journey.

ACKNOWLEDGMENT

I am deeply grateful to my supervisor, Prof. dr. hab. Marek Gazdzicki, for his unwavering support, guidance, and endless patience throughout my doctoral studies. His dedication to imparting essential skills and knowledge was invaluable, and his contributions were crucial to shaping my research and personal growth.

Equally, my heartfelt appreciation extends to Dr. Tobiasz Czopowicz, who, alongside Marek, has been an unwavering source of support and guidance throughout my Ph.D. studies. Tobiasz's expertise in NA61/SHINE data analysis, particularly in the realm of intermittency analysis, has played a pivotal role in enriching my understanding of the subject. His guidance, from the initial stages to the ultimate culmination of my Ph.D. thesis, has been instrumental in achieving successful completion. His willingness to share his knowledge and assist me in mastering new techniques related to my work has been invaluable throughout my doctoral studies.

Additionally, the inception of this thesis owes much to the NA61/SHINE Collaboration, characterized by fruitful discussions during official meetings and on numerous other occasions. My gratitude goes out to Andrzej Rybicki, Katarzyna Grebieszkow, Peter Seyboth, Nikolaos Davis, Andrey Seryakov, Brant Rumberger, Maciej Lewicki, and other esteemed members of the NA61/SHINE Collaboration. Their rich experience and deep knowledge provided ready solutions for nearly any conceivable problem.

I extend special thanks to Francesco Giacosa, Grzegorz Stefanek, Alicja Wzorek, and Maciej Rybczynski for their consistent support and valuable advice. I appreciate the engaging discussions I shared with Subhasis Samanta, Samrangy Sadhu, Leonardo Tinti, Stanislaw Mrowczyski, and Giorgio Torrieri.

I want to give a shout-out to my friends who smoothened my Ph.D. journey: Shreya Mondal, Shahriyar Jafarzade, Regina Satura, Abhipsa Acherya, Uzair Shah, Ivan Pidhurskyi, Ali Bagzir, Valeria Reyna, Yehor Bondar, Oleksandra Panova, and Tobiasz too.

Lastly, I wish to acknowledge my family's immeasurable support and patience.

SEARCH FOR THE CRITICAL POINT OF STRONGLY INTERACTING MATTER

(PROTON INTERMITTENCY ANALYSIS BY NA61/SHINE AT CERN SPS)

ABSTRACT

Haradhan Adhikary, M.Sc.
Jan Kochanowski University, Kielce
April 2023

Supervisor: prof. dr hab. Marek Gazdzicki

The existence and location of the critical point of strongly interacting matter are objects of both experimental and theoretical studies. As the critical point has properties of the second-order phase transition, it is expected that in its vicinity the system will have special properties. NA61/SHINE approach involves a two-dimensional scan in beam momentum and system size of colliding nuclei, focusing on measuring particle number fluctuations in transverse-momentum space. The study uses second-scaled factorial moments of the multiplicity distribution to quantify these fluctuations and systematically searches for any non-monotonic dependence of the observables on collision energy and nucleus size.

This thesis presents the first results of proton intermittency for central Pb+Pb collisions at 13*A* ($\sqrt{s_{NN}} \approx 5.1$ GeV), 30*A* GeV/*c* ($\sqrt{s_{NN}} \approx 7.6$ GeV), and Ar+Sc collisions at 13*A*, 19*A*, 30*A*, 40*A* and 75*A* GeV/*c* ($\sqrt{s_{NN}} \approx 5.1$-11.9 GeV) recorded by NA61/SHINE at the CERN SPS. The intermittency analysis is performed using both transverse and cumulative transverse momentum, and statistically independent data sets are used for each subdivision number. The results are an important milestone in the search for the critical point of strongly interacting matter.

The presented results do not show evidence for the critical point of strongly interacting matter in the scanned region of the QCD phase diagram. An upper limit on the fraction of critical-proton pairs and the power of the correlation function is obtained based on a comparison with the Power-law Model developed for this purpose. The theoretical background for the critical point and its significance in understanding the phase structure of strongly interacting matter is provided.

POSZUKIWANIE PUNKTU KRYTYCZNEGO SILNIE ODDZIAŁUJĄCEJ MATERII
(ANALIZA INTRMITENCJI PROTONÓW W NA61/SHINE PRZY CERN SPS)

ABSTRAKT

mgr Haradhan Adhikary
Uniwersytet Jana Kochanowskiego w Kielcach
April 2023

Promotor: prof. dr hab. Marek Gazdzicki

Zarówno istnienie punktu krytycznego materii silnie oddziałującej jak i jego położenie są przedmiotem intensywnych badań eksperymentalnych oraz teoretycznych. Eksperyment NA61/SHINE wykonał skan dostępnego obszaru diagramu fazowego przeprowadzając zderzenia różnych jąder (proton-proton, beryl-beryl, argon-skand, ksenon-lantan oraz ołów-ołów) przy różnych pędach wiązki (13*A*–150*A* GeV/*c*, $\sqrt{s_{NN}} \approx$ 5.1–17 GeV). Zebrane dane umożliwiają systematyczne poszukiwanie spodziewanych sygnałów punktu krytycznego poprzez analizę niemonotonicznych zależności obserwowanych wielkości od energii zderzenia i rozmiaru systemu.

Jako że punkt krytyczny ma właściwości przejścia fazowego II rodzaju, oczekuje się, że w jego pobliżu układ będzie przejawiał specjalne właściwości. Jedną z analizowanych wielkości jest liczba wyprodukowanych cząstek w przestrzeni pędu poprzecznego opisana za pomocą skalowanych momentów silni (intermitencja).

Niniejsza praca przedstawia analizę oraz pierwsze wyniki pomiaru intermitencji protonów wyprodukowanych w zderzeniach argon-skand przy pędach wiązki 13*A*, 19*A*, 30*A*, 40*A* oraz 75*A* GeV/*c* zarówno dla pędu poprzecznego, jak i dla kumulatywnego pędu poprzecznego. Prezentowane wyniki stanowią istotny wkład w poszukiwania punktu krytycznego silnie oddziałującej materii. Nie wskaxują one na jego istnienie w badanym obszarze diagramu fazowego QCD, ale dzięki porównaniu z opracowanym w tym celu modelem możliwe było wyznaczenie górnej granicy ilości krytycznych protonów w zależności od siły korelacji.

Contents

Chapter One

Introduction

There are various states of matter. A good example of this is water, which has several different phases we can experience daily. The ice cube is considered to be in a solid state due to its specific characteristics. The state of matter may change or undergo a phase transition when certain characteristics, such as temperature, are altered. The ice cube will dissolve into liquid water when heated.

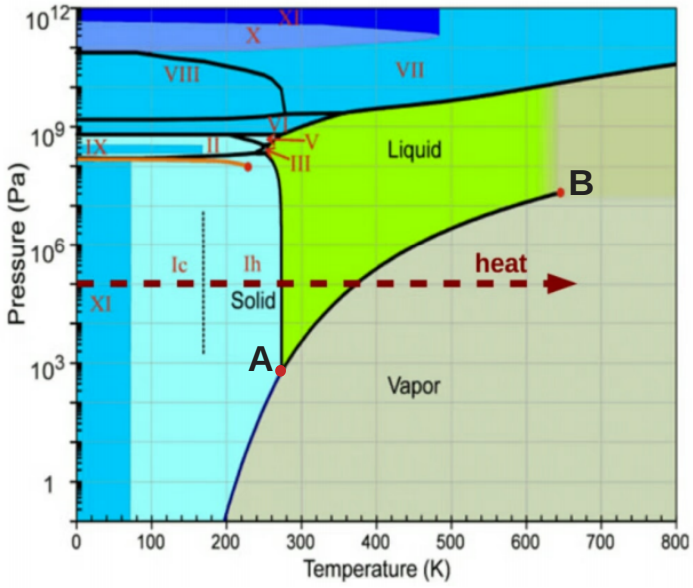

Figure 1.1 The well-known phase diagram of water. One of the important points on this water phase diagram is the critical point, where the difference between the liquid and gas phases disappears, see text for details. The figure is taken from Ref. [1].

The well-known water phase diagram is shown in Fig. 1.1, which depicts phases of water, solid, liquid and vapour, at different pressures and temperatures. Some important points on this

phase diagram include the triple point (denoted by A), where all three phases exist together, and the critical point (CP) (denoted by B), where the distinction between liquid and gas disappears. A line of first-order liquid-gas transition ends at the CP where the transition is of the second-order [2]. Properties of water phases and transitions between them are given by properties of electromagnetic interactions.

Similarly, the system of strongly interacting particles in equilibrium, known as strongly interacting matter [1], is governed by the strong interactions. The binding force that holds protons and neutrons together to form nuclei and quarks and gluons together to form hadrons is known as the strong interaction — one of the fundamental forces in nature. In the Standard Model (see Sec. 1.1) of particle physics, the strong interaction is described in the framework of a relativistic quantum field theory called Quantum Chromodynamics (QCD) (see Sec. 1.2), where point-like quarks and gluons are the elementary constituents. The structure of the strongly-interacting-matter phase diagram (see Fig. 1.2) is one of the most important topics in nuclear and particle physics.

Since the discovery of sub-hadronic particles, quarks and gluons, it became clear that hadrons are built from quarks and gluons and hence have substructure. It has been speculated that at high temperatures (T) and/or baryochemical potential (μ_B), densely packed hadrons will "dissolve" into a new phase of quasi-free quarks and gluons, the quark-gluon plasma (QGP) [3]. Experiments on high-energy nuclear collisions seem to confirm this hypothesis. Consequently, the primary focus in studying the phase diagram of strongly interacting matter is the structure of the phase transition region between the hadron gas (HG) [4] and QGP [3, 5]. The transition at low T and high μ_B is believed to be of the first order and happens along a line which ends with decreasing μ_B at QCD CP [6] (see Sec. 1.5) and then turns into a crossover region (see Sec. 1.4.1). The experimental measurements serve the purpose of gaining insights into the transition region and decisively answering the question of the existence and location of QCD CP in nature.

1.1 Standard Model

The Standard Model of particle physics is a theory classifying all known elementary particles and explains three fundamental interactions: strong, electromagnetic, and weak. All elementary particles can be divided into two groups:

(i) bosons – particles having integer spin,

(ii) fermions – particles having half-integer spin.

There are four gauge bosons with spin $S = 1$ and the Higgs boson with spin $S = 0$. The fermion sector has six quarks (up, down, charm, strange, top, and bottom) and six leptons (electron, electron neutrino, muon, muon neutrino, tau, and tau neutrino). They are paired to form three generations, which have similar properties. All of them have anti-particles. Interactions between particles are exchanged by force carriers – bosons. Each type of fundamental force has specific carriers: strong – gluons, electromagnetic – photons, weak – $W^{\pm}$ and Z^0 bosons.

The building blocks of almost all visible matter are up and down quarks, which combine to create protons, and neutrons - constituents of atomic nuclei. The recent discovery of the Higgs boson has provided crucial insight into how elementary particles gain mass, thereby completing and reinforcing the self-consistency of the Standard Model. Within this model, the theory of strong interactions is known as QCD, playing a critical role in our understanding of particle physics.

1.2 Quantum chromodynamics

The quantum chromodynamics explains the physics behind the strong interaction [7]. Its relevant fields are quark and gluon, with associated particles of quarks and gluons. These particles interact through an internal degree of freedom known as the color. The term "chromodynamics" describes the dynamics that arise from this degree of freedom in the strong interaction. The two main features of the QCD theory are:

(i) **asymptotic freedom:** Wilczek, Gross [8], and Politzer [9] discovered asymptotic freedom in the strong interactions, revealing that particle interaction weakens at shorter distances.

This discovery enabled precise predictions of high-energy experiment results within the framework of perturbative quantum field theory [7].

(ii) **color confinement:** QCD's color confinement [10] is a notable characteristic that complements its asymptotic freedom. It entails that particles with color charges, like quarks and gluons, cannot exist independently in vacuum. Consequently, they cannot be detected directly.

Providing information on the dynamics of quarks and gluons, QCD can describe different phases of matter governed by strong interactions.

1.3 Phase diagram of strongly interacting matter

The diagram shown in Fig. 1.2 [11] illustrates the phases of matter that can be observed in a system described by QCD and is commonly referred to as the phase diagram of strongly interacting matter. This representation is based on the state-of-the-art of QCD findings.

The phase diagram presented in Fig. 1.2 has similarities to that of water's phase diagram (see Fig. 1.1). In this diagram, temperature (T) is plotted on the ordinate and baryon chemical potential (μ_B) on the abscissa, replaces the pressure in the water phase diagram. It depicts regions covered by the different phases and their boundaries. Several phases are distinguished in this diagram, including hadron gas [4], nuclear-matter [12], QGP [5], quark-matter [13, 14], and color-flavor-locked (CFL) [15] phase. To achieve the objectives of this thesis, two phases are briefly discussed below.

1.3.1 Hadron gas phase

Ordinary matter comprises quarks and gluons confined in hadrons (protons, neutrons and others), constituting atomic nuclei and electrons, forming atoms and chemical elements together. An ensemble of strongly interacting particles at low temperatures and relatively low baryonic chemical potential (low energy density) can be considered as a matter in the form of hadron gas (HG) [4] (see Fig. 1.2). Lattice calculation of strongly interacting matter at finite

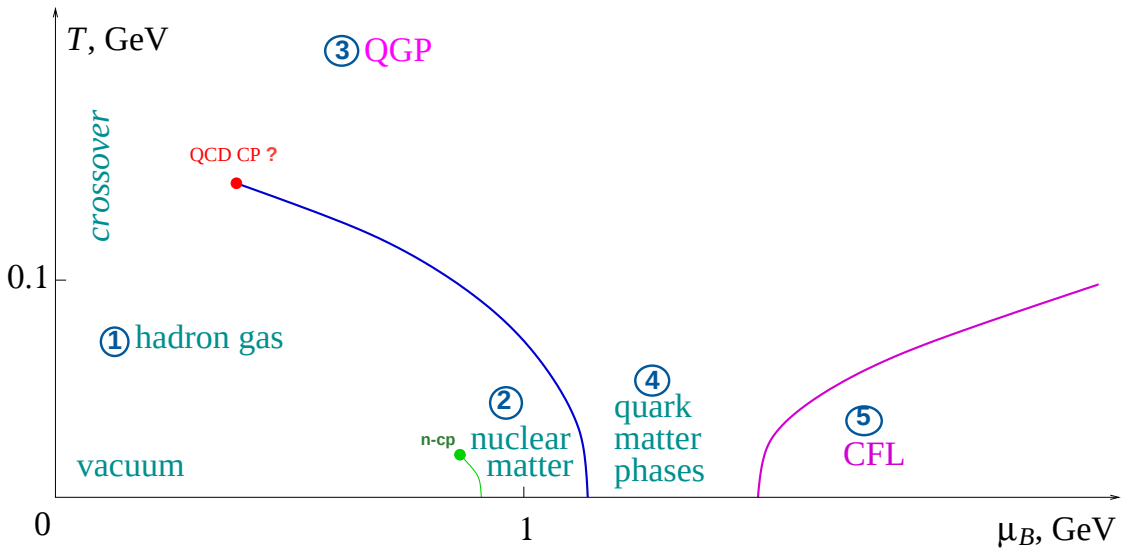

Figure 1.2 A semi-quantitative illustration of the contemporary view of the phase diagram of strongly interacting matter. Different phases of matter are marked on the phase diagram: 1) hadron gas [4], 2) nuclear matter [12], 3) QGP [3, 5], 4) quark matter [13, 14] and 5) CFL [15] phases. Also, the hypothetical QCD CP and crossover are mentioned. The green line at small temperatures and high densities shows the nuclear liquid-gas transition, also ending at a critical point (n-cp). The figure is taken from Ref. [11].

temperature, T and baryon chemical potential, μ_B suggest that the QCD thermodynamics in the HG can be effectively modeled by hadron resonance gas (HRG) [16, 17].

1.3.2 Quark-Gluon Plasma phase

As mentioned above, quarks and gluons are confined in hadrons at low energy densities. However, with increasing temperature and/or baryon density, a phase transition may occur to the state where the ordinary hadrons no longer exist, and quarks and gluons become the relevant degrees of freedom. The idea of asymptotic freedom (see Sec. 1.2) evolved into a concept of a new state of matter. In 1978, Shuryak coined the name of the new state of matter as *quark-gluon plasma* (QGP) [5].

Many years of intense experimental and theoretical studies of high-energy nucleus-nucleus collisions led to the conclusion that QGP exists in nature. To create the QGP state, nuclei must accelerate to velocities close to the speed of light and collide, creating a dense medium of quarks

and gluons. Signatures of the new state of matter in heavy ion collisions were first observed in the measurements of the CERN SPS (Super Proton Synchrotron) heavy-ion experiment [18]. This was followed by the detailed description of the properties of the QGP by experiments working on the Relativistic Heavy Ion Collider (RHIC) [19, 20] at BNL.

Nowadays, the primary focus in investigating strongly interacting matter is to understand the structure of the phase diagram, particularly the phase transitions [21, 22] between HG and QGP.

1.4 Phase transition between HG to QGP

The transition from the HG phase to the QGP phase is probably similar to the transition from liquid water to water vapour [11]. The first-order transition line ends at the second-order critical point, and the cross-over transition follows. In Fig. 1.2, the first-order phase transition is marked by a solid blue line separating the HG and QGP phases. There, the HG-QGP phase transition also separates regions with broken chiral symmetry [23] (HG state) and restored chiral symmetry [24] (QGP state). For many years, chiral transition [25] and deconfinement [26] were considered to occur at the same T and μ_B [27, 28]. The later studies [29, 30] suggest that these two transitions might be separated in the strongly interacting matter phase diagram.

1.4.1 Cross-over region

The temperature-driven change at zero μ_B is not a thermodynamic singularity but a smooth crossover [31] between HG and QGP. Most of the theoretical knowledge of the phase diagram is restricted to the vicinity of $\mu_{\mathrm{B}} = 0$, where lattice QCD [32] methods can be employed. In this limit, the lattice calculations have shown that the change from the low-temperature phase, where the degrees of freedom are hadrons, to the high-temperature phase described by quarks and gluons is an analytic crossover [33].

1.4.2 QCD CP

Due to the sign problem [34], studying QCD on the lattice at a finite chemical potential is exponentially difficult. Nevertheless, several different model approaches [35, 36, 37, 38, 39, 40]

indicate that the transition in this region is the first-order. Since the first order line originating at zero T cannot end at the vertical axis μ_B = 0, the line must end somewhere in the middle of the diagram [11]. This suggests that there is a hypothetical end-point that has properties of a second-order phase transition, referred to as QCD CP in this thesis.

At QCD CP, the system exhibits critical phenomena, such as diverging correlation length, which is associated with forming long-range correlations [41] and emerging universal behavior. The first lattice prediction for the location of QCD CP ($T = 160 \pm 3.5$ MeV and μ_B = 725 $\pm$35 MeV) has been reported in 2002 in Ref. [42]. Existing lattice methods can also be viewed as extrapolations from μ_B = 0, but finite T. There are two promising approaches to determine the location of QCD CP; one is simulations at finite imaginary values of μ_B [43], and another approach is Taylor expansions around μ_B = 0 [44].

There are many model to predictions on the location of QCD CP in the phase diagram. Some of them are summarized in Fig. 1.3 and Table 1.1.

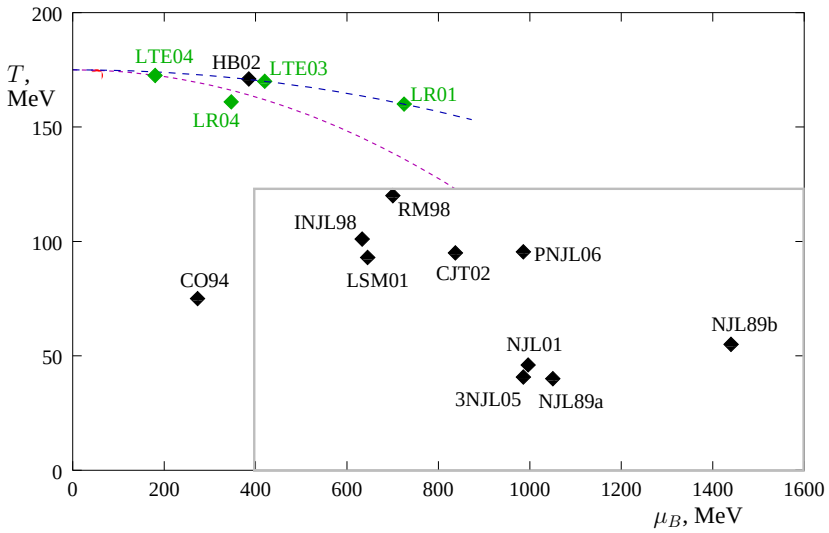

Figure 1.3 Comparison of predictions for the location of QCD CP on the phase diagram (see Ref. [11]). Black points are model predictions, and green points are lattice predictions. The two dashed lines indicate the magnitude of the slope $\frac{\mathrm{d}^2 T}{\mathrm{d}\mu^2}$ obtained by lattice Taylor expansion [44]. The gray region indicates the possible location of QCD CP, as predicted by the latest lattice QCD calculations [45].

The latest lattice QCD calculation [45] suggests that a possible QCD CP in the phase diagram

Table 1.1 Model predictions of the location of QCD CP, see details in Ref. [11].

Source	(T, μ_B) MeV	Comments	Label
MIT Bag/QGP	none	only 1st order, no chiral symmetry	—
Asakawa, Yazaki '89	(40, 1050)	NJL, Case I	NJL89a
Asakawa, Yazaki '89	(55, 1440)	NJL, Case II	NJL89b
Scavenius , et al '01	(93,645)	linear σ-model	LSM01
Scavenius , et al '01	(46,996)	NJL	3NJL05
Fodor, Katz '01	(160, 725)	lattice reweighting	LR01
Hatta, Ikeda '02	(95,837)	effective potential (CJT)	CJT02
Antoniou, Kapoyannis '02	(171,385)	hadronic bootstrap	HB02
Ejiri, et al '03	(170,420)	lattice Taylor expansion	LTE03
Ejiri, et al '03	(172,189)	lattice Taylor expansion	LTE04

may exist for,

$$T(\mu_B) < 130 \text{ MeV and } \mu_B > 400 \text{ MeV} .$$

Also, calculations of the equation of state as a function of T and μ_B have been performed using direct simulations at imaginary chemical potential [46], and calculations using up-to-eighth order Taylor expansions in μ_B [44]. Results of such calculations agree well for $\mu_B/T \leq 2$ - 2.5 [47].

There are no conclusive predictions of QCD CP from the lattice QCD calculations and different models. It is necessary to do an experimental search in order to determine whether or not QCD CP exists and, if it exists, where it is located in the QCD phase diagram.

1.5 Strongly interacting matter in heavy-ion collision

The phase diagram of strongly interacting matter can be accessed experimentally in nucleus-nucleus collisions at ultra-relativistic energy. Experimentally, the structure of the phase diagram is explored by studying the final states produced in relativistic nucleus-nucleus collisions. By varying collision energy and size of colliding nuclei, one can change T and μ_B of the matter [48].

Experimental programs at the Brookhaven Alternating Gradient Synchrotron (AGS) [49],

Relativistic Heavy-Ion Collider (RHIC) [22, 50] at Brookhaven, and the CERN Super Proton Synchrotron (SPS) [18] have concentrated on studying the phase diagram of strongly interacting matter. Several new facilities will join the study in the future. These are the Nuclotron-based Ion Collider facility(NICA) [51] at the Joint Institute for Nuclear Research (JINR) in Dubna, Russia, the Compressed Baryonic Matter (CBM) Experiment [52] at the Facility for Antiproton and Ion Research in Europe (FAIR) [53] at Darmstadt, Germany, and the J-PARC heavy ion project (J-PARC-HI) [54] at the Japan Proton Accelerator Research Complex (J-PARC) in Tokai, Japan.

Figure 1.4 shows a region of the $T - \mu_B$ phase diagram explored by NA49 [55] and NA61/SHINE [56] experiments. Experimentally determined chemical freeze-out [57] points for NA49 (blue squares) and those predicted for NA61/SHINE (green circles) based on the hadron gas model [58] are indicated.

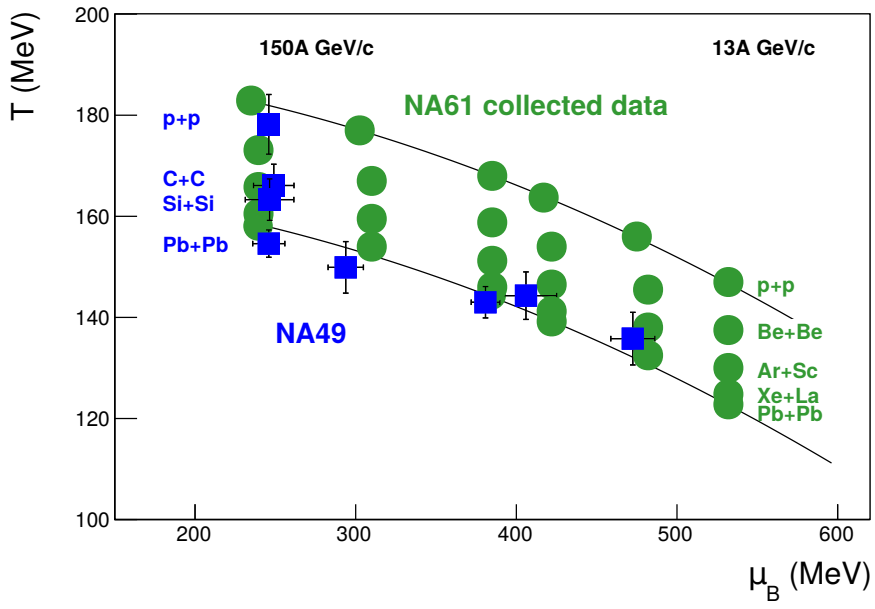

Figure 1.4 Experimentally determined chemical freeze-out points for NA49 [55] (blue squares) and those predicted for NA61/SHINE [56] (green circles) based on the thermal hadron gas model [58]. This is an updated version of the plot from Ref. [59].

1.6 Critical point search strategy

This section presents concepts and methods relevant to the experimental investigation of strongly interacting matter's critical behavior at the CERN SPS. The characteristic signatures of QCD CP can be observed if the freeze-out point [57, 60] is located close to QCD CP. The analysis of the existing experimental data indicates that the location of the freeze-out point in the phase diagram depends on the collision energy and the mass of the colliding nuclei (see Fig. 1.4). Thus, the experimental search for QCD CP requires a two-dimensional scan of collision energy and the system size. Nuclear collisions provide a possible method for finding QCD CP, but only at energies higher than the energy of the QGP creation [61], which was determined empirically to be at the low SPS energies [62].

1.7 QCD CP search observables

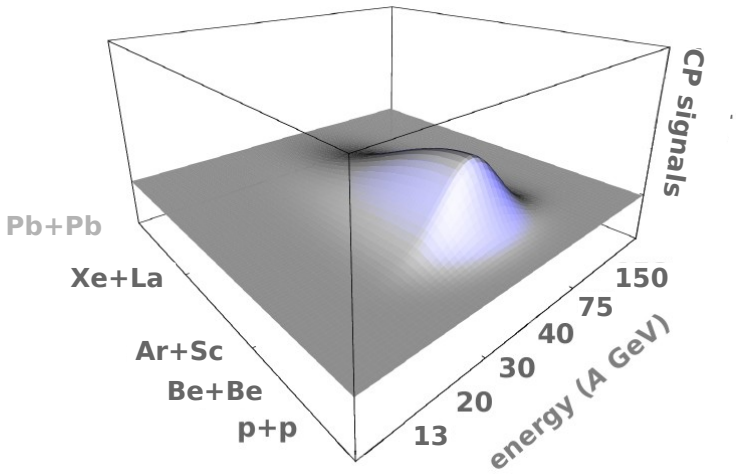

Figure 1.5 A sketch of the "critical hill" that is shown in the search for QCD CP in the two-dimensional plane (system size)-(collision energy). The maximum of the characteristic fluctuation signals of QCD CP is located at the hill. The figure is taken from Ref. [63].

Fluctuations are considered promising signatures of QCD CP. A second-order phase transition is characterized by the divergence of the correlation length. The system has been made to be

scale-invariant. This leads to characteristic fluctuations, for example, particle multiplicity [6]. Thus, a region with significant fluctuations as illustrated in Fig. 1.5 [63], may signal QCD CP. Experimental studies were strongly motivated by these expectations.

NA61/SHINE searches for QCD CP using such quantities as central moments of multiplicity distributions of higher-order [64], intensive and strongly intensive measures of particle multiplicity and kinematic variable fluctuations [65], short-range correlations [66] and intermittency analysis [67]. The latter is the subject of this thesis.

1.7.1 Multiplicity fluctuations in a large momentum acceptance

The expected signal of QCD CP is a non-monotonic dependence of various fluctuation and correlation measures in the NA61/SHINE energy-system size scan. Special interest is given to the fluctuations of conserved charges such as electric, strangeness, or baryon number.

In particular, NA61/SHINE has studied the net-electric charge fluctuations for $p+p$, central Be+Be, and Ar+Sc interactions [68] (see Appendix B.1). No evidence for QCD CP has been found.

Moreover, transverse momentum fluctuations have been measured by the NA49 and NA61/SHINE experiments [69, 70]. No evidence for QCD CP has been found.

1.7.2 Short-range correlations

Short-range correlations have been studied by NA61/SHINE. The dependence of Levy exponent, α (see Appendix B.1.3) for Be+Be and Ar+Sc at 17 GeV by NA61/SHINE is approximately independent of transverse mass (m_T), and far from the conjectured value for QCD CP, α = 0.5 [71]. No evidence for QCD CP has been found.

1.7.3 Intermittency analysis

Intermittency refers to the random deviations from regular behavior, characterized by scale invariance, fractality, and stochastic nature of the underlying physics [72]. The intermittent multiplicity fluctuations in high energy collisions [73] were discussed as the signal of the critical point in particular by Satz [74], Antoniou et al. [75] and Bialas, Hwa [76] (see Chapter 2).

The pioneering work of Wosiek [77] showed that intermittent behavior is expected at the phase transition of the second order. Further studies [74, 75, 73] also suggested intermittency at QCD CP. This inspired studies utilizing scaled factorial moments [78] to analyze particle multiplicity fluctuations in search for QCD CP (see Sec.2.1). The results of NA49 on critical fluctuations of the proton density in nucleus-nucleus collisions at 158A GeV/c [78] suggest that effects related to QCD CP have been observed in collisions of medium-size nuclei at the top SPS energy (see Sec. 2.4).

This motivated NA61/SHINE to perform a systematic scan in collision energy and system size through the analysis of the scaled factorial moments (SFMs) of the second and higher orders as a function of the phase space cell size in the transverse momentum plane to answer the question, does QCD CP exist in nature? Also, if QCD CP exists in nature, where is it located in the QCD phase diagram?

1.8 Thesis' outline

Search for QCD CP by proton intermittency analysis of Ar+Sc and Pb+Pb data of NA61/SHINE is the subject of this thesis. The second-scaled factorial moments for mid-rapidity protons using cumulative variables of transverse momenta and statistically independent data points have been measured.

This thesis consists of eight chapters, and it is organized as follows: Chapters 1 and 2 introduce the basic concepts and experimental searches for the critical point of strongly interacting matter. Innovative methods used by the author when analyzing the proton intermittency are presented in Chapter 3. They include using cumulative variables and statistically independent data points. Chapter 4 describes important for the thesis aspects of the NA61/SHINE facility. Analysis details are given in Chapter 5. It includes the event and track selection cuts, with special attention paid to the selection of proton candidates. The single and two-particle acceptance maps used for the selection of proton candidates are also presented. Results on second-order scaled factorial moments of proton multiplicity distribution in transverse-momentum space at mid-rapidity are presented in Chapter 6. Chapter 7 discusses the comparison of the experimental

results with models, concluding that there is no evidence for the critical point. An upper limit on the fraction of critical-proton pairs and the power of the correlation function is also obtained based on a comparison with the Power-law Model. A brief summary and conclusions are given in Chapter 8. Supplementary information is given in Appendixes A- E.

1.9 Novelty and author's contributions

The first proton intermittency results of 0–10% central ^{208}Pb + ^{208}Pb collisions at 13*A* and 30*A* GeV/*c*, and ^{40}Ar + ^{45}Sc collisions at 13*A*, 19*A*, 30*A*, 40*A*, and 75*A* GeV/*c* are reported in this thesis. To get these results, the analysis procedure started with defining and applying quality cuts on events and tracks in experimental and EPOS1.99 model data. Also, the centrality selection for ^{208}Pb + ^{208}Pb collisions at 13*A* and 30*A* GeV/*c* was performed using data-based and model-based methods, which are discussed in detail in this thesis.

One of the novelties of these analyses is the use of cumulative variables and statistically independent data points in the intermittency analyses. Also, the momentum-based two-track distance (mTTD) cut introduced in this thesis is a new tool for the intermittency analysis to account for the detector losses of close-in-space tracks properly. The new approach to proton intermittency analysis is discussed in detail in Chapter 3. The NA61/SHINE Collaboration will use a similar prescription for intermittency analysis of other data sets.

The results show no indication of QCD CP. To quantify these results, the exclusion plots for the fraction of critical-proton pairs, and the power of the correlation function are obtained based on a comparison with the Power-law Model [79].

The NA61/SHINE Collaboration at CERN SPS has released the proton intermittency results in 0–10% central ^{40}Ar + ^{45}Sc collisions at 13*A*–75*A* GeV/*c* as final results [80]. The publication draft with the proton intermittency results from the Ar+Sc energy scan is under review by the NA61/SHINE Editorial Board. The NA61/SHINE Collaboration released the preliminary results for 0–10% central ^{208}Pb + ^{208}Pb collisions at 13*A* and 30*A* GeV/*c* [81], which will be finalized for another publication.

The results were presented by me in talks and posters at eight international conferences and

schools. Besides obtaining the important and unique physics results presented in this thesis, I was responsible for tests of the new TPC reconstruction software of NA61/SHINE using experimental and Monte Carlo data. Moreover, I actively participated in the NA61/SHINE data-taking and the MTPC installation campaign at the CERN SPS.

Chapter Two

Intermittency analysis

in high energy physics

Intermittency refers to random deviations from smooth or regular behavior [72]. The idea of "intermittency" which was first introduced to the study of turbulent flow [82], later became important in the physics of particle production, especially as a way to study fluctuations. In the pioneering article of Bialas and Peschanski [73] introducing intermittency analysis to high-energy physics, it was proposed to study the scaled-factorial moments of the multiplicity of particles produced in high-energy collisions as a function of the resolution-size of rapidity interval. Wosiek found an evidence of intermittent behavior in the critical region of the two-dimensional Ising model [83]. This raised the general question of whether or not intermittency and critical behavior are related. Satz showed that the critical behavior of the Ising model indeed leads to intermittency, with indices determined by the critical exponents [74]. Later, Bialas and Hwa reported [76] that intermittency parameters could serve as a signal of second-order phase transition in a statistical system. This initiated experimental studies of the structure of the phase transition region via studies of particle multiplicity fluctuations in high-energy collisions using scaled-factorial moments.

2.1 Scaled factorial moments

The use of scaled-factorial moments (SFMs) [73] allows one to decrease the statistical bias due to the finite multiplicity of produced particles in a single collision. At the same time, this

measure is sensitive to interesting dynamical phenomena, such as the emergence of new scales in particle production or the existence of an "intermittent" background - cascading fluctuations at different scales. Moreover, this method allows one to identify unusually large fluctuations, such as fluctuations at the second-order phase transition. The SFMs, $F_r(M)$ of order (rank) r is

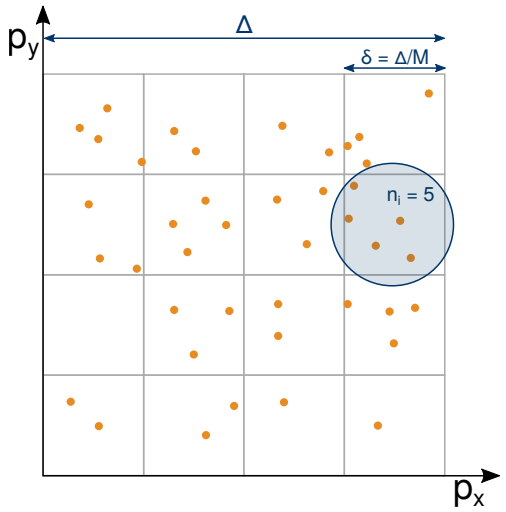

Figure 2.1 Two-dimensional transverse-momentum space is sub-divided into $M \times M$ number of equally sized bins. The n_i is the particle multiplicity in a given sub-interval, Δ is the momentum region, and δ is bin-width. The figure is taken from Ref. [84]

.

defined as [73]:

$$F_r(M) = \frac{\left\langle \frac{1}{M^D} \sum_{i=1}^{M^D} n_i ... (n_i - r + 1) \right\rangle}{\left\langle \frac{1}{M^D} \sum_{i=1}^{M^D} n_i \right\rangle^r}, \tag{2.1}$$

where M^D is the number of equally-sized subdivision intervals in which the D-dimensional space is partitioned, n_i is the particle multiplicity in a given sub-interval, angle brackets denote averaging over the analyzed events, and Δ is the momentum interval as shown in Fig. 2.1. The $F_r(M)$ equals one for all values of r and M^D providing:

(i) multiplicity distribution in Δ is Poissonian,

(ii) particle production is uncorrelated,

(iii) particle density in sub-division space is uniform.

For the ideal gas of particles in the grand-canonical ensemble, these conditions are satisfied in the configuration space, where the particle density is uniform throughout the gas volume, multiplicity fluctuations are Poissonian, and particles are uncorrelated. The momentum distribution is generally non-uniform, and thus, in the momentum space, it is more convenient to use the so-called cumulative variables [85]. By construction, particle density in the cumulative variables is uniformly distributed (see Sec. 3.1.2).

If the dynamics of the particle production are scale-invariant [86], that could be reflected in the power-law behaviour of the SFMs [73]:

$$F_r(M) = F_r(\Delta) \cdot (M^D)^{\phi_r} \ . \tag{2.2}$$

The logarithm of SFMs can be written as:

$$log_{10}F_r(M) = \phi_r \cdot log_{10}M^D \ + \ log_{10}F_r(\Delta) \ . \tag{2.3}$$

Figure 2.2 (*left*) shows the linear dependence of the logarithm of SFMs as a function of the logarithm of M^D (for D = 2).

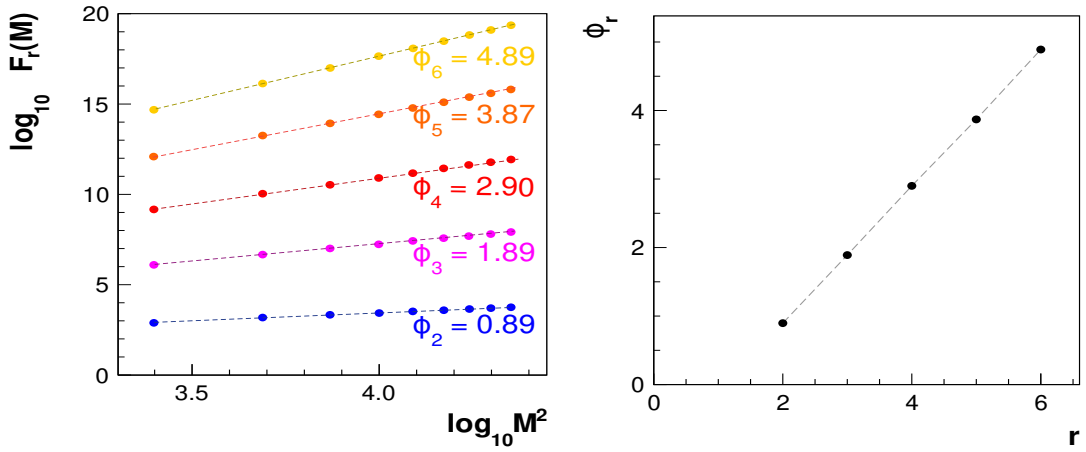

Figure 2.2 *Left:* The log-log plot of the scaled-factorial moments of order r = 2, 3, 4, 5, 6 (full-color circles) from the Power-Law model [84] and also intermittency indices (ϕ_2, ϕ_3, ϕ_4, ϕ_5, ϕ_6) values are shown. *Right:* Linear dependence of intermittency indices on the order of moments, *r* are shown.

The associated intermittency indices, ϕ_r are predicted [78, 87] to follow the pattern:

$$\phi_r = (r-1) \cdot (d_r/D), \tag{2.4}$$

with d_r, the so-called anomalous fractal dimension of the set formed by the order parameter density fluctuations. Figure 2.2 (*right*) shows linear dependence of ϕ_r on *r*.

For the mono-fractal set, d_r is independent of r, and it is related to the corresponding fractal dimension, d_F, through the relation, $d_r = D - d_F$. Such behaviour is analogous to critical opalescence in conventional matter [88]. This initiated experimental studies of the structure of the phase transition region via studies of particle multiplicity fluctuations using SFMs.

2.2 First intermittency analyses

The pioneering paper by Bialas and Hwa [76] served as the motivation for the CERN SPS experiments (EMC [89], NA22 [90], and KLM [91]) to begin the search for intermittency signal at the beginning of 1990. These studies use power law fits to determine intermittency indices, ϕ_r, based on the bin size dependence of the scaled-factorial moments of successive rank r in the pseudo-rapidity, η (see Appendix A.5). Figure 2.3 (*left*) shows the anomalous dimensions,

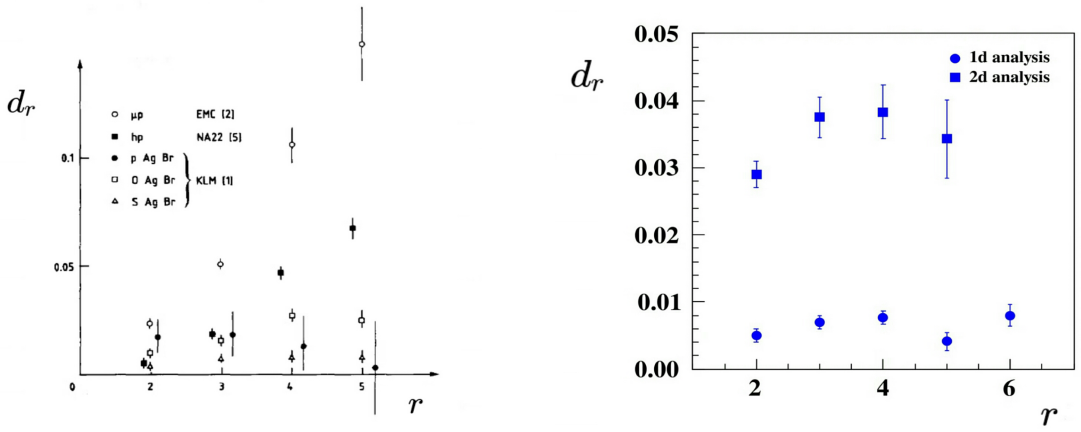

Figure 2.3 *Left:* Anomalous dimensions, $d_r = \frac{\phi_r}{r-1}$, of pseudo-rapidity spectra of hadrons produced in $\mu + p$ (EMC), $h + p$ (NA22), p+AgBr, O+AgBr, and S+AgBr (KLM) collisions at $\sqrt{s_{NN}} \approx 20$ GeV. *Right:* From an extended intermittency analysis of the emulsion data of the KLM collaboration: intermittency analysis in 1-dimensional (pseudo-rapidity) (shown by circles) and 2-dimensional (pseudo-rapidity and azimuthal angle) (shown by squares) as a function of subdivision size for the 19% most central S+(Ag Br) collisions at 200*A* GeV/*c* [92]. Plots are taken from Ref. [63].

$d_r = \frac{\phi_r}{(r-1)}$, of pseudo-rapidity spectra of hadrons produced in $\mu + p$ (EMC), $h + p$ (NA22), p+AgBr, O+AgBr, and S+AgBr (KLM) collisions at $\sqrt{s_{NN}} \approx$20 GeV. The anomalous dimension

stays constant for the heaviest system, for S+AgBr collisions at 200*A* GeV/c, but increases strongly for the small systems.

Later, an extended intermittency analysis was performed, where corrections were applied for the non-uniform rapidity distribution and the intermittency indices were determined both for one-dimensional (pseudo-rapidity) and two-dimensional (pseudo-rapidity and azimuthal angle) sub-divisions for S+AgBr collisions at 200*A* GeV/*c* emulsion data of the KLM Collaboration [92]. The values of d_r from both one-dimensional and two-dimensional are shown in Fig. 2.3 (*right*). The values of d_r are approximately 5 times larger in the two-dimensional analysis than in the one-dimensional analysis. Bialas and Seixas [93] explained this result as being due to the averaging of fluctuations via the projection procedure, and suggested that in the future, the factorial moment analysis in three dimensions should be mandatory for searching for critical behavior. Note that the proton intermittency analysis results reported in this thesis are done in the transverse-momentum plane for a small rapidity window. This is an analysis in three dimensions.

Motivated by previous findings, the WA80 [94] and NA35 [95] experiments at CERN SPS conducted intermittency analysis in nucleus-nucleus collisions at 200*A* GeV/c. WA80 found no significant intermittency effect in S+S and S+Au collisions [96]. However, NA35 observed an increase of factorial moments with the number of subdivisions of phase space, but the power law did not describe this rise accurately [97]. The puzzling results motivated further experimental studies of the structure of the phase transition region via analyses of particle multiplicity fluctuations using SFMs [78].

2.3 Intermittency in search for QCD CP

One of the main goals in heavy-ion collisions is to locate QCD CP in the phase diagram of strongly interacting matter (see Sec. 1.4.2). Intermittency analysis is a tool to find evidence for QCD CP in high-energy nuclear collisions. The signal of QCD CP is discussed as intermittent multiplicity fluctuations by Satz [74], Antoniou et al. [75] and Bialas, Hwa [76]. At QCD CP, the divergence of the correlation length (ξ) occurs due to the second-order phase transition [98]. The

particle density-density correlation function exhibits power-law scaling, inducing intermittent behaviour of particle multiplicity fluctuations [99]. Other system properties [6] are also sensitive to the vicinity of QCD CP, and these fluctuations have specific characteristics [76, 99]. If there are no long-range interactions, then all anomalous fractal dimensions are equal, i.e., the system is a simple fractal, as demonstrated explicitly for the Ising model [74]. These system properties can be measured by calculating SFMs at various system scales in transverse-momentum space [93, 100].

QCD-inspired considerations [11] suggest that the order parameter for the phase transition is the chiral condensate $\langle \bar{q}q \rangle$ [101], where q represents the quark field. The isoscalar σ-field [102] is the quantum state that contains both the quantum numbers and the critical properties of the chiral condensate. If this state can be formed in high-energy collisions, there are two possibilities for observing the properties of Eqs. 2.2 and 2.4:

(i) The sigma condensate will decay into pairs of π^+ and π^- with an invariant mass greater than that of two pions. Using universality class arguments, it was predicted that the exponent of expected power-laws in transverse-momentum space ($D = 2$) would have the value $d = \phi_2 = \frac{2}{3}$ [100].

(ii) Measuring proton number fluctuations [103] is a promising method for QCD CP search in heavy-ion experiments. The singularity of the baryon number susceptibility, which diverges [104] at QCD CP, is reflected in the fluctuations. Protons carry both baryon and electric charges, and $d = \phi_2 = \frac{5}{6}$ is expected here [88].

The ideal QCD CP signal derived for the infinite system in equilibrium, Eqs. 2.2 and 2.4, may be distorted by various effects in high-energy collisions, including the system's finite size [105, 106], evolution time, other particle correlations, and measurement acceptance and resolution [107]. In addition, QCD CP searches in high-energy collisions require the selection of the momentum-space region's dimension, interval size, and location. Unbiased results can only be obtained by analyzing variables and dimensions where the singular behavior appears [93, 108, 109], otherwise, the critical fluctuation signal can be distorted.

2.4 Intermittency results on search for QCD CP

The NA49 experiment at the CERN SPS began searching for evidence of the critical behavior of strongly interacting matter in 2000. Over the past decade, there has been interesting experimental exploration of intermittency and fractality in high-energy collisions.

NA49 searched for intermittency signals in the production of low-mass $\pi^+\pi^-$ pairs [110] and protons [78] at mid-rapidity in the most central collisions (12%, 12%, and 10%) of "C"+C, Si+Si, and Pb+Pb at a beam energy of 158*A* GeV/*c* ($\sqrt{s_{NN}} \approx 17.3$ GeV). They used the second scaled-factorial moment (SSFM), $F_2(M)$, and estimated the large background from misidentified and non-critical protons using the mixed event method (see Sec.3.1.1). The background subtracted moments, $\Delta F_2(M) \approx F_2^{data}(M) - F_2^{mixed}(M)$ were calculated as a function of M^2.

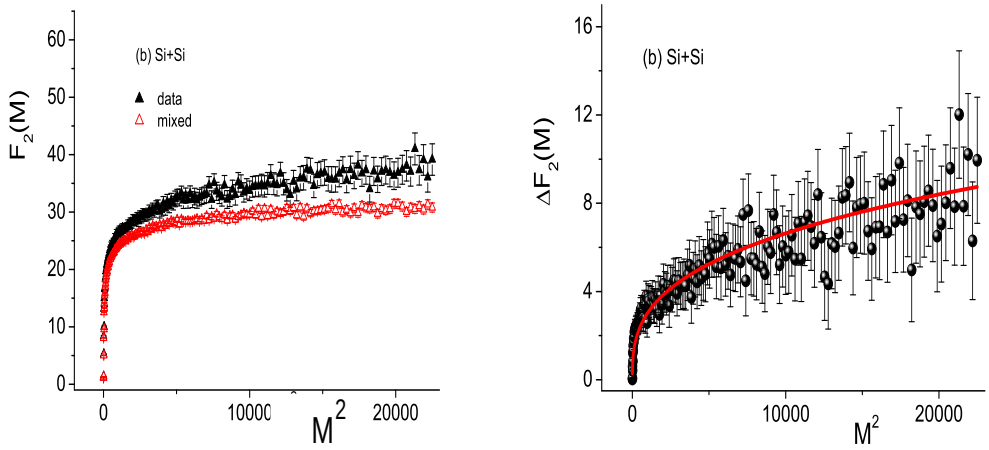

Figure 2.4 *Left:* SSFMs, $F_2(M)$ of the low-mass $\pi^+\pi^-$ pair multiplicity distribution is shown in transverse-momentum space at forward rapidity ($y \geq 0.5$) for the most central collisions of Si+Si (12%) at $\sqrt{s_{NN}}$ ≈17.3 GeV. The data (circles) is compared to the mixed events (crosses). *Right:* The background subtracted moments, $\Delta F_2(M) \approx F_2^{data}(M) - F_2^{mixed}(M)$, of the low-mass $\pi^+\pi^-$ pair multiplicity distribution are shown in transverse-momentum space at forward rapidity ($y \geq 0.5$) for the same collisions. A power-law fit for $M^2 > 2000$ with an exponent of 0.33 is also shown. The plots are taken from Ref. [110].

The SSFMs of the low-mass $\pi^+\pi^-$ pair multiplicity distribution versus the number of subdivisions of the transverse-momentum space are presented in Ref. [110]. The selected pairs covered the forward rapidity region ($y \geq 0.5$). For Si+Si collisions power-law increase was

observed with an exponent $\phi_2 = 0.33 \pm 0.04$ (see Fig. 2.4). The exponent extracted indicates a significant intermittency effect, but it is smaller than the expected critical point value of $\phi_2 = 0.67$. No systematic biases were studied.

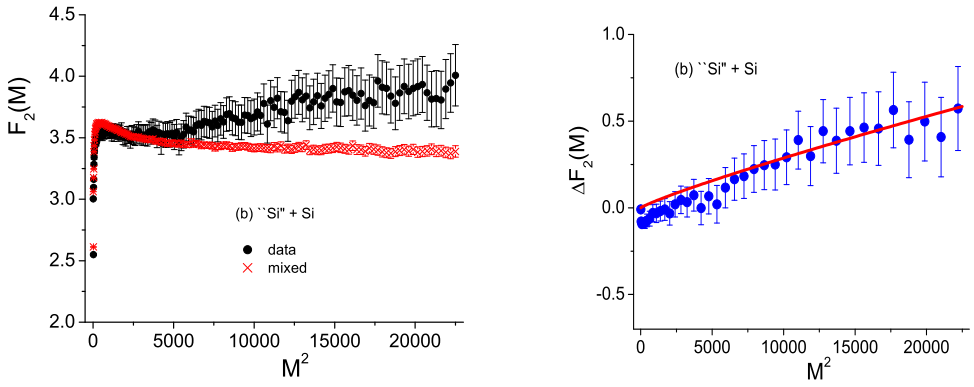

Figure 2.5 *Left:* $F_2(M)$ for protons in transverse-momentum space at forward rapidity ($-0.75 < y < 0.75$) for the most central collisions of Si+Si (12%) at $\sqrt{s_{NN}}$ ≈17.3 GeV. The circles (crosses) represent $F_2(M)$ of the data (mixed events), respectively. *Right:* background subtracted moments, $\Delta F_2(M) \approx F_2^{data}(M) - F_2^{mixed}(M)$, of proton number in transverse-momentum space at forward rapidity ($-0.75 < y < 0.75$) for the most central collisions of Si+Si (12%) at $\sqrt{s_{NN}}$ ≈17.3 GeV. The line in the plot shows the result of a power-law fit for $M^2 > 6000$ with an exponent of 0.96. Plots are taken from Ref. [78].

Figure 2.5 (*left*) shows that $F_2(M)$ values increase with M^2 for Si+Si collisions, while the mixed events remain constant. No intermittency signal was observed for proton production in C+C and Pb+Pb collisions, but power-law fluctuations were observed in Si+Si reactions with an exponent consistent with the critical point predictions. Figure 2.5 (*right*) shows the background subtracted, $\Delta F_2(M)$ values increasing with M^2. A power-law fit in the region $M^2 > 6000$ gave the result $\phi_2 = 0.96^{+0.38}_{-0.25}(stat) \pm 0.16(syst)$ with $\chi^2/d.o.f \approx 0.09 - 0.51$ [78].

The STAR Collaboration is searching for QCD CP at RHIC [50] through intermittency analysis of charged particles within $|\eta| < 0.5$ in Au+Au collisions at $\sqrt{s_{NN}}$ ≈ 7.7-200 GeV. Results are reported in Ref. [111]. Figure 2.6, (*a*)-(*d*) shows $F_r(M)$ data and mixed events corrected for reconstruction efficiency, from the second-order to the sixth-order in the range of M^2 from 1 to 100^2 in the most central (0-5%) Au+Au collisions at $\sqrt{s_{NN}}$ = 7.7-200 GeV. $\Delta F_r(M)$ (*r* = 2-6) is significantly larger than zero in the large M^2 region, where the increase

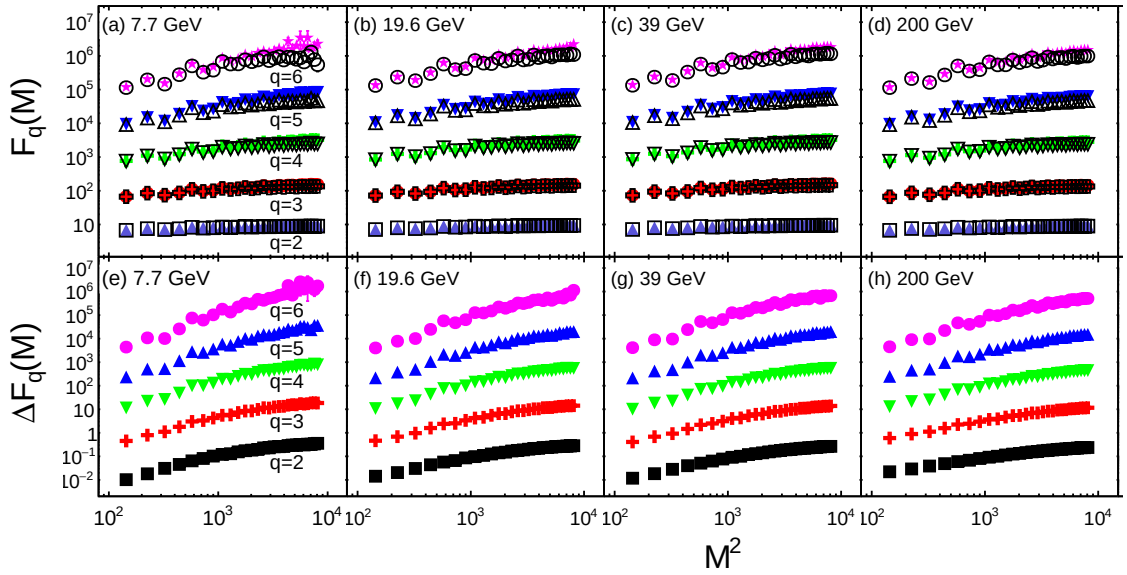

Figure 2.6 (a)-(d) The scaled-factorial moments, $F_r(M)$ (r = 2-6), of identified charged hadron ($h^{\pm}$) multiplicity in the most central (0-5%) Au+Au collisions at four example energies in the $\sqrt{s_{NN}}$ = 7.7-200 GeV range. Solid (open) markers represent $F_r(M)$ of data (mixed events) as a function of M^2. (e)-(h) $\Delta F_r(M)$ (r = 2-6) as a function of M^2 in the most central (0-5%) Au+Au collisions at four example energies in double-logarithmic scale. Plots are taken from Ref. [111].

slows down for $M^2 > 4000$. A distinct scaling behavior between the higher-order and second-order scaled-factorial moments, $\Delta F_r(M)/\Delta F_2(M)$ scaling, is reported in Au+Au collisions at all energies [111]. It is important to note that the event selection and acceptance criteria for the SPS results differ significantly from those of the RHIC-BES program.

A systematic search for QCD critical fluctuations has been conducted by the NA61/SHINE collaborations at CERN SPS. They measured intermittency in nucleus-nucleus collisions and conducted a two-dimensional scan of system size and collision energy for the first time. Reference [79] reports the recent results from the NA61/SHINE Collaboration on QCD CP search in ^{40}Ar + ^{45}Sc collisions at 150*A* GeV/*c* via proton intermittency analysis using cumulative variables and statistically independent data points. Following this study, the NA61/SHINE Collaboration is continuing the systematic search for QCD CP via proton intermittency analysis. The thesis will report the results of Ar+Sc and Pb+Pb collisions [80]. Intermittency analysis of negatively charged hadrons produced in Xe+La and Pb+Pb collisions is ongoing.

In the meantime, various model studies have been conducted to understand the experimental

data. It includes studies reported in Refs. [112, 113, 114, 115, 116, 117, 118] along with the Critical Monte-Carlo (CMC) [88] and Power-Law Model [84].

These new and upcoming results of intermittency analysis may answer the question about the nature of the transition region and, in particular, whether or not the critical point of strongly interacting matter exists.

Chapter Three

New approach to proton intermittency analysis

In the proton intermittency analysis presented here, only the second scaled-factorial moment (SSFM) is taken into account due to the limited statistics. The SSFM, $F_2(M)$, can be obtained by setting $r = 2$ and for two-dimensional space of transverse momentum, $D = 2$ in Eq. 2.1:

$$F_2(M) = \frac{\left\langle \frac{1}{M^2} \sum_{i=1}^{M^2} n_i(n_i - 1) \right\rangle}{\left\langle \frac{1}{M^2} \sum_{i=1}^{M^2} n_i \right\rangle^2}, \tag{3.1}$$

where the transverse-momentum space is partitioned into $M \times M$ equal-size bins and n_i is the number of protons in the i-th bin. For a fixed value of M, the numerator and the denominator are averaged over bins and then over events.

As discussed in Sec. 2.4, the NA49 experiment [55] at CERN SPS searched for an intermittency signal in the production of protons at mid-rapidity [78] in a the transverse-momentum plane using the SSFM. The proton spectra in transverse momentum are non-uniform. Moreover, for each M point, the full set of data was used. Thus, the results for different *M* are correlated. Statistical uncertainties were obtained using the Bootstrap method [119].

In this chapter, I'll discuss the new approach to proton intermittency analysis that the NA61/SHINE experiment uses to search for QCD CP. The novelty comprises of:

(i) cumulative transformation method (Sec. 3.1.2),

(ii) independent sub-sample of events for each data point (Sec. 3.2),

(iii) analytical calculation of statistical uncertainties (Sec. 3.3),

(iv) momentum-based Two-Track Distance (mTTD) cut (Sec. 3.4).

3.1 Intermittency analysis of non-uniform distributions

The intermittency signal of CP will always be affected by various biasing effects. The most important one is due to the fact that SFMs are sensitive to the shape of the single-particle momentum distribution. This dependence biases the signal of critical fluctuations. In the past, the mixed event method was utilized to correct the bias. Figure 3.1 (*top*) shows intermittency

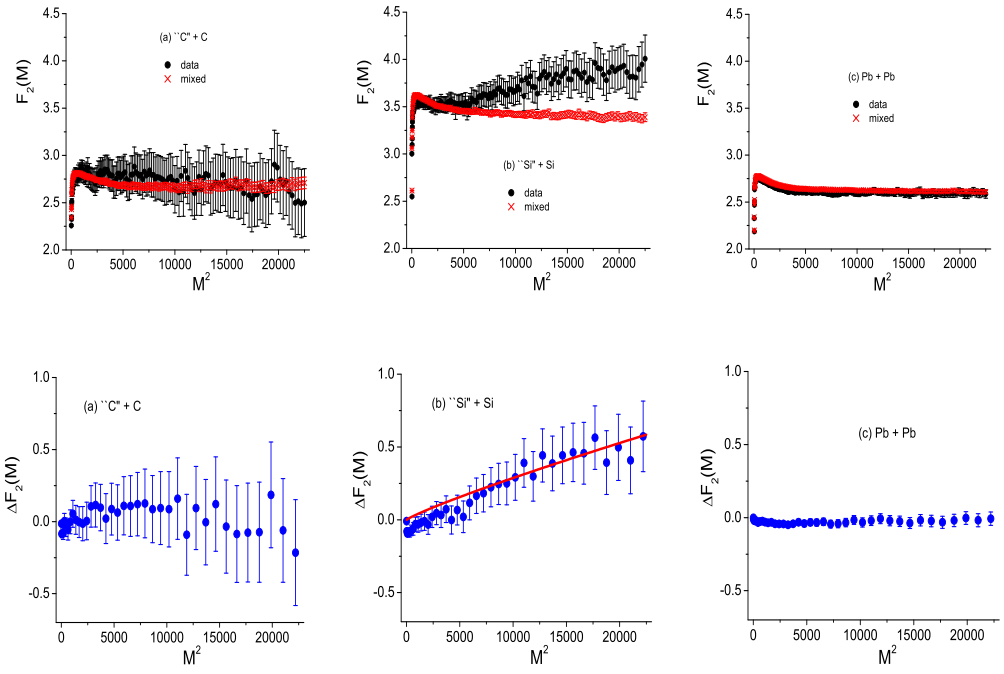

Figure 3.1 *Top:* $F_2(M)$ of protons in non-uniform transverse-momentum space at mid-rapidity for the most central collisions of (*a*) C+C (12%), (*b*) Si+Si (12%), and (*c*) Pb+Pb (10%) at $\sqrt{s_{NN}}$ ≈17.3 GeV [78]. The black circles (red crosses) represent $F_2(M)$ of the data (mixed events) respectively. *Bottom:* the background subtracted SSFMs, $\Delta F_2(M)$ for the most central collisions of (*a*) C+C (12%), (*b*) Si+Si (12%), and (*c*) Pb+Pb (10%) at $\sqrt{s_{NN}}$ ≈17.3 GeV are calculated using mixed event method. Statistical uncertainties were obtained using the Bootstrap method. Plots are taken from Ref. [78].

analysis results [78] of proton multiplicity at mid-rapidity in the most central (12%, 12%, and

10%) of C+C, Si+Si, and Pb+Pb collisions at 158A GeV/c ($\sqrt{s_{NN}} \approx 17.3$ GeV) from the NA49 experiment.

In these analyses, SSFMs were shown as a function of the number of sub-divisions in the transverse-momentum space. The black circles (red crosses) represent $F_2(M)$ of the data (mixed events). The background-subtracted SSFMs [78],

$$\Delta F_2(M) \approx F_2^{\text{data}}(M) - F_2^{\text{mixed}}(M), \tag{3.2}$$

were calculated to eliminate the bias due to non-uniform spectra using the mixed event method as shown in Fig 3.1 (*bottom*).

In the new approach, the cumulative transformation technique is used to eliminate bias rather than the mixed event method. In the subsequent subsections, two methods are briefly discussed.

3.1.1 Mixed event method

In the case of the mixed event method, particles from different data events are used to generate mixed events. Figure 3.2 graphically shows the procedure for the random mixing of particles from different events. Each particle in each mixed event comes from a different data event. Mixed

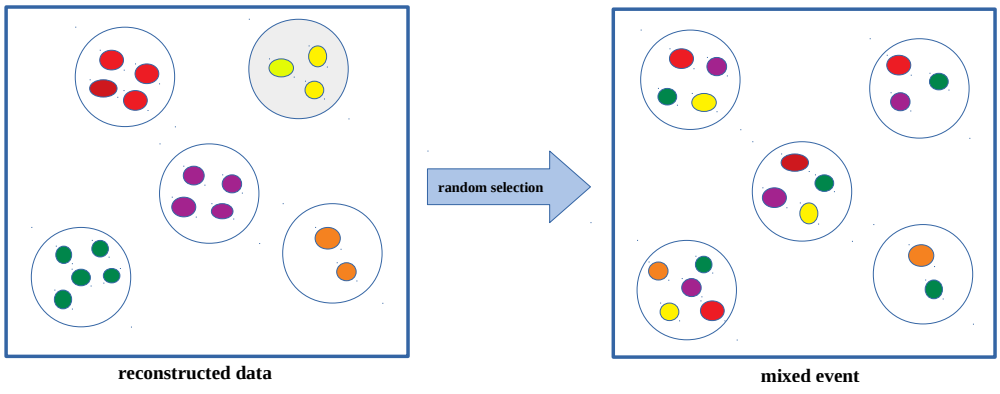

Figure 3.2 The procedure of random mixing of particles from different events is shown graphically to remove correlations between particles. Each open circle represents one event, and the color circle corresponds to the track of that event. The *left* box for reconstructed data and *right* box for mixed events.

events are constructed in this way to remove all correlations between particles. By construction, the multiplicity distribution of the data and mixed events are identical. Figure 3.4 (red circles)

shows the dependence of the SSFMs on the number of sub-division for mixed events constructed using the Power-law Model (see Sec. 7.2) setting the intermittency index to ϕ_2 = 0.83 for r =2.

It was shown that this procedure approximately removes the dependence of $\Delta F_2(M)$ on the shape of a single-particle distribution [78].

3.1.2 Cumulative transformation method

As it is discussed, the experimental results on $F_2(M)$ do depend on the shape of the single-particle distribution and on the choice of variables used for analysis. Bialas and Gazdzicki [85] proposed to study intermittency in terms of variables for which the single-particle density is constant. It was also shown [85] that this method reduces the bias caused by a non-uniform single-particle distribution leaving the CP signal unchanged. In this thesis, the suggested new variables are referred to as the *cumulative* variables.

Assume that the single particle distribution in a variable x is measured and given by a (non-negative) function $f(x)$. For a one dimensional distribution $f(x)$, the cumulative variable, Q_x, is defined as:

$$Q_x = \int_a^x f(x')dx' \Big/ \int_a^b f(x')dx' \ , \tag{3.3}$$

where a and b are lower and upper limits of the variable x. For a two-dimensional distribution $f(x, y)$ and a given x the cumulative transformation defined as:

$$Q_y(x) = \int_a^y f(x, y')dy' \Big/ \int_a^b f(x, y')dy'. \tag{3.4}$$

The cumulative variable has the following properties:

(i) its value depends on the ordering of particles in x, and thus it is the same for all variables which preserve the ordering,

(ii) the single-particle distribution in the cumulative variable is uniform, and it ranges from 0 to 1.

The property (i) gives a new way to compare the results obtained in different experiments. The property (ii) removes the dependence of the intermittency parameters on the shape of the

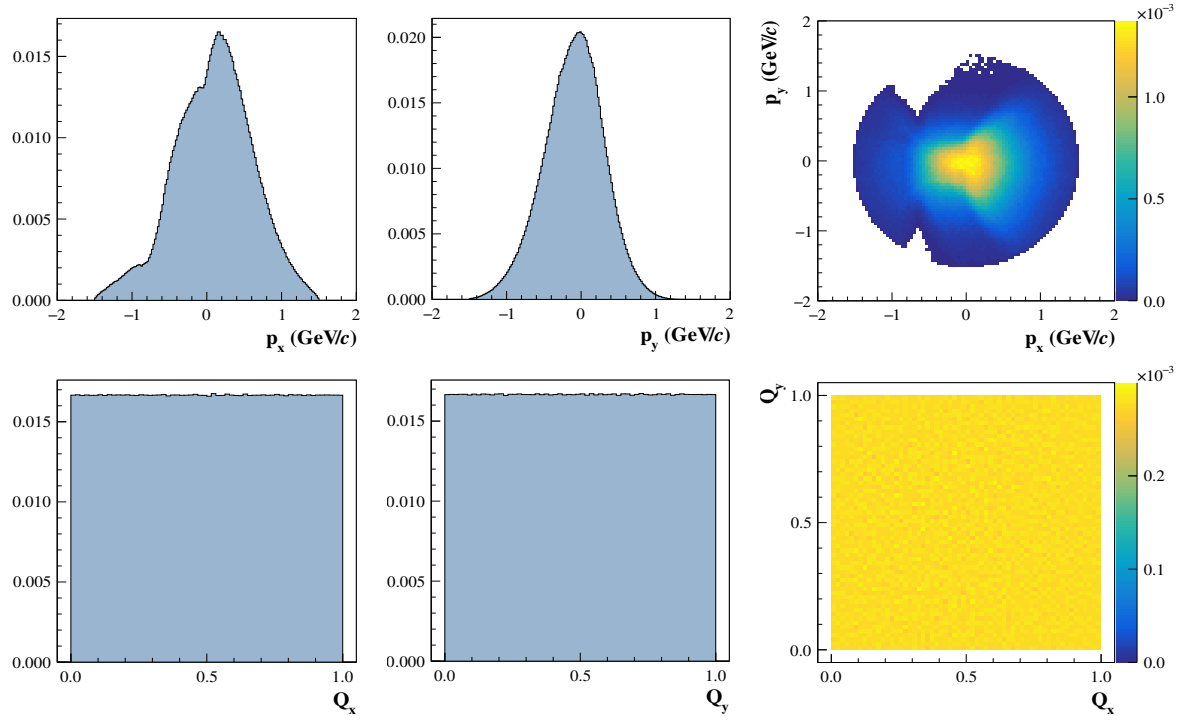

Figure 3.3 Example of the effect of the cumulative transformation of transverse-momentum components, p_x and p_y, generated from the Power-law Model [84]. Distributions before (*top*) and after (*bottom*) the transformation.

single-particle distribution. At the same time, it has been verified [120] that the transformation preserves the critical behaviour is given by Eq. 2.2, at least for the SSFMs.

An example of the cumulative transformation of transverse-momentum components, p_x and p_y generated from the Power-law Model, is shown in Fig 3.3 where distributions before (*top*) and after (*bottom*) the transformation are shown. Figure 3.4 shows the dependence of SSFMs on the number of sub-divisions in the cumulative-transformed transverse-momentum plane using data generated within the Power-law Model.

3.2 Statistically-independent data points

The intermittency analysis gives the dependence of scaled-factorial moments on the number of sub-divisions of transverse momentum or cumulative-transverse-momentum intervals. In the past intermittency analyses, the same data set was used to obtain results for each number of subdivisions (see Fig. 3.1). The results for different *M* are statistically correlated. Therefore

the full covariance matrix is required for proper statistical treatment of the results. This is numerically not trivial [121].

Here, statistically-independent subsets of data events are used to obtain results for each sub-division number. In this case, the results for different sub-division numbers are statistically independent. Thus only diagonal elements of the covariance matrix are non-zero, and the complete relevant information needed to interpret the results is easy to present graphically. However, this procedure decreases the number of events used to calculate each data point increasing statistical uncertainties. The number of events used in each subset was selected to obtain similar values of the statistical uncertainties of results for different subsets. Table 3.1 shows the fraction of all available events used to calculate each of the 10 points.

Table 3.1 Fraction of the total number of analyzed events used to calculate second-order scaled factorial moments for the chosen number of cumulative momentum bins.

number of bins (M^2)	1^2	50^2	70^2	86^2	100^2	111^2	122^2	132^2	141^2	150^2
fraction of all events (%)	0.5	3.0	5.0	7.0	9.0	11.0	13.0	15.5	17.0	19.0

Figure 3.4 illustrates an example of intermittency analysis using SSFM for a critical system utilizing the new approach with data generated by the Power-law Model and mixed events. Statistically-independent data subsets are used to obtain results for each sub-division number.

3.3 Statistical uncertainties

Statistical uncertainties in the intermittency analysis (see Fig. 3.1) of the NA49 experiments were calculated using the Bootstrap method [119]. Here, statistical uncertainties are calculated analytically. Below the new approach is briefly presented.

The standard expression for the SSFM, Eq. 3.1, can be rewritten as

$$F_2(M) = 2M^2 \frac{\langle N_2(M) \rangle}{\langle N \rangle^2}, \tag{3.5}$$

where N and $N_2(M)$ denote the total number of protons and proton pairs, respectively, in M^2 bins in an event.

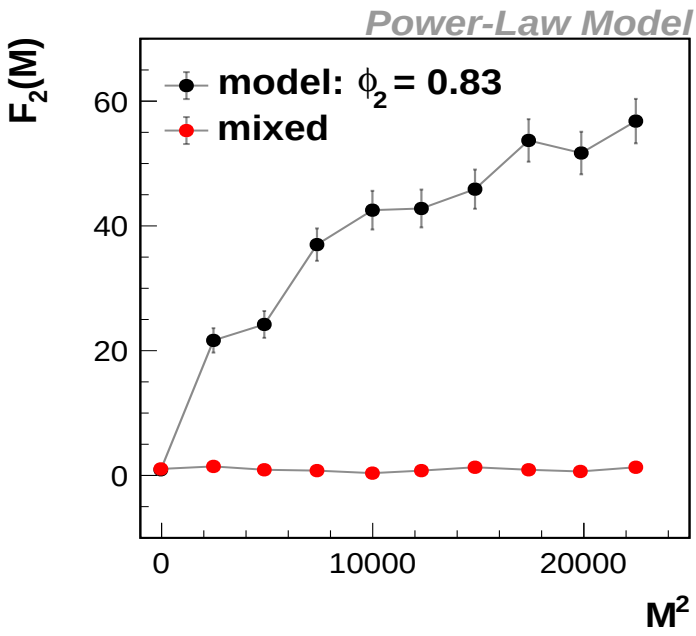

Figure 3.4 The dependence of the SSFMs of particle multiplicity distribution on the number of sub-divisions in cumulative transverse-momentum space. Independent sub-samples are used for each data point. Black and red circles indicate model and mixed events, respectively. Calculations were performed using the Power-law Model [84] with intermittency index, ϕ_2 = 0.83 for r = 2. Statistical uncertainties are calculated using statistical uncertainty propagation.

With the help of the modified SSFM expression, Eq 3.5, the statistical uncertainties can be calculated using the statistical uncertainty propagation:

$$\frac{\sigma_{F_2}}{|F_2|} = \sqrt{\frac{(\sigma_{N_2})^2}{\langle N_2\rangle^2} + 4\frac{(\sigma_N)^2}{\langle N\rangle^2} - 4\frac{(\sigma_{N_2N})^2}{\langle N\rangle\langle N_2\rangle}}\,. \tag{3.6}$$

Statistical uncertainties shown in Fig. 3.4 are calculated using this method. It has been found that the statistical uncertainties derived from each of the methodologies are similar [79]. However, the new approach, which utilizes statistical uncertainty propagation is easy to implement and fast.

3.4 Momentum-based Two Tracks Distance cut

Another new tool introduced to the intermittency analysis is a two-particle acceptance map in momentum space. The Time Projection Chambers (TPCs) (see Sec. 4.2.4) are the primary

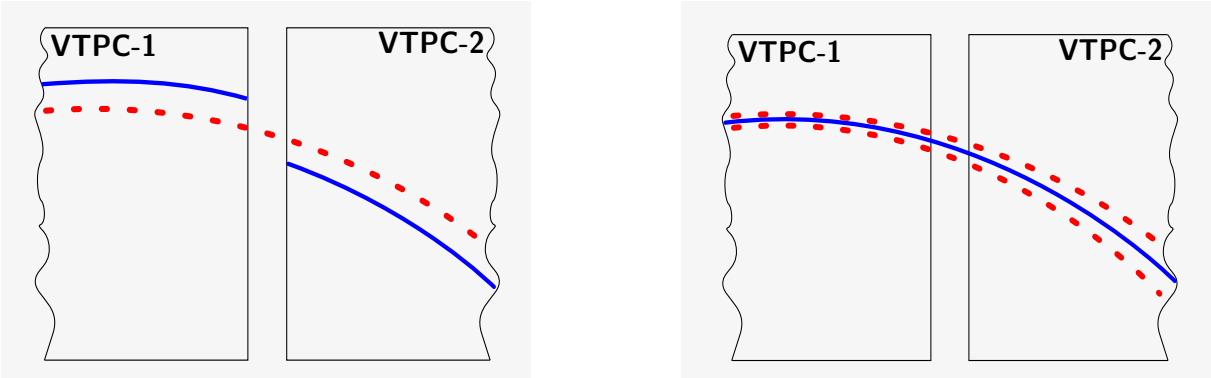

Figure 3.5 *Left:* An example of split tracks is illustrated here. The boxes represent the two TPC chambers labeled VTPC-1 and VTPC-2. The red dotted line is a single track, but it is split into two tracks between two VTPC-1 and VTPC-2 chambers. *Right:* An example of a merged track is illustrated here. The two red dotted lines represent the trajectory of two close in-space particles (tracks). The blue line represents the merged track, reconstructed when clusters of the two tracks overlap

tracking devices in the NA61/SHINE experiment. However, it's important to note that they do have limitations. In particular, when two tracks are too close in space, and their clusters overlap, the TPCs fail to differentiate between them. Consequently, the TPC cluster finder frequently rejects overlapping clusters, and the tracks can be lost. Moreover, the TPC track reconstruction may fail to merge two track fragments. This can generate two tracks out of a single track. These biases must be addressed.

An example of problematic tracks is shown in Fig. 3.5. One of them is a split track presented in Fig. 3.5 (*left*), and the second kind of problematic track is a merged track shown in Fig. 3.5 (*right*). The potential point ratio (see Sec. 5.2.3), the ratio of the number of measured clusters to the number of potential clusters in all TPCs, is required to be greater than 0.5 and less than 1.1. This cut can effectively eliminate split tracks. Previously, the geometric Two-Track Distance (gTTD) cut was utilized to eliminate a set of tracks that were positioned too closely together to be reconstructed using geometrical two-track distance calculations (see Fig. 3.6). Figure 3.6 (*left*) shows the geometric two-track distance of selected protons from Ar+Sc collisions at 75*A* GeV/*c* (red line) recorded by the NA61/SHINE experiment and the corresponding result for mixed events (black line). The ratio of the distributions is shown in Fig. 3.6 (*right*). The bias due to the low efficiency of measuring close tracks is seen for two-track distances

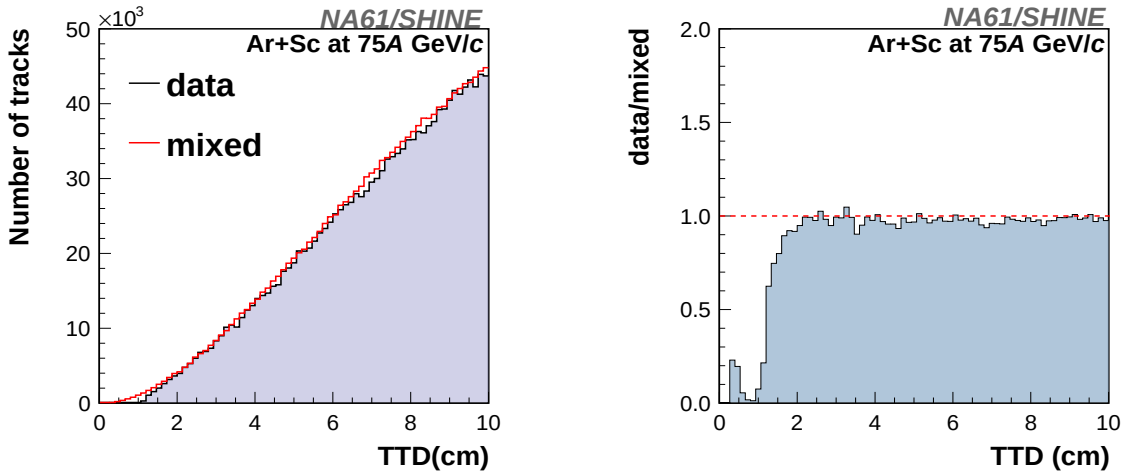

Figure 3.6 *Left:* An example of geometrical TTD for *central* ^{40}Ar + ^{45}Sc collisions at 75*A* GeV/*c* data (black line) and the corresponding mixed (red line) is shown. *Right:* The same distribution is shown for data to mixed ratio. A region less than $2\ cm$ corresponds to the biased region due to the low efficiency of measuring two tracks.

lower than 2 cm.

To apply the gTTD cut, the NA61/SHINE detector geometry and magnetic field information are required. However, access to this information is limited to those who are members of the NA61/SHINE Collaboration. Here, a momentum-based Two-Track Distance (mTTD) cut is introduced. The mTTD cut removes the remaining split tracks from the data after the potential point ratio cut, and it provides the precise definition of the biased region in which we don't have good efficiency for measuring two-tracks. Having this definition of the biased region, one can apply the mTTD cut to the model data. The magnetic field bends the trajectory of charged particles in the x-z plane. Thus, it is most convenient to express the momentum of each particle in the following momentum coordinates (see Fig. 3.7):

$$\begin{aligned} s_x &= p_x/p_{xz} = \cos(\Psi)\ , \\ s_y &= p_y/p_{xz} = \sin(\lambda)\ , \\ \rho &= 1/p_{xz}\ , \end{aligned} \tag{3.7}$$

where $p_{xz} = \sqrt{p_x^2 + p_z^2}$. For each pair of particles, a difference in these coordinates is calculated

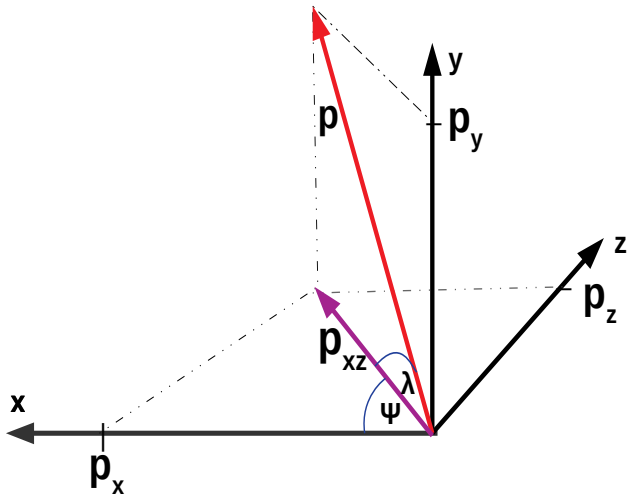

Figure 3.7 New momentum coordinate systems are introduced in s_x, s_y and ρ in terms of p_x, p_y, and p_{xz}. Where Ψ is the angle between p_{xz} and p_x, and λ is the angle between p_{xz} and p.

as:

$$\begin{aligned} \Delta s_x &= s_{x,2} - s_{x,1} \ , \\ \Delta s_y &= s_{y,2} - s_{y,1} \ , \\ \Delta \rho &= \rho_2 - \rho_1 \ . \end{aligned} \tag{3.8}$$

The distributions of particle pairs' momentum difference for pairs with gTTD less than 2 cm (as an example for Ar+Sc collisions at 75*A* GeV/*c*, see Fig. 5.20) are parameterized with ellipses in the new momentum coordinates. Such parameterized elliptical cuts are defined as:

$$\begin{aligned} \left(\frac{\Delta\rho}{r_\rho}\right)^2 + \left(\frac{\Delta s_y}{r_{s_y}}\right)^2 &\leq 1 \ , \\ \left(\frac{\Delta s_x}{r_{s_x}}\right)^2 + \left(\frac{\Delta s_y}{r_{s_y}}\right)^2 &\leq 1 \ , \\ \left(\frac{\Delta\rho\cos\theta - \Delta s_x \sin\theta}{r_{\rho s_x}}\right)^2 + \left(\frac{\Delta\rho\sin\theta + \Delta s_x \cos\theta}{r_{s_x\rho}}\right)^2 &\leq 1 \ , \end{aligned} \tag{3.9}$$

where $r_{\rho s_x}$ and $r_{s_x\rho}$ is the semi-major and semi-minor axis of an ellipse formed by $\Delta\rho$ and Δs_x, and θ is the angle from the positive horizontal axis to the ellipse's major axis. Similarly, other semi-major and semi-minor axes of the other ellipses are also defined in Eqs. 3.9.

Proton pairs with momenta inside all the ellipses are rejected. The mTTD cut can replace the gTTD cut. Due to its momentum-based definition, the mTTD cut can be used for model

comparison of the experimental results. The parameters of the mTTD cut (see Eqs. 3.9) are given in Table 5.6 and the cut is used for the data analysis (see Chapter 6) and comparison with the models (see Chapter 7).

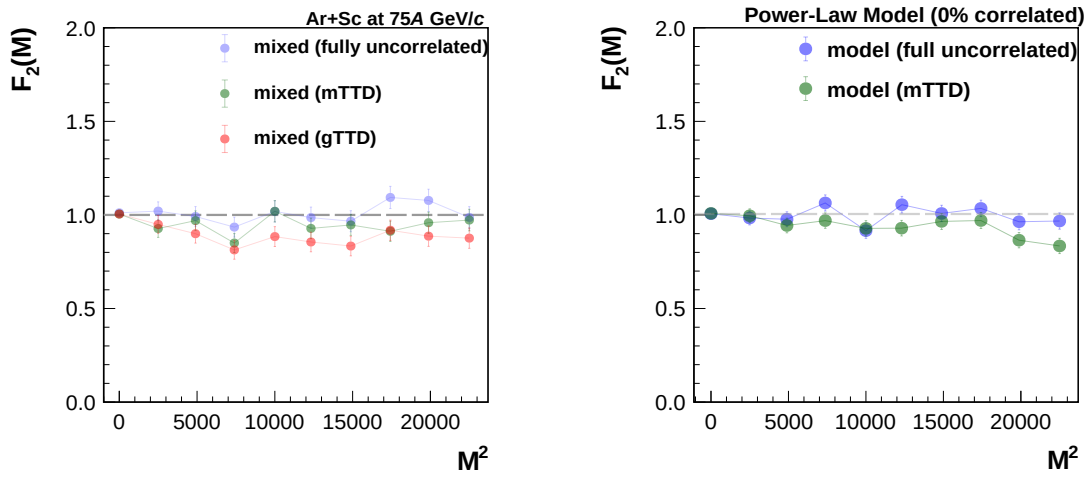

Figure 3.8 Example of the gTTD or mTTD cut impact on mixed events for ^{40}Ar + ^{45}Sc collisions at 75*A* GeV/*c* (*left*) and on the Power-law Model with uncorrelated particles only (*right*) are shown. The blue circles correspond to the dependence of $F_2(M)$ on M^2 where neither gTTD nor mTTD cut is applied to the mixed events or the Power-law Model. As indicated in the plot, the green and red points correspond to either gTTD or mTTD cut applied.

The effect of the mTTD cut for ^{40}Ar + ^{45}Sc collisions at 75*A* GeV/*c* mixed events and the Power-law Model is shown in Fig. 3.8. The dependence of $F_2(M)$ on M^2 in cumulative transverse-momentum space for $M^2 > 1$ is systematically below $F_2(M = 1)$ (See Chapter 6) when gTTD or mTTD cut is applied to fully uncorrelated mixed events (*left*) and the Power-law Model with uncorrelated particles only (*right*).

Chapter Four

NA61/SHINE experiment

The NA61/SPS Heavy Ion and Neutrino Experiment [56, 122], also known as the SHINE experiment, is situated in the North Area of CERN and is a fixed-target experiment on the H2 beamline of the Super Proton Synchrotron (SPS) accelerator. NA61/SHINE is a versatile experimental facility constructed to study hadron production in hadron-proton, hadron-nucleus, and nucleus-nucleus collisions. The long-term advancement of the proton and ion sources at CERN, the accelerator chain, and the H2 beamline in the CERN North Area has tremendously benefited the NA61/SHINE experiment. NA61/SHINE projected from the equipment inherited from its predecessors, specifically the NA49 experiment [55].

4.1 NA61/SHINE physics program

An advantage of using fixed target experiments in heavy ion collisions is that they typically have large rapidity acceptance and cover the low transverse momentum region. These features allow us to conduct various measurements for physics of strong interactions and for neutrino [123] and cosmic-ray [124] physics. The NA61/SHINE's strong interactions program is focused on a two-dimensional scan varying the size and energy of the collision system [125]. The scan in the collision energy is performed in the beam momentum range of 13A-150A GeV/c. The experiment studies interactions between the smallest nuclei, p+p and the heaviest ones Pb+Pb. Collected experimental data in the 2007-2018 period (see Fig. 4.1) allows NA61/SHINE for precise studies of the transition between the phases of strongly interacting matter and search for QCD CP.

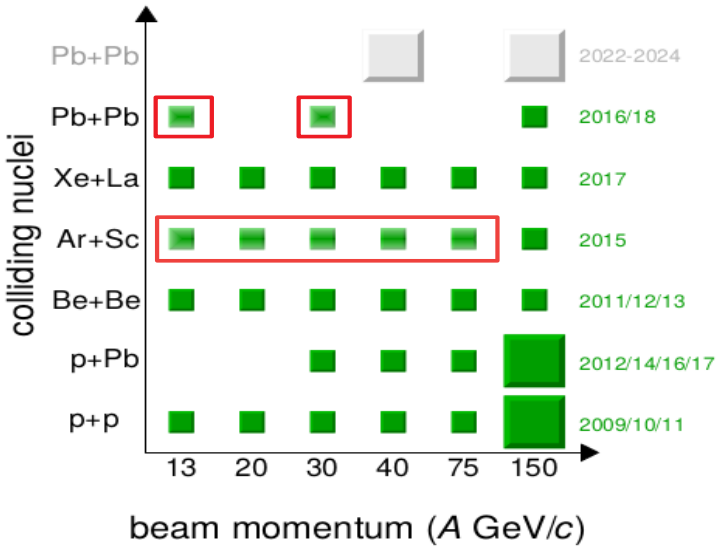

Figure 4.1 An overview of NA61/SHINE's system size and collision energy scan. The boxes show the already taken data, and the large boxes mark systems for which large statistics were obtained. The Ar+Sc and Pb+Pb data sets, demonstrated by red boxes, are being studied, and proton intermittency results are presented in this thesis.

An overview of the two-dimensional scan performed by NA61/SHINE is presented in Fig. 4.1. The area of the scan can be roughly translated to the T-μ_{B} plane using the hadron gas model [58], which is presented in Fig. 1.4. The NA61/SHINE Collaboration recorded the data on ^{40}Ar+^{45}Sc and ^{208}Pb + ^{208}Pb collisions in 2015 and 2016 are marked by the red box in Fig. 4.1. These data sets were analyzed within the doctoral studies, and the results are reported in this thesis.

After the Long Shutdown 2, the upgraded NA61/SHINE experiment continues measurements at CERN SPS. They focus on the open charm hadron production in Pb+Pb collisions, nuclear fragmentation cross sections for cosmic ray physics, and hadron production in hadron-induced reactions for neutrino physics. The NA61/SHINE detector was upgraded to meet the open charm measurement requirements. The details of the upgrade are described in Ref. [125].

4.2 Overview of the NA61/SHINE detector

The layout of the NA61/SHINE large-acceptance hadron spectrometer before LS2 is presented in Fig. 4.2 [56]. The core components of the set-up are four large-volume Time Projection Chambers (TPCs): VTPC-1, VTPC-2, MTPC-L, and MTPC-R. TPCs are the main tracking

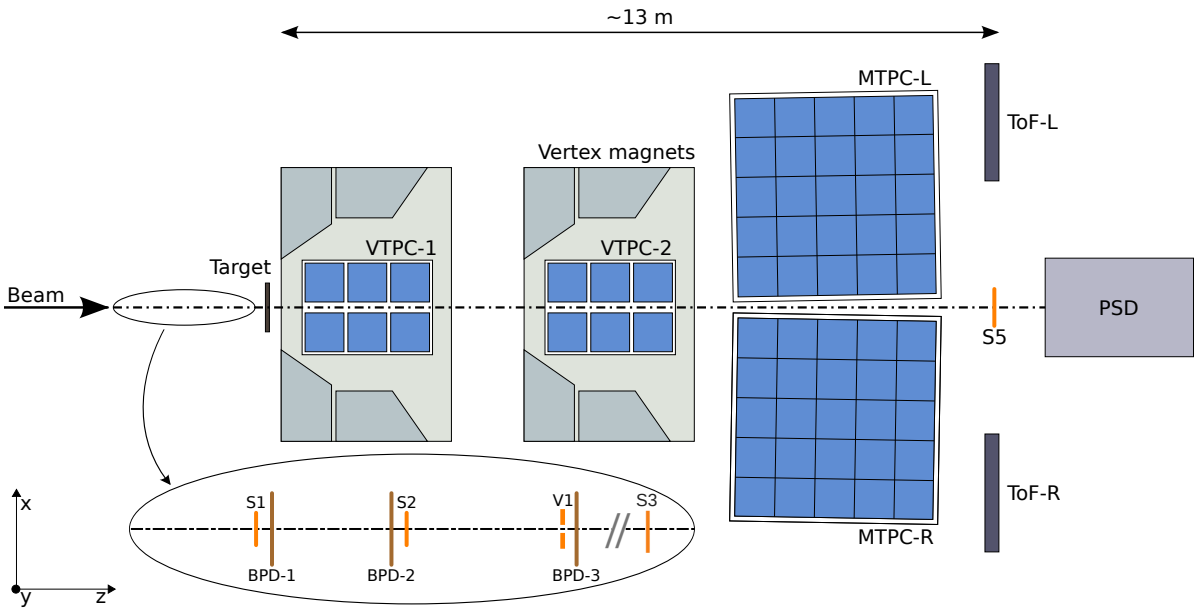

Figure 4.2 An illustration showing the NA61/SHINE detector setup (not to scale). The four Time Projection Chambers (TPCs) are important. The inside of superconducting magnets contains VTPCs. Two Time of Flight (ToF) walls are located downstream of the MTPCs. The Projectile Spectator Detector (PSD) is on the far right. The figure is taken from Ref. [56].

devices of the NA61/SHINE spectrometer. Two Time of Flight detectors, ToF-L and ToF-R, are placed downstream of the MTPCs. The purpose of the ToF detectors is to improve particle identification. Another component is the Projectile Spectator Detector (PSD), which measures the energy of projectile spectators. The superconducting magnets, large-volume TPCs, and TOF-L/R detectors were inherited from the NA49 experiment [55]. The ^{40}Ar+^{45}Sc data were registered at six beam momenta: p_{beam} = 13*A*, 19*A*, 30*A*, 40*A*, 75*A*, and 150*A* GeV/*c*. A similar configuration was used during the ^{40}Ar+^{45}Sc data-taking campaign, differing only in magnetic field reduction. Upgraded beam and detector configuration was used for ^{208}Pb + ^{208}Pb at 13*A*, 30*A*, and 150*A* GeV/*c* data-taking in 2016. The following subsection briefly discusses key components of the NA61/SHINE facility relevant to this work.

4.2.1 Beamline and beams

NA61/SHINE uses primary and secondary beams consisting of a variety of different ions, delivered by the CERN accelerator complex. The SPS provides the beam with six beam

momenta that NA61/SHINE often uses 13A, 19A, 30A, 40A, 75A, and 150A GeV/c. The maximum momentum of the CERN SPS imposes the upper limit on the beam momentum, while the lower limit is dictated by the beam stability and quality, as the H2 beamline was designed for the maximal SPS momentum. The beams of protons (see Ref. [126]) and ions undergo several acceleration steps to be brought to the desired momentum in the SPS and finally to be extracted to the North Area and transported to NA61/SHINE from the sources.

Ion acceleration chain

The ion acceleration process is illustrated in Fig. 4.3 (*left*). Isotopically pure ^{208}Pb is evaporated

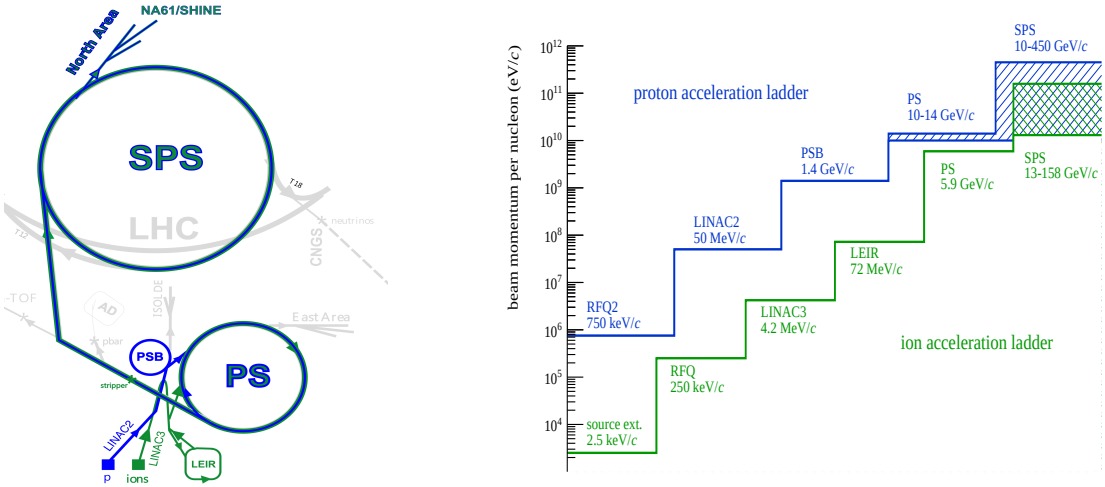

Figure 4.3 *Left:* A schematic diagram of the CERN accelerator chain related to the operation of NA61/SHINE (top view, not to scale). *Right:* A quantitative representation of successive stages of the proton (blue) and ion (green) beam acceleration. Figures are taken from Ref. [56].

for the lead beam, while gas sources are used for other beams. The atoms are ionized in an Electron Cyclotron Resonance (ECR) source with electrons accelerated by repetitive microwave pulses. The ions are electrostatically extracted with the energy of 2.5A KeV/c into the separator, which selects the particular charge state depending on the beam type. After the separator, the beam momentum is raised to 250A KeV/c by the Radio Frequency Quadrupole (RFQ). Then, the Linear Accelerator-3 (LINAC3) brings the beam momentum up to a 4.2A MeV/c momentum. The beam is then injected into the Low Energy Ion Ring (LEIR), reaching the momentum of

72*A* MeV/*c* and passing it to the Proton Synchrotron (PS). In the PS, the ion beam is accelerated to 5.9*A* GeV/*c* and extracted to the Super Proton Synchrotron (SPS). The final acceleration of the ion beam is conducted by the SPS, where the beam reaches a momentum of up to 150*A* GeV/*c*.

The consecutive steps of the ion acceleration process and corresponding momentum values are illustrated in Fig. 4.3 (*right*).

H2 beamline

The H2 beamline delivers the beam to NA61/SHINE detectors in CERN North Area after final acceleration in SPS. Using a pair of large spectrometers, the beamline selects a beam type based on its rigidity, allowing the production of secondary hadron and ion beams. Downstream collimators lower beam intensity to a few 10^5 ions per spill lasting typically 10 sec [127]. Detectors provide precise information on the beam's position, profile, and intensity.

Beam detectors

A set of detectors, including scintillators and three gaseous beam position detectors are situated upstream of the target in the beamline. These detectors provide precise information on the charge, position, and timing of the incoming beam particles. Additionally, two scintillating counters (S3, S5) are located downstream of the target and serve as interaction detectors, allowing for triggering inelastic interactions of the beam particles inside the target.

Figures depicting the schematic diagram of the beam counters used for ^{40}Ar + ^{45}Sc and ^{208}Pb + ^{208}Pb data collections are presented in Figs. 4.4 and 4.5, respectively, and those are briefly discussed below:

(i) **S1 counter:** The first counter on the beamline is equipped with four fast photo-multiplier tubes (PMTs). It collects and transforms scintillation light into electrical signals for the readout and trigger electronics. S1 provides precise timing for the experiment.

(ii) **S2 counter:** The S2 counter on the beamline is used in coincidence with S1 in the trigger logic. The amount of light produced by the scintillator is proportional to the squared charge Z^2 of the incoming particle, allowing for the selection of beam particles with

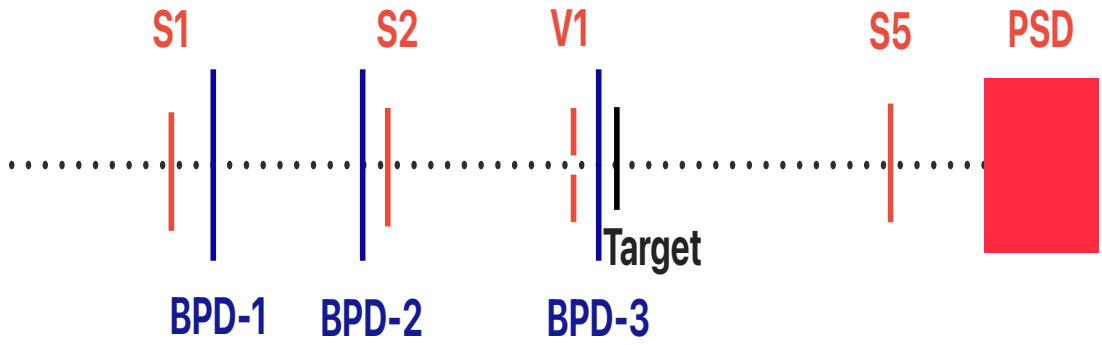

Figure 4.4 A schematic diagram (not to scale) of the beam counters used in ^{40}Ar+^{45}Sc data-taking campaign in 2015.

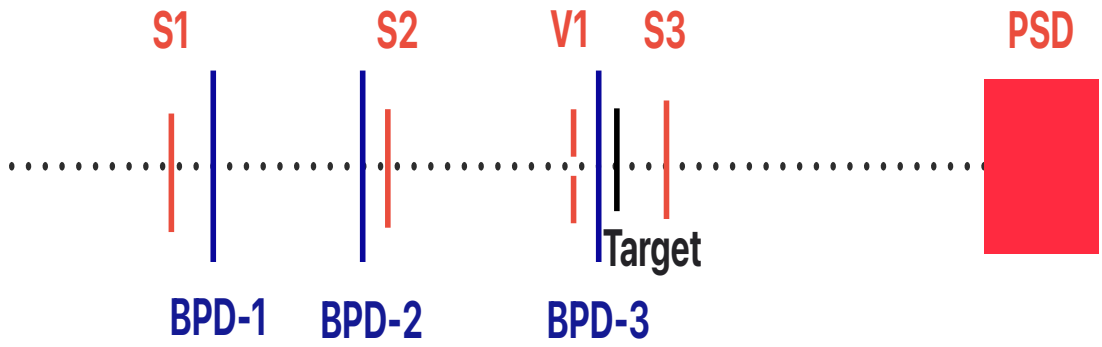

Figure 4.5 A schematic diagram (not to scale) of the beam counters used in ^{208}Pb + ^{208}Pb data-taking campaign in 2016.

different charge states Z in off-line analysis or at the trigger level. In contrast, the V1 plastic scintillator with small holes in the middle is used in anti-coincidence (veto) mode to remove the beam halo and trigger only on the central part of the beam.

(iii) **S3, S5:** In the NA61/SHINE beamline, plastic scintillator detectors called S3 and S5 are used downstream of the target to detect interactions of the beam particles. The interaction between the last counter running in coincidence (typically S2) and the given interaction

counter is signaled by the absence of the beam particle signal in this counter. Therefore, these counters are used in anti-coincidence mode in the trigger logic to detect interactions. A single interaction counter is typically selected for triggering, depending on the beam type and the detector configuration.

(iv) **BPDs:** Beam Position Detectors (BPDs) are placed along the beamline upstream of the target to measure each beam particle trajectory. A schematic view of a single BPD detector is shown in Fig. 4.6.

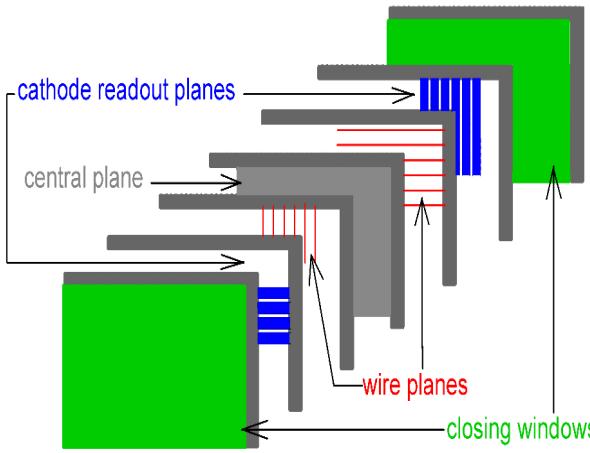

Figure 4.6 A schematic layout of the BPD detector. The figure is taken from Ref. [56].

BPDs are gas detectors that use a mixture of Ar and CO_2 (80:15) to detect particles. Each BPD has two orthogonal planes of readout strips that allow for position measurement in the x-y plane. This measurement can extrapolate the trajectory of beam particles to the target z-plane with a precision of around 100 μm.

The parameters of the counters used for ^{40}Ar + ^{45}Sc and ^{208}Pb + ^{208}Pb data-taking campaign are summarized in Table 4.1.

Table 4.1 Summary of beam detector parameters: dimensions, positions along the beamline (z coordinates) used for ^{40}Ar + ^{45}Sc and ^{208}Pb + ^{208}Pb data-taking campaign.

detector	dimensions (mm)	hole (mm)	position (m)
S1	$60 \times 60 \times 5$		-36.42
S2	$\phi = 28 \times 2$		-14.42
S3	$\phi = 26 \times 5$		-6.58
S5	$\phi = 20 \times 5$		9.80
V1	$100 \times 100 \times 10$	$\phi = 8$	-6.72
V1^p	$100 \times 100 \times 10$	$\phi = 8$	-6.72
BPD1	$48 \times 48 \times 32.6$		-32.60
BPD2	$48 \times 48 \times 32.6$		-14.90
BPD3	$48 \times 48 \times 32.6$		-6.70

4.2.2 Triggering systems

The NA61/SHINE trigger system uses analog signals from beam detectors (BPDs are not included) to classify events and limit stored data, when, for instance, an interaction with a target did not take place. It can include any signal arriving up to ≈300 ns after the S1 signal and has four independent trigger configurations (T1-T4).

Table 4.2 Trigger definitions used during the ^{40}Ar+^{45}Sc and ^{208}Pb + ^{208}Pb data-taking campaign.

Trigger	Description	Definition		Fraction of data	
		Ar+Sc	Pb+Pb	Ar+Sc	Pb+Pb
T3	unidentified beam	S1 · S2	S1 · S2	0.18%	0.80%
T1	identified beam	T3 · $\overline{\text{V1}}$	T3 · $\overline{\text{V1}}$	1.16%	10.4%
T4	unidentified beams interaction	T1 · $\overline{\text{S5}}$	T1 · $\overline{\text{S3}}$	7.13%	67.13%
T2	identified beams interaction	T4 · $\overline{\text{PSD}}$	T4 · $\overline{\text{PSD}}$	92.61%	21.61%

The Projectile Spectator Detector (see Sec. 4.2.5) also contributes to the trigger logic in veto mode. Collimators in the beam line were adjusted to obtain beam rates of $\approx 10^4$/sec during the ≈ 10 sec spill and a super-cycle time of 32.4 sec. Trigger definitions used during the ^{40}Ar + ^{45}Sc

and ^{208}Pb + ^{208}Pb data taking are presented in Table 4.2.

After the T1-T4 signals are generated, they are sent to the prescaler module. The role of the module is to select a given fraction of triggers of a given type for recording.

4.2.3 Targets

The target used in ^{40}Ar + ^{45}Sc data-taking of the NA61/SHINE experiment was a stack of six square ^{45}Sc plates of 2.5×2.5 cm^2 area and 1 mm thickness. During the ^{208}Pb + ^{208}Pb data-taking campaign, a square ^{208}Pb plate, with an area of 2.5×2.5 cm^2 and a thickness of 1 mm was utilized as a target. The detailed specifications for ^{45}Sc and ^{208}Pb targets are in Appendix C. The targets were placed about 80 cm upstream of the VTPC-1. The targets are placed in a specialized holder with a helium atmosphere to minimize interactions with air. Targets can be easily removed or inserted using a pneumatic movement system for data collection. The data were taken using two target configurations: target inserted (target IN) and target removed (target R). Approximately 90% of accumulated statistics were collected with target IN.

Table 4.3 A summary of target IN and target R statistics of the collected Ar+Sc and Pb+Pb data

p_{beam} (GeV/c)	Target IN	Target R
^{208}Pb + ^{208}Pb		
13A	$2.67 \cdot 10^6$	$9.43 \cdot 10^5$
30A	$4.69 \cdot 10^6$	$1.35 \cdot 10^6$
^{40}Ar + ^{45}Sc		
13A	$3.59 \cdot 10^6$	$2.32 \cdot 10^5$
19A	$3.70 \cdot 10^6$	$2.34 \cdot 10^5$
30A	$4.83 \cdot 10^6$	$2.64 \cdot 10^5$
40A	$8.91 \cdot 10^6$	$8.75 \cdot 10^5$
75A	$4.37 \cdot 10^6$	$2.94 \cdot 10^5$

A summary of target IN and target R statistics of the collected Ar+Sc and Pb+Pb data is summarized in Table. 4.3. The target R data was collected to correct for interactions of beam

particles with the material surrounding the target (off-target interactions).

The purity of the ^{45}Sc and ^{208}Pb target was measured [128] at Jan Kochanowski University in Kielce, Poland using the WDXRF method [129]. The content of ^{45}Sc in the ^{45}Sc target and ^{208}Pb in the ^{208}Pb target was about 99.3% and 99.4%, respectively. The measurements of the ^{45}Sc and ^{208}Pb target impurities using the WDXRF technique are summarized in Table C.2. The most abundant contaminants in the target were identified to be: Ti, Al, Fe, Cu, W, and Ta. The influence of these other elements on the mean multiplicity and multiplicity fluctuations of negatively and positively charged particles in the SPS energy range is reported in Ref. [128].

In the case of ^{40}Ar + ^{45}Sc collisions, the presence of Ta and W nuclei in the ^{45}Sc target was mostly responsible for the asymmetric widening of mean multiplicity distributions. The relative change of second order moments [128] was 3.9% for forward kinematical acceptance, defined by $y_\pi > 0$. In contrast, for ^{208}Pb + ^{208}Pb collisions [128], there was no influence of impurities for the analyzed mean multiplicity distributions, and no significant relative changes were observed in the second-order moments for forward kinematical acceptance. This bias was significantly smaller compared to the estimated bias observed from pure (smeared) and reconstructed EPOS model (see Sec. 7).

4.2.4 Time Projection Chambers

In high-energy physics, TPC is a type of particle detector that employs electric and magnetic fields and a sensitive volume of gas or liquid to reconstruct the trajectory or interaction of particles in three dimensions. The TPCs track reconstruction efficiency and resolution of kinematic quantities were studied using a simulation of the detector. Estimates were obtained by matching generated tracks to their reconstructed partners. Overall TPCs track reconstruction efficiency around 90% [56]. The principle of TPC operation is discussed in Ref. [126]. The main components of TPCs relevant to this study are briefly discussed below.

VTPCs

The VTPC-1 and VTPC-2 are positioned amidst two large superconducting magnets, VERTEX-1 and VERTEX-2. The VERTEX magnets generate a magnetic field that is anti-parallel to the

y-axis and can produce a total bending power of up to 9 Tm. This magnetic field orientation causes the positively charged particles' trajectories to bend towards the x-direction, whereas the negatively charged particles are directed towards the -x direction. By precisely measuring the deflection of the charged particle track, the particle's momentum and charge sign can be determined. The TPC momentum resolution [55] is parameterized by $dp/p^2 = 0.3 \times 10^4\,(\text{GeV}/c)^{-1}$ for particles in range 4-100 GeV/c. The magnitude of the field in the VERTEX magnets varies for each beam momentum to achieve optimal acceptance in the collision center-of-mass reference frame. The NA61/SHINE tracking and reconstruction software use an accurate magnetic field map to compensate for the magnetic field inhomogeneities at the edges of the VTPC active volumes.

MTPCs

Two large-volume Main TPCs, MPTC-L and MTPC-R, are placed downstream to the magnets, symmetrically around the beam. The MTPCs improve the accuracy of the energy loss measurement ($\sigma(dE/dx)\big/dE/dx \geq 4\%$) and provide precise tracking of charged particles toward the ToF detectors.

Particle identification

In TPCs, the energy lost by different charged particles can be measured using dE/dx, which refers to the energy loss per unit length. The NA61/SHINE dE/dx resolution [55] is parameterized as $38\%/\sqrt{N}$, where N is the total number of clusters on a track. A combination of energy and momentum measurements allows particle identification (see Chapter 5.2.7) using the Bethe-Bloch formula [130] (see Appendix D).

4.2.5 Projectile Spectator Detector

The Projectile Spectator Detector (PSD) [131] is a forward hadron calorimeter used to measure energy of projectile spectators in nucleus-nucleus collisions. A schematic view of PSD is shown in Fig. 4.7. PSD consists of 44 modules covering a transverse area of 120×120 cm^2. The central part of PSD has 16 smaller modules of size 10×10 cm^2, while the outer part comprises

28 modules of size 20×20 cm^2. Each module contains 60 pairs of lead and scintillator plates, and has a longitudinal length of 120 cm corresponding to 5.7 nuclear interaction lengths. To address the issue of hadronic showers created by Ar ions (about 12%) [125] escaping through the rear side of the calorimeter, a short module [131] was added during 2016 ^{208}Pb + ^{208}Pb data collection. The short module comprises 12 lead/scintillator layers with thicknesses of 16 mm and 4 mm, respectively, and is tied together and placed in a 0.5 mm thick steel box. The transverse size of the module is 10×10 cm^2.

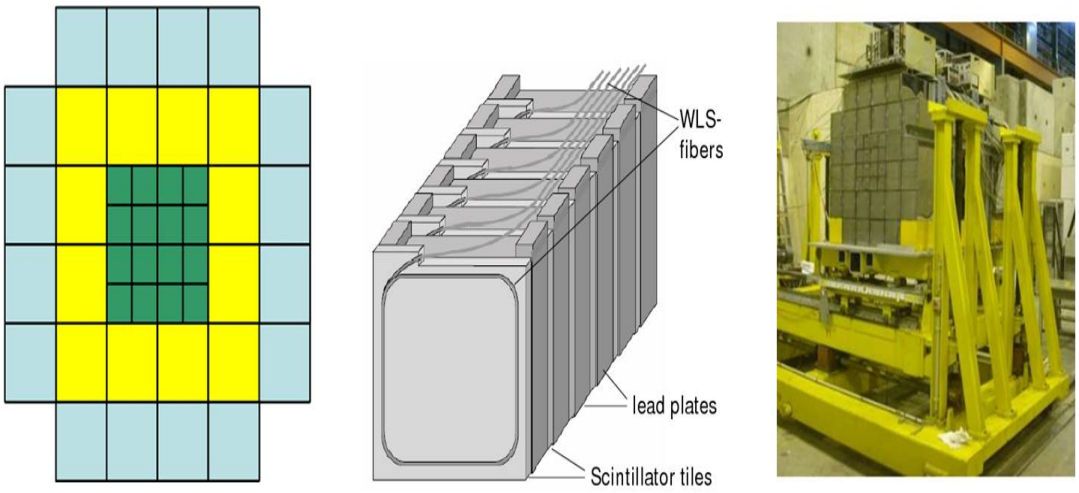

Figure 4.7 A schematic front view (*left*), single module (*center*), and the dimly assembled (*right*) PSD is shown here. Figures are taken from Ref. [56].

In order to select the ^{40}Ar + ^{45}Sc and ^{208}Pb + ^{208}Pb collisions, a low PSD energy value is necessary. This energy is mostly emitted in the area where projectile spectators are mostly populated, known as central collisions. Selecting collisions based on forward energy is called centrality selection (see Sec. 5.1.3). The PSD acceptance maps [132] were used to calculate the energy of the forward spectator in a Monte-Carlo event generator (see Sec. 4.3.2). These maps correspond to the acceptance of the PSD detector and are based on three-dimensional kinematic regions (rigidity, transverse rigidity, and azimuthal angle). Furthermore, the precise measurement of the energy carried by projectile spectators enables the extraction of the number of interacting nucleons from the projectile with a precision of one nucleon. The high energy

resolution of PSD is crucial for studying fluctuations in nucleus-nucleus collisions. In order to quantify the performance of PSD, the energy resolution can be parameterized [133] by,

$$\frac{\sigma_E}{E} = 60\%/\sqrt{E\ (\text{GeV})/(1\ \text{GeV})}, \tag{4.1}$$

and it has a good transverse uniformity [133].

4.3 Data processing and Monte-Carlo simulations

Before final data analysis, raw signals from TPCs and other detectors undergo a complex process of calibration [134] and reconstruction [134] of physical quantities such as charge, momentum, or energy loss. The calibration process includes time-dependent correction of electron drift velocity or specific energy loss per unit length to enhance data quality. Tracks are reconstructed by combining clusters and fitting their momenta. The reconstruction procedure is briefly discussed below (see Sec. 4.3.1). A Monte-Carlo simulation is conducted in the final phase to derive the geometrical acceptance of the detector, the contribution of weak decay, and the interactions of primary particles with the detector (see Sec. 4.3.2).

4.3.1 Reconstruction of tracks

The reconstruction process translates raw quantities recorded by the detector into particle trajectories and associated quantities. An example of a reconstructed ^{208}Pb + ^{208}Pb collision at 30*A* GeV/*c* is presented in Fig. 4.8. Starting with detector raw data, the event reconstruction procedure can be broken into the following steps, performed sequentially:

BPD reconstruction

An algorithm extracts beam particle positions from three BPDs and fits them to a straight line to determine particle trajectory.

TPC reconstruction

(i) **Cluster finding:** In the first step of the TPC reconstruction algorithm, cluster finding searches for signals in TPC pads and time slices. Groups of signals present in adjacent

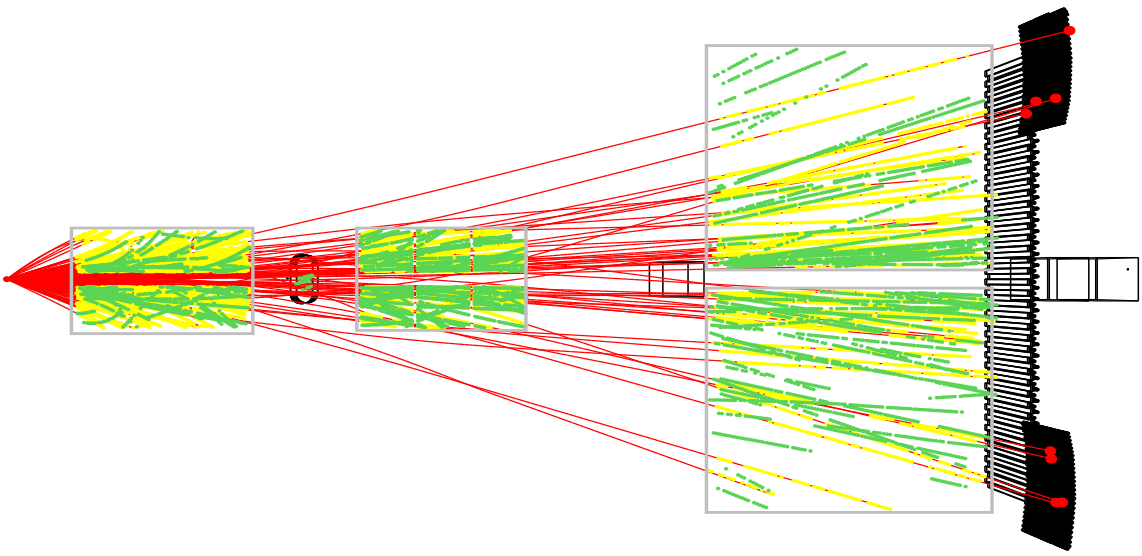

Figure 4.8 An example of reconstructed ^{208}Pb + ^{208}Pb collision at 30*A* GeV/*c* is shown. Green points represent clusters on reconstructed local tracks. Yellow points represent clusters that belong to tracks from the main vertex, and red lines show reconstructed global vertex tracks (for reference, see the detector layout in Fig. 4.2).

pads and time slices are defined as clusters. If two distinct maxima are found in the connected charge region, this algorithm assumes they belong to two separate clusters and splits them in two. The position of the cluster is calculated with the center of gravity method using measured charges as weights. In events with a high multiplicity, such as ^{208}Pb + ^{208}Pb or ^{40}Ar+^{45}Sc, the number of clusters is exceptionally high, and the distances between them are extremely small. Therefore, it may not be possible to identify all clusters belonging to the same particle's track. The reconstruction algorithm was optimized to identify clusters originating from the same particle's track while minimizing the inclusion of clusters from adjacent paths and utilizing the detector's time dependence.

(ii) **Local tracking in each TPCs:** Clusters in close proximity are merged into local track fragments for each TPC, requiring geometrical topology: straight lines in MTPCs and curved ones in VTPCs due to the magnetic field.

(iii) **Global tracking:** Track pieces from multiple TPCs are merged, and the momenta of the connected tracks are fitted, accounting for magnetic field distribution within and between TPCs.

Reconstruction of vertices

(i) **Finding interaction vertex:** Finding the interaction vertex involves extrapolating merged tracks upstream to identify a single common vertex. The vertex's z position is then fitted based on all TPC tracks in a given event. The x and y coordinates of the vertex are calculated by extrapolating the beam track measured by the BPDs to the z coordinate of the vertex. The momenta of tracks are re-fitted with the interaction vertex as an additional constraint. The distance in the x-y plane between the BPD-measured vertex position and the extrapolated track is referred to as the impact point, and it is a measure used to reject non-vertex tracks.

(ii) **Finding secondary vertices:** The algorithm tries to match pairs of tracks with a common secondary vertex to identify if they came from decay.

Additional steps of the reconstruction algorithm are the ToF reconstruction and the PSD reconstruction. Following the reconstruction, the data consists of tracks with the following parameters:

(i) electric charge sign,

(ii) momentum vector at the interaction vertex.

(iii) average energy loss $\mathrm{d}E/\mathrm{d}x$,

(iv) number of measured and potential points in each TPC,

(v) coordinates of the impact point (the distance between the track extrapolated to the target z-plane and the reconstructed vertex).

4.3.2 Monte-Carlo simulations

Monte Carlo (MC) simulations are utilized in NA61/SHINE to correct analysis results for detector efficiency, geometrical acceptance, and reconstruction algorithms. An MC generator is used to mimic particle production (see Chapter 6), and Epos1.99 event generator is used in this study, as it has reasonable agreement with previous SHINE measurements and had consistent developer support. Epos utilizes both partons and pomerons (Parton ladders) in

its multiple dispersal technique. The particles produced by Epos1.99 are then inserted into a detector simulation using the Geometry And Tracking (Geant3) software, which allows the simulation of important physical processes such as particle decay and secondary interactions. The Detector Response Simulator then processes the output from Geant3 in order to generate TPC clusters that have position and charge. The resulting MC events then go through the same reconstruction procedure as the actual data, and a matching procedure is carried out to identify the corresponding simulated track for each reconstructed track. Finally, reconstructed MC events are run through a simulation of the PSD detector to determine the deposited energy.

Chapter Five

Event and track selection

The goal of these analyses is to search for QCD CP (see Sec. 1.4.2) by measuring the SSFMs (see Sec. 2.1) of selected proton candidates within the analyses acceptance in 0–10% *central* ^{208}Pb + ^{208}Pb collisions at 13*A* and 30*A* GeV/*c* and ^{40}Ar + ^{45}Sc collisions at 13*A*–75*A* GeV/*c*. Not all recorded events were eligible for analysis as *central* collisions in the target, and not all recorded tracks were the *primary products* of such collisions. Therefore, optimization was done by introducing selection criteria for events and tracks. This chapter will present the event and track selection for ^{208}Pb + ^{208}Pb and ^{40}Ar + ^{45}Sc data sets. The selection procedure involves the following steps:

(i) event selection including the *centrality* selection (Sec. 5.1),

(ii) single-track selection including proton candidate selection (Sec. 5.2),

(iii) single-particle acceptance maps (Sec. 5.3),

(iv) two-particle acceptance map (mTTD cut) (Sec. 5.4).

As an illustration of the selection procedure, the distributions for ^{208}Pb + ^{208}Pb collisions at 13*A* GeV/*c* and ^{40}Ar + ^{45}Sc collisions at 75*A* GeV/*c* are shown in this chapter. Distributions before and after the event and track selection for other analyzed ^{208}Pb + ^{208}Pb and ^{40}Ar + ^{45}Sc data sets are documented in Ref. [135].

5.1 Event selection

The sub-sample consisting of central interactions of beam-ions ^{40}Ar (or ^{208}Pb) with ^{45}Sc (or ^{208}Pb) target nuclei selected on the trigger level - T2 trigger (see Sec. 4.2.2)- was analyzed. A sequence of event selection criteria was imposed on the T2 trigger sample, ensuring the highest quality of the analyzed data and proper, well-defined event *centrality* interval. There are two sets of event selection criteria: upstream or non-biasing cuts and downstream or biasing cuts. Also, before the physical event selection of target-inserted data sets, a subset of events has to be excluded due to malfunctioning of PSD (see Sec. 4.2.5) and/or other detectors (see Ref. [135]).

5.1.1 Non-biasing event selection criteria

The upstream of the target or non-biasing cuts do not employ interaction-dependent variables. They reduce the number of unwanted events without influencing the properties of wanted events. These are cuts on the beam's position, composition, and timing.

Beam quality

A precise measurement of the beam particle trajectory was needed to determine the interaction. The presence of the signal from BPD3 (see Sec. 4.2.1), together with a signal from either of the other beam position detectors (BPD-1 or BPD-2), was required. Such conditions allow the fitting of the beam trajectory and its extrapolation to the target area. Furthermore, it also assures that the beam particle did not interact upstream of BPD3. Examples of beam position distributions for ^{208}Pb + ^{208}Pb collisions at 13A GeV/c and ^{40}Ar + ^{45}Sc collisions at 75A GeV/c are shown in Figs. 5.1 and 5.2, respectively. The *left* and *right* distributions are represented before and after the beam quality cut, respectively.

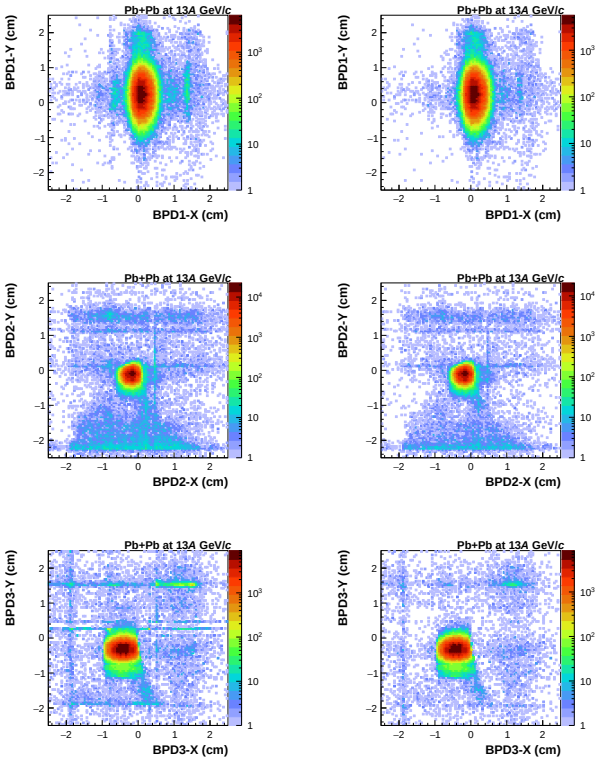

Figure 5.1 Examples of beam position distributions registered by all three BPDs for ^{208}Pb + ^{208}Pb collisions at 13*A* GeV/*c*. BPD-1 (*top*), BPD-2 (*middle*) and BPD3 (*bottom*) distributions, before (*left*) and after (*right*) the BPD cuts, are shown.

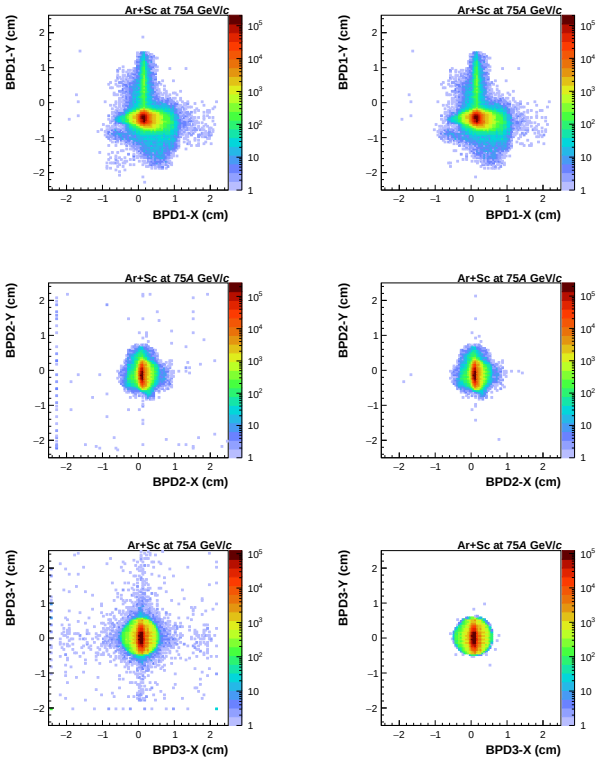

Figure 5.2 Examples of beam position distributions registered by all three BPDs for ^{40}Ar + ^{45}Sc collisions at 75*A* GeV/*c*. BPD-1 (*top*), BPD-2 (*middle*) and BPD3 (*bottom*) distributions, before (*left*) and after (*right*) the BPD cuts, are shown.

BPD3 charge

Additional information is provided to verify the charge of the beam ions measured by the BPD3 counter. Example distributions of the charge signal obtained on X and Y planes of BPD3 for ^{208}Pb + ^{208}Pb collisions at 13*A* and ^{40}Ar + ^{45}Sc collisions at 75*A* GeV/*c* are shown in Fig. 5.3. The red rectangular region in both distributions represents the region selected for these analyses. The upper and lower limits of the BPD3 charge used to select events for ^{208}Pb + ^{208}Pb and ^{40}Ar + ^{45}Sc data sets are summarized in Table 5.1.

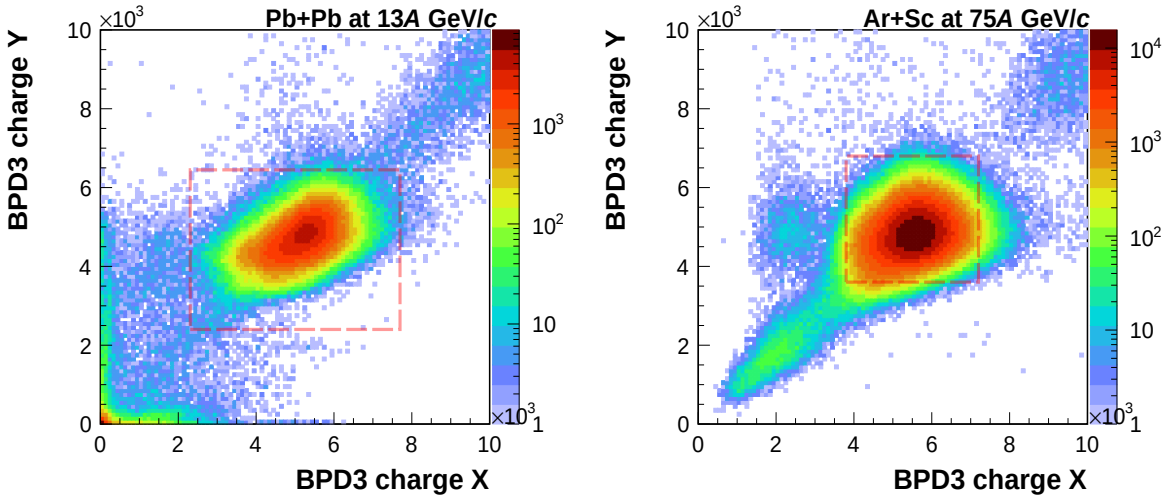

Figure 5.3 Examples distributions of BPD3 charge Y versus BPD3 charge X for ^{208}Pb + ^{208}Pb collisions at 13*A* GeV/*c* and ^{40}Ar + ^{45}Sc collisions at 75*A* GeV/*c*. The red rectangular regions in both distributions represent the graphical cut used for event selection. Clouds outside the red rectangular area are due to secondary interactions or off-time beam particles.

Table 5.1 The BPD3 charge cut values used to select events for ^{208}Pb + ^{208}Pb collisions at 13*A* and 30*A* GeV/*c* and ^{40}Ar + ^{45}Sc collisions at 13*A*–75*A* GeV/*c*.

	BPD3 charge X		BPD3 charge Y	
p_{beam} (GeV/*c*)	lower limit	upper limit	lower limit	upper limit
^{208}Pb + ^{208}Pb				
13*A*	2307	7697	2400	6450
30*A*	2000	8408	2150	6650
^{40}Ar + ^{45}Sc				
13*A*	3000	7900	2500	6800
19*A*	3500	6500	3200	6000
30*A*	3400	7400	2800	6600
40*A*	3500	8000	3000	7000
75*A*	3800	7200	3600	6800

Off-time beam particles

This criterion reduces the contribution of events in which there was an additional beam particle that could interact with the target or the detector material in close time proximity to the triggering particle. If it is too close in time, it may be mistaken for the product of the collision or may interact with the target, producing a second collision that is indistinguishable by the reconstruction software. Such events may bias the fluctuation measurements. The main selection tool is the distribution of the time in which beam particles pass through the S1 counter (see Sec. 4.2.1) with respect to the trigger signal (generated by the interaction beam ion). This selection criteria usually refers to the WFA (WaveForm Analyzer) cut.

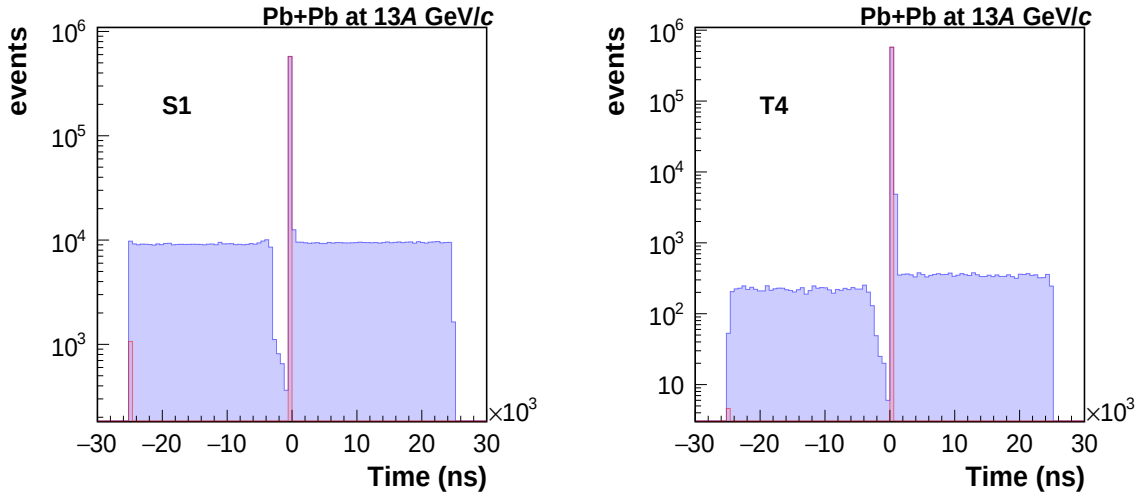

Figure 5.4 Example distributions of beam particles time measured by the S1 counter (*left*) and obeying the T4 trigger (*right*) with respect to a trigger signal in target-inserted ^{208}Pb + ^{208}Pb collisions at 13*A* GeV/*c*. The blue line with blue-shaded distributions and the red line with red-shaded distributions are before and after the WFA cut.

In the ^{208}Pb + ^{208}Pb event selection, the WFA cut selects events with no off-time beam particle within the $\pm$ 25 μs window with respect to the trigger particle S1 signal. In the ^{40}Ar + ^{45}Sc event selection, the WFA cut selects events with no off-time beam particle within the $\pm$ 4 μs window with respect to trigger particle S1 signal. Additionally, no off-time particle that gives the T4 signal (see Sec. 4.2.2) can be detected within the $\pm$ 25 μs window.

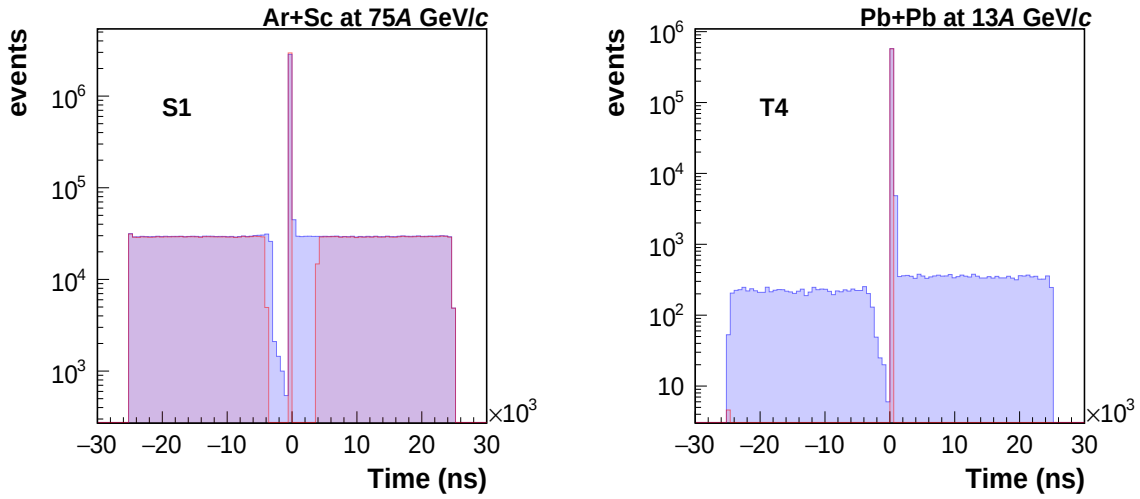

Figure 5.5 Example distributions of beam particles time measured by the S1 counter (*left*) and obeying the T4 trigger (*right*) with respect to a trigger signal in target-inserted ^{40}Ar + ^{45}Sc collisions at 75*A* GeV/*c*. The blue line with blue-shaded distributions and the red line with red-shaded distributions are before and after the WFA cut.

Example distributions of beam particles time measured by the S1 counter and obeying the T4 trigger with respect to a trigger signal in target-inserted ^{208}Pb + ^{208}Pb collisions at 13*A* GeV/*c* and ^{40}Ar + ^{45}Sc collisions at 75*A* GeV/*c* are shown in Figs. 5.4 and 5.5, respectively. The blue line with blue-shaded beam particle's time distributions represents before the WFA cut, and the red line with red-shaded beam particle's time distributions represents after the WFA cut.

5.1.2 Biasing event selection criteria

In turn, inappropriately applied downstream of the target or biasing cuts may (and typically do) affect the properties of the wanted events. Typically, these are used to remove the background of non-target interactions or to determine collision *centrality*. Using Monte Carlo simulations, it is possible to estimate and, if needed, correct the effect of these biasing cuts.

Interaction vertex fit quality

This criterion ensures that the interaction vertex is fitted during the reconstruction process and that the fit quality is good enough.

Interaction vertex z position

Example distributions of the fitted vertex z position for the target inserted for ^{208}Pb + ^{208}Pb collisions at 13*A* GeV/*c* and ^{40}Ar + ^{45}Sc collisions at 75*A* GeV/*c* are shown in Fig 5.6. An overview of the fitted vertex z position for the target inserted and target removed in a broad range and an explanation of the origin of different peaks is presented in Fig. E.1 (see Appendix E).

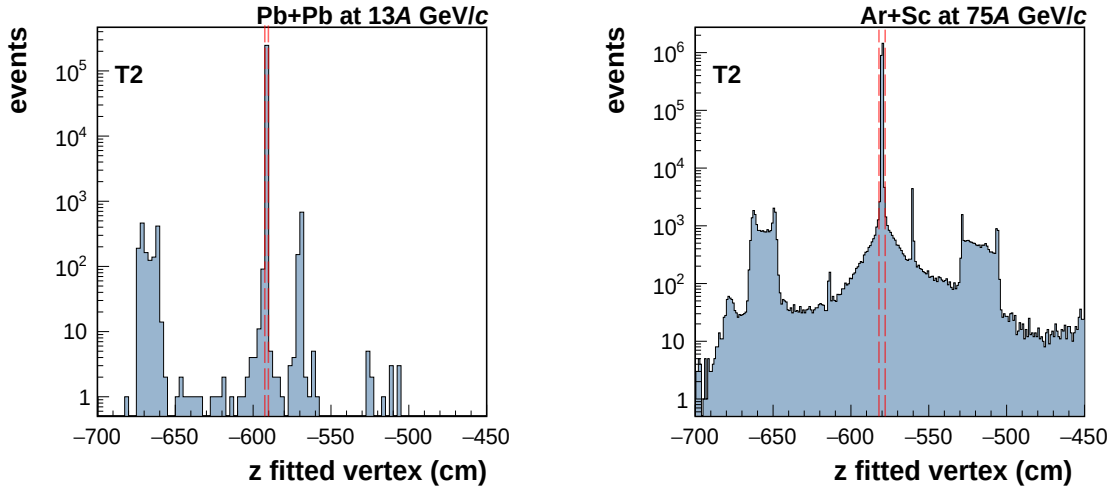

Figure 5.6 Example distributions of the fitted vertex z position for the target inserted data-sets of ^{208}Pb + ^{208}Pb collisions at 13*A* GeV/*c* (*left*) and ^{40}Ar + ^{45}Sc collisions at 75*A* GeV/*c* (*right*). In both distributions, the red lines represent the cut used for event selection.

Further analysis was conducted only for events that have a reconstructed interaction vertex within $\pm$ 1 cm for ^{208}Pb + ^{208}Pb data-sets and $\pm$ 2 cm for ^{40}Ar + ^{45}Sc data-sets form the peak maximum or around. The red lines represent the cut used for event selection for ^{208}Pb + ^{208}Pb collisions at 13*A* GeV/*c* and ^{40}Ar + ^{45}Sc collisions at 75*A* GeV/*c*, shown in Fig. 5.6.

5.1.3 Centrality selection

The energy deposited in the PSD detector, E_{PSD}, is used to determine the *centrality* of collisions. The analysis in this thesis focuses on the 0–10% most *central* ^{40}Ar + ^{45}Sc and ^{208}Pb + ^{208}Pb collisions. The selection process for the *centrality* of ^{40}Ar + ^{45}Sc collisions is discussed in detail in Refs. [136, 137]. Figure 5.7 shows the modules used to determine the *centrality* of ^{40}Ar + ^{45}Sc

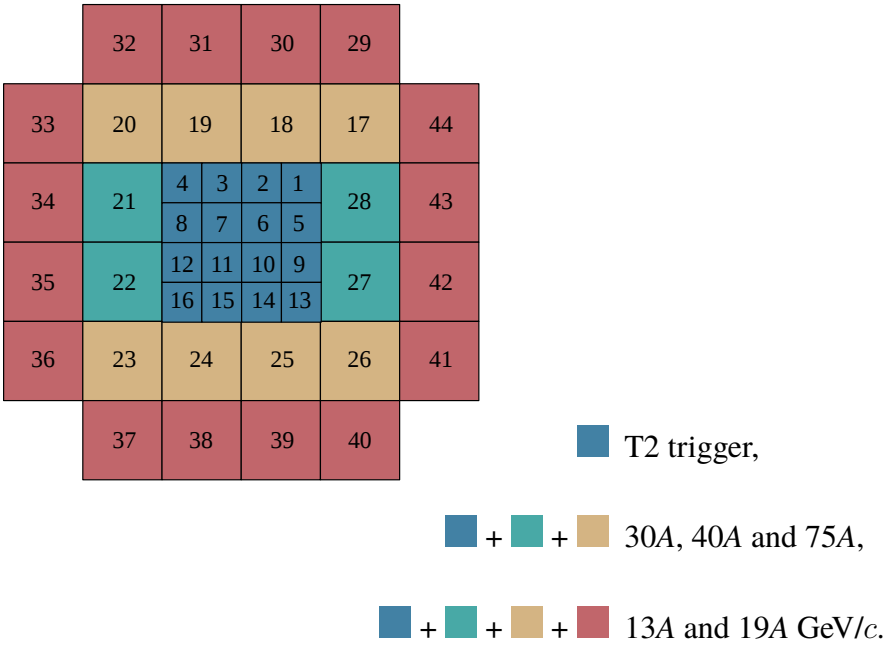

Figure 5.7 Modules used for *centrality* determination were selected based on the anti-correlation between energy and track multiplicity. All modules were used for ^{40}Ar + ^{45}Sc collisions at 13A and 19A GeV/c, while 28 central modules were chosen for 30A, 40A, and 75A GeV/c. For T2 trigger, 16 central modules were used.

data sets. The modules were chosen based on the anti-correlation between the measured energy and the track multiplicity in a given event. All modules were used to determine the *centrality* of ^{40}Ar + ^{45}Sc collisions at 13A and 19A GeV/c, while 28 central modules were chosen for 30A, 40A, and 75A GeV/c. For the T2 trigger, 16 central modules were used. Event selection for data analysis was based on ≈10% of collisions with the lowest value of the energy E_{PSD} measured by a subset of PSD modules (see Fig. 5.7) to optimize sensitivity to projectile spectators. The acceptance resulting from the definition of the forward energy, E_F, corresponds closely to the acceptance (see Sec. 4.2.5) [138] of this subset of PSD modules. Online event selection by the hardware trigger (T2) used a threshold on the sum of electronic signals from the 16 central

modules of the PSD to accept ≈30% of all inelastic interactions (see Table 5.3).

The *centrality* selection of ^{208}Pb + ^{208}Pb collisions at 13*A* and 30*A* GeV/*c* was done using the model and data-based methods. The following section discusses the model-based method, and the data-based method is briefly discussed in Appendix E.

Cross-section determination

An inelastic cross-section (σ_{inel}) represents the cross-section of processes where the initial state particles differ from the final state particles. Such cross-sections are composed of contributions from electromagnetic and strong processes and can be divided into two parts: quasi-elastic (σ_{qe}) and production (σ_{prod}) cross-sections. Quasi-elastic cross-sections involve the process of either target, projectile, or both being fragmented, but no additional hadrons were produced. It is difficult to measure target fragmentation in fixed-target experiments; however, projectile fragmentation is measured by PSD. Production cross-sections result in new hadrons being produced in the final state. The inelastic cross-section can be written as:

$$\sigma_{inel} = \sigma_{qe} + \sigma_{prod} \, . \tag{5.1}$$

The inelastic cross-section from strong interactions of ^{208}Pb + ^{208}Pb collisions at 13*A* and 30*A* GeV/*c* was calculated from the GLISSANDO model [139]. GLISSANDO – GLauber Initial-State Simulation AND mOre, a versatile Monte-Carlo generator for Glauber-like models of the initial stages of ultra-relativistic heavy-ion collisions. The value of inelastic cross-sections of ^{208}Pb + ^{208}Pb collisions at 13*A* and 30*A* GeV/*c* are summarized in Table 5.2.

Probability of inelastic interaction

The probability of inelastic interaction, P_{inel}, defined as a ratio between the beam particles that interacted with the target to all beam particles, can be defined as:

$$P_{inel} = \frac{\sigma_{inel} \cdot \rho \cdot L \cdot N_A}{A}, \tag{5.2}$$

where ρ is the target density, L is the target length, N_A is the Avogadro constant, and A is the atomic number of the target nuclei. The specifications of the ^{208}Pb target are summarized in

Table C.1. The probabilities of inelastic interaction of ^{208}Pb + ^{208}Pb at 13*A* and 30*A* GeV/*c* are listed in Table 5.2.

Centrality determination

For the *centrality* determination of ^{208}Pb + ^{208}Pb collisions at 13*A* and 30*A* GeV/*c*, data sets are analyzed using identified beam trigger (T1 trigger) with unbiasing event selection criteria (see Sec. 5.1.1). All biasing and unbiasing event selection criteria are used to analyze ^{208}Pb + ^{208}Pb data sets using T4 and T2 triggers. All PSD modules, including the short module, are used to calculate the PSD energy of ^{208}Pb + ^{208}Pb collisions at 13*A* and 30*A* GeV/*c* (see Sec. 4.2.5). The PSD energy distributions of ^{208}Pb + ^{208}Pb collisions at 13*A* GeV/*c* using T1, T2, and T4 triggers are shown in Fig. 5.8 (*left*). The distributions are normalized to their integral to the left from the vertical green line, which is assumed to be unbiased by off-target interactions. The dashed vertical red line is at the energy, where the T2 PSD energy distribution has maximum.

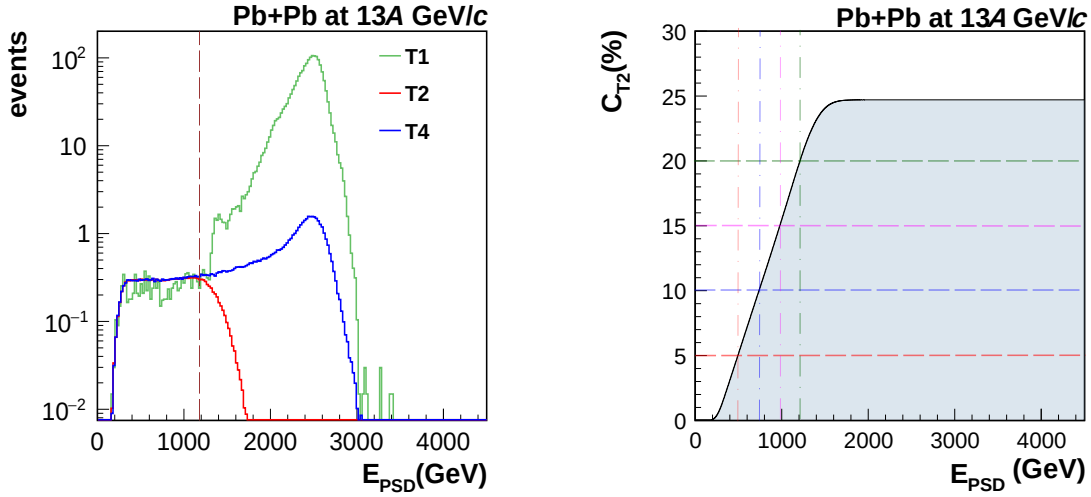

Figure 5.8 *Left:* The PSD energy distributions for ^{208}Pb + ^{208}Pb collisions at 13*A* GeV/*c* using T1, T2, and T4 triggers, see text for details. *Right:* The scaled cumulative PSD energy distribution for ^{208}Pb + ^{208}Pb collisions at 13*A* GeV/*c* data considering the T2 trigger is shown, see text for details.

The total number of inelastic collisions is given by

$$N_{\text{inel}} = P_{inel} \cdot \int_{0}^{\infty} N\left(E_{PSD}^{T1}\right) dE_{PSD}^{T1} \,, \tag{5.3}$$

while the number of T2 inelastic collisions is calculated as

$$N_{T2} = \int_{0}^{\infty} N\left(E_{PSD}^{T_2}\right) dE_{PSD}^{T2} \, . \tag{5.4}$$

The T2 *centrality* is defined as

$$C_{T2} = N_{T2} \Big/ N_{inel} \, , \tag{5.5}$$

and the values of C_{T2} for ^{208}Pb + ^{208}Pb collisions at 13*A* GeV/*c* and 30*A* GeV/*c* are listed in Table 5.2.

Table 5.2 The value of inelastic cross-section due to strong interactions for ^{208}Pb + ^{208}Pb collisions at 13*A* and 30*A* GeV/*c* are calculated from the GLISSANDO [139] model. Probability of inelastic collisions, P_{inel} and the T2 *centrality*, C_{T2} are calculated for ^{208}Pb + ^{208}Pb collisions at 13*A* and 30*A* GeV/*c*.

p_{beam} (GeV/*c*)	inelastic cross-section, σ_{inel} (mb)	P_{in} (%)	C_{T2}
13*A*	6618.0 ± 7.5	2.2	28%
30*A*	6661.7 ± 3.7	2.3	25%

The cumulative distribution of the T2 trigger PSD energy scaled to C_{T2} is shown in Fig. 5.8 (*right*). The dotted horizontal red, blue, magenta, and green lines represent 5%, 10%, 15%, and 20% *centrality* intervals, respectively, and the dotted vertical lines represent the corresponding lowest value of E_{PSD} to select desired central events.

The lowest values of the PSD energy to select 0–10% *central* ^{208}Pb + ^{208}Pb collisions at 13*A* and 30*A* GeV/*c* are listed in Table 5.3. The lowest values of E_{PSD} for different *centrality* intervals from the model-based and the data-based method are listed in Table E.1 (see Appendix E).

Table 5.3 The values of online *centrality* selection by the hardware trigger (T2) of ^{208}Pb + ^{208}Pb collisions and ^{40}Ar + ^{45}Sc collisions are tabulated here. The lowest PSD energy values measured by a subset of PSD modules to select 0–10% of the most central collision events of ^{208}Pb + ^{208}Pb and ^{40}Ar + ^{45}Sc interaction are listed here.

p_{beam} (GeV/c)	T2 *centrality* (%)	E_{PSD} limit (GeV) (for 10% *central* events)
^{208}Pb + ^{208}Pb		
13A	34	825
30A	25	3002
^{40}Ar + ^{45}Sc		
13A	30	143
19A	35	264
30A	30	446
40A	35	666
75A	20	1290.6

Central event selection

The proton intermittency analysis results are presented in Chapter 6 for 0–10% *central* events of ^{40}Ar + ^{45}Sc, and ^{208}Pb + ^{208}Pb collisions using the E_{PSD} limits listed in Table 5.3.

Event statistics

After applying the event selection criteria, the event statistics are summarized in Table 5.4.

Table 5.4 The statistics of selected events for ^{208}Pb + ^{208}Pb collisions at 13*A* and 30*A* GeV/*c* and ^{40}Ar + ^{45}Sc collisions at 13*A*–75*A* GeV/*c*.

p_{beam} (GeV/*c*)	target IN	T2 trigger (good events)	beam quality	beam off-time	vertex fit quality	vertex z position	10% of most *central*
^{208}Pb + ^{208}Pb							
13*A*	$2.67{\cdot}10^6$	$6.58{\cdot}10^5$	$5.82{\cdot}10^5$	$2.50{\cdot}10^5$	$2.49{\cdot}10^5$	$2.46{\cdot}10^5$	$1.17{\cdot}10^5$
30*A*	$4.69{\cdot}10^6$	$9.75{\cdot}10^5$	$8.35{\cdot}10^5$	$4.41{\cdot}10^5$	$4.40{\cdot}10^5$	$4.39{\cdot}10^5$	$1.69{\cdot}10^5$
^{40}Ar + ^{45}Sc							
13*A*	$3.59{\cdot}10^6$	$2.14{\cdot}10^6$	$1.60{\cdot}10^6$	$1.56{\cdot}10^6$	$1.56\cdot10^6$	$1.48\cdot10^6$	$4.97{\cdot}10^5$
19*A*	$3.70{\cdot}10^6$	$2.51\cdot10^6$	$2.00{\cdot}10^6$	$1.93{\cdot}10^6$	$1.92{\cdot}10^6$	$1.83{\cdot}10^6$	$5.24{\cdot}10^5$
30*A*	$4.83{\cdot}10^6$	$3.71{\cdot}10^6$	$2.93{\cdot}10^6$	$2.85{\cdot}10^6$	$2.84{\cdot}10^6$	$2.74{\cdot}10^6$	$9.13{\cdot}10^5$
40*A*	$8.91{\cdot}10^6$	$5.71{\cdot}10^6$	$4.87{\cdot}10^6$	$4.74{\cdot}10^6$	$4.71{\cdot}10^6$	$4.53{\cdot}10^6$	$1.29{\cdot}10^6$
75*A*	$4.37{\cdot}10^6$	$2.89{\cdot}10^6$	$2.44{\cdot}10^6$	$2.37{\cdot}10^6$	$2.36{\cdot}10^6$	$2.32{\cdot}10^6$	$1.16{\cdot}10^6$

5.2 Single-track selection

Among the selected events, many tracks should be rejected from the analysis. The cuts presented in this section are standard NA61/SHINE cuts common for most analyses in the experiment. To select tracks of primary charged hadrons and to reduce the contamination by particles from secondary interactions, weak decays, and off-time interactions, the following track selection criteria were applied.

5.2.1 Track fit quality

For this analysis, only positively charged particles with a converged momentum fit at the main interaction vertex were selected.

5.2.2 Minimal number of clusters

This track cut ensures good momentum reconstruction and track quality. The threshold for the number of clusters in all TPCs (see Sec. 4.2.4) (VTPC1, VTPC2, MTPCL, and MTPCR) was set to 30. The maximum number of clusters in all TPCs is 234 and the maximum number of clusters in VTPCs is 143. In addition, the number of clusters in VTPCs (VTPC1 and VTPC2) has to be larger than 15.

5.2.3 Potential-point ratio

The TPC reconstruction (see Sec. 4.3.1) may fail to merge track fragments from different TPCs. This can generate two or more tracks for a single particle. Such problematic tracks are referred to as split tracks (see Sec. 3.4). For all the selected tracks, the ratio of the number of measured clusters to the number of potential clusters in all TPCs must be greater than 0.5 and less than 1.1. The lower cut removes such split tracks. The number of potential clusters was calculated for vertex tracks. Example potential-point ratio distributions for ^{208}Pb + ^{208}Pb collisions at 13A GeV/c and ^{40}Ar + ^{45}Sc collisions at of 75A GeV/c are shown in Fig. 5.9. The dotted vertical lines show the upper and lower limit of the potential point ratio cut.

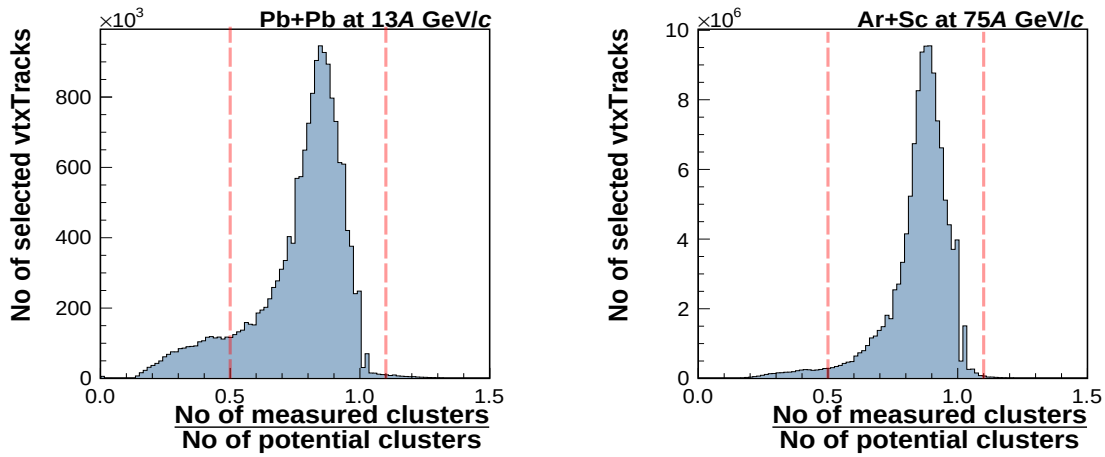

Figure 5.9 Example ratio (the number of measured clusters to potential clusters in all TPCs) distributions for ^{208}Pb + ^{208}Pb collisions at 13*A* GeV/*c* (*left*) and ^{40}Ar + ^{45}Sc collisions at 75*A* GeV/*c* (*right*). The dotted vertical lines show the upper and lower limits of the potential point ratio.

5.2.4 Impact parameters

This track selection criteria enforces that the difference between the track extrapolation to the target z position and the reconstructed interaction vertex is small enough in the x-y plane. It was re-

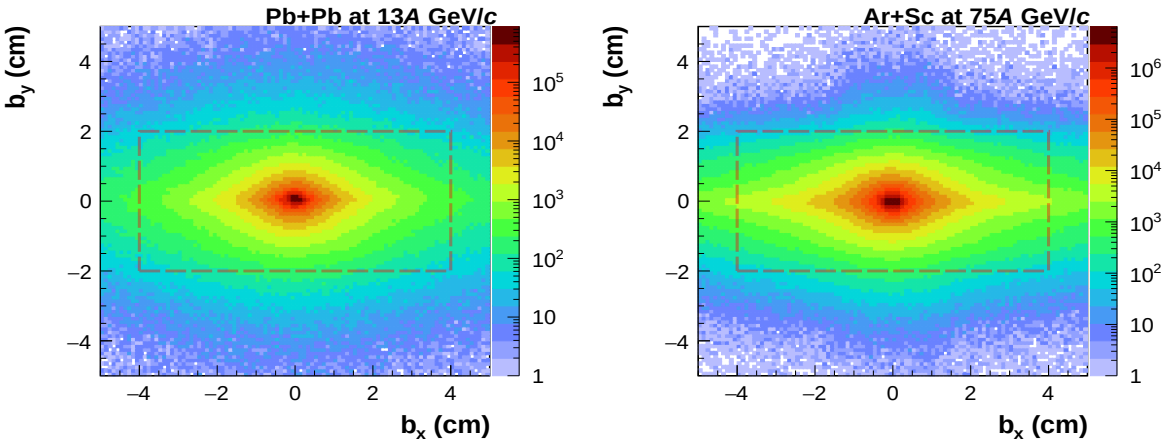

Figure 5.10 Example impact-parameters (along x, b_x and along y, b_y) distributions for ^{208}Pb + ^{208}Pb collisions at 13*A* GeV/*c* (*left*) and ^{40}Ar + ^{45}Sc collisions at 75*A* GeV/*c* (*right*). The dotted red rectangular region represents the region selected for the analysis.

quired to be smaller than 4 cm in the horizontal (bending) plane (b_x) and 2 cm in the vertical (drift) plane (b_y). Example impact-parameter distributions for ^{208}Pb + ^{208}Pb collisions at 13*A* GeV/*c* and ^{40}Ar + ^{45}Sc collisions at 75*A* GeV/*c* are shown in Fig. 5.10. The dotted red rectangular region represents the region selected for the analysis.

5.2.5 Transverse momenta

Only particles with transverse momentum components, $|p_x|$ and $|p_y|$, values less than 1.5 GeV/*c*, were selected for the analysis. Example transverse-momenta (along x, p_x and along y, p_y) distributions for ^{208}Pb + ^{208}Pb collisions at 13*A* GeV/*c* and ^{40}Ar + ^{45}Sc collisions at 75*A* GeV/*c* are shown in Fig. 5.11. The dotted red rectangular region represents the region selected for the analysis.

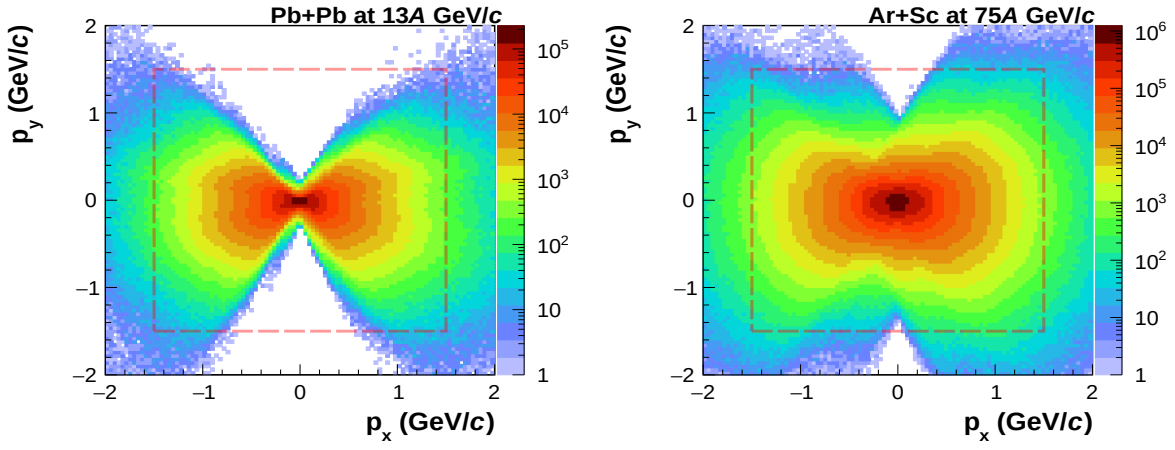

Figure 5.11 Example transverse-momenta (along x, p_x and along y, p_y) distributions for ^{208}Pb + ^{208}Pb collisions at 13*A* GeV/*c* (*left*) and ^{40}Ar + ^{45}Sc collisions at 75*A* GeV/*c* (*right*). The dotted red rectangular region represents the region selected for the analysis.

5.2.6 Track statistics

After applying the selection criteria, the track statistics are summarized in Table 5.5.

Table 5.5 The statistics of selected tracks for ^{208}Pb + ^{208}Pb collisions at 13*A* and 30*A* GeV/*c* and ^{40}Ar + ^{45}Sc collisions at 13*A*–75*A* GeV/*c*.

p_{beam} (GeV/*c*)	track fit quality	minimal number of clusters	potential-point ratio	impact-parameter	transverse-momenta
			^{208}Pb + ^{208}Pb		
13*A*	$5.179 \cdot 10^7$	$3.208 \cdot 10^7$	$2.914 \cdot 10^7$	$2.803 \cdot 10^7$	$2.777 \cdot 10^7$
30*A*	$8.465 \cdot 10^7$	$4.783 \cdot 10^7$	$4.266 \cdot 10^7$	$3.222 \cdot 10^7$	$3.178 \cdot 10^7$
			^{40}Ar + ^{45}Sc		
13*A*	$2.83 \cdot 10^7$	$1.88 \cdot 10^7$	$1.73 \cdot 10^7$	$1.69 \cdot 10^7$	$1.68 \cdot 10^7$
19*A*	$4.04 \cdot 10^7$	$2.62 \cdot 10^7$	$2.46 \cdot 10^7$	$2.40 \cdot 10^7$	$2.39 \cdot 10^7$
30*A*	$9.16 \cdot 10^7$	$5.94 \cdot 10^7$	$5.61 \cdot 10^7$	$5.47 \cdot 10^7$	$5.45 \cdot 10^7$
40*A*	$1.53 \cdot 10^8$	$9.89 \cdot 10^7$	$9.39 \cdot 10^7$	$9.16 \cdot 10^7$	$9.12 \cdot 10^7$
75*A*	$1.93 \cdot 10^8$	$1.23 \cdot 10^8$	$1.18 \cdot 10^8$	$1.17 \cdot 10^8$	$1.16 \cdot 10^8$

5.2.7 Selection of proton candidates

To select proton candidates, only positively charged particles were considered. Their ionization energy loss per unit length ($\mathrm{d}E/\mathrm{d}x$) in TPCs is taken to be greater than 0.5 and less than the proton Bethe-Bloch (see Appendix D) value increased by the 15% difference between the values for kaons and protons while the total momentum is in the relativistic-rise region from 4 to 125 GeV/c.

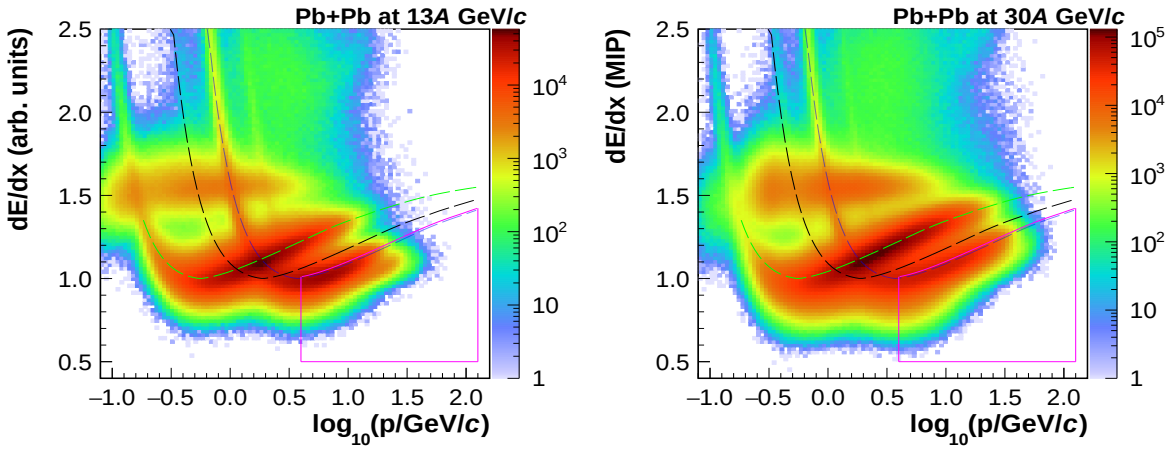

Figure 5.12 Energy loss measured in TPCs versus the logarithm of the total momentum of positively charged particles from selected events of ^{208}Pb + ^{208}Pb collisions at 13A GeV/c (*left*) and 30A GeV/c (*right*), see text for details.

Energy loss measured in TPCs versus the total momentum of positively charged particles from selected events of ^{208}Pb + ^{208}Pb collisions at 13A GeV/c and 30A GeV/c, and ^{40}Ar + ^{45}Sc collisions at 13A–75A GeV/c are shown in Figs. 5.12 and 5.13 respectively. The dashed blue, black, and green lines represent the nominal Bethe-Bloch values for protons, kaons, and pions. The selected region in the $\mathrm{d}E/\mathrm{d}x$–p_{LAB} plane is marked with a magenta line.

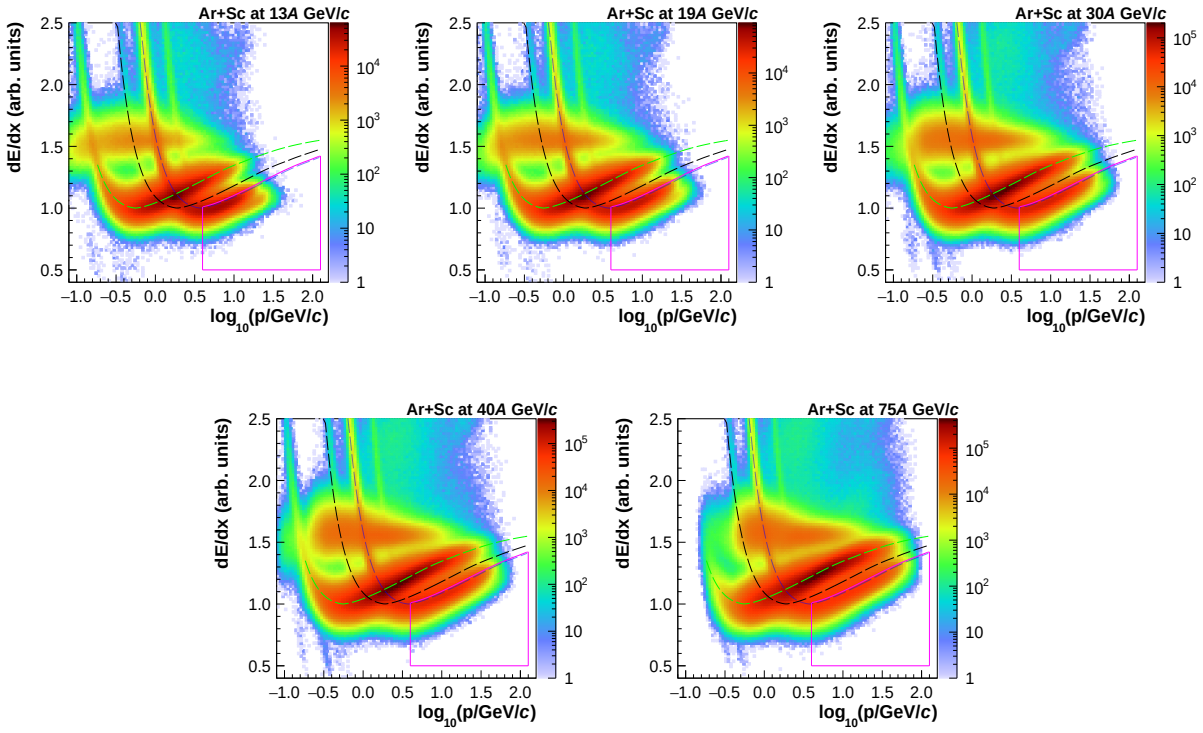

Figure 5.13 Energy loss measured in TPCs versus the logarithm of the total momentum of positively charged particles from selected events of ^{40}Ar + ^{45}Sc collisions at 13*A*–75*A* GeV/*c*, see text for details.

To estimate the fraction of selected protons and kaon contamination in the selected proton candidates fits to the dE/dx distributions in momentum bins were used [140]. The dE/dx fits were done in two-dimensional p and p_T bins using `TShine` software. Gaussian distributions for protons and kaons for each bin were drawn with the help of fit parameters such as mean, amplitude, and standard deviation. Example distributions of dE/dx fit in $7.94 < p < 10.00$ GeV/c and 1.30$< p_T <$1.40 GeV/c bin for ^{208}Pb + ^{208}Pb collisions at 13A and 30A GeV/c and ^{40}Ar + ^{45}Sc collisions at 13A–75A GeV/c are shown in Figs. 5.15 and 5.14.

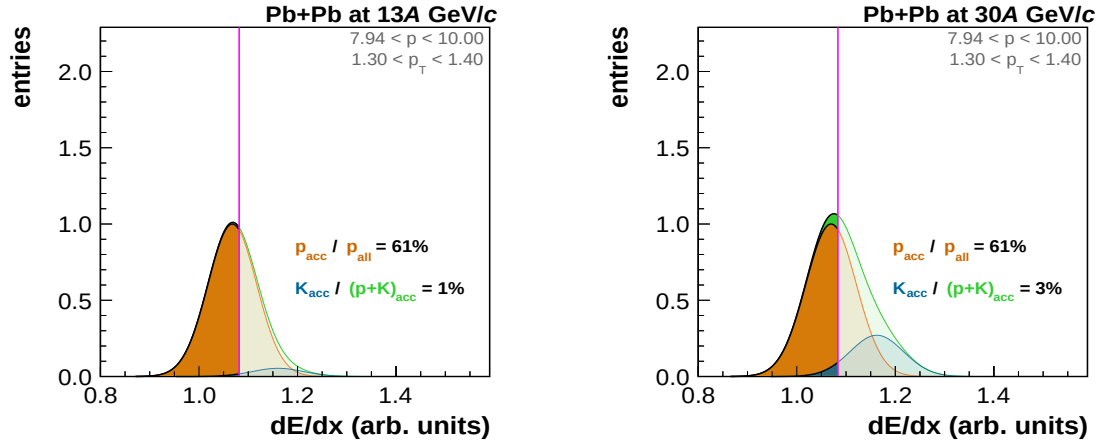

Figure 5.14 Example of Gaussian fits in one of the analyzed p-p_T bins (normalized to proton peak) for ^{208}Pb + ^{208}Pb collisions at 13A (*left*) and 30A GeV/c (*right*). The graphical cut to select proton candidates is marked with a magenta line.

Orange and blue distributions represent protons and kaons Gaussian distribution. The green distribution represents the sum of these two distributions. The vertical magenta line indicates the dE/dx cut used to select a proton candidate. The selection of proton candidates was found to select, on average, approximately 60% of protons (see example in Fig. 5.15). The remaining average kaon contamination is of the order of a few percent, depending on collision energy. The averaging was done over these analyses' p–p_T acceptance. The corresponding random proton losses do not bias the results in the case of independent production in the transverse momentum space [79]. The random losses of proton candidates will affect the results for correlated protons. Thus, the random proton losses due to the proton candidate selection have to be taken into account when calculating model predictions (see Chapter 7).

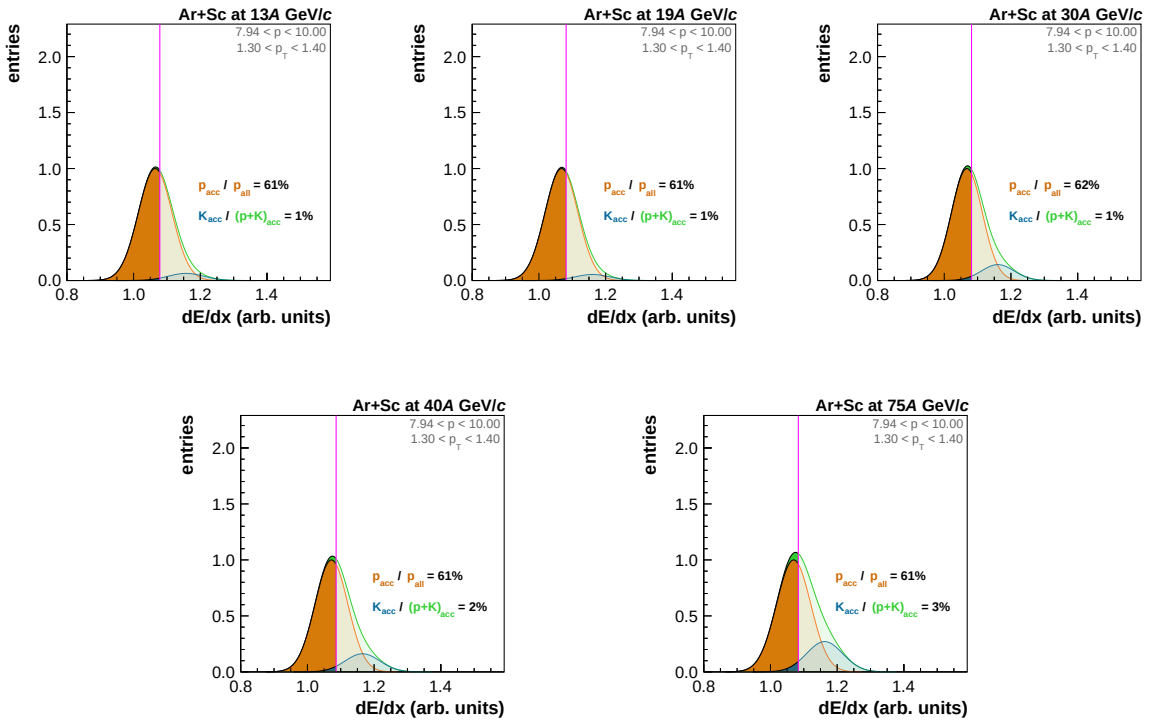

Figure 5.15 Example of Gaussian fits in one of the analyzed p–p_T bins (normalized to proton peak) for ^{40}Ar + ^{45}Sc collisions at 13A–75A GeV/c. The graphical cut to select proton candidates is marked with a magenta line.

5.2.8 Rapidity selection

As the analysis concerns mid-rapidity protons [141], only proton candidates with center-of-mass rapidity (see Appendix. A.5) assuming proton mass, y_p, greater than 0 and less than 0.75 were selected. Distributions of y_p versus transverse-momenta, p_T (see Appendix A.2) for ^{208}Pb + ^{208}Pb collisions at 13A GeV/c and 30A GeV/c are shown in Fig. 5.16, and for ^{40}Ar + ^{45}Sc collisions at 13A–75A GeV/c are shown in Fig. 5.17. The dotted red vertical lines show the upper and lower limits of the mid-rapidity proton selection.

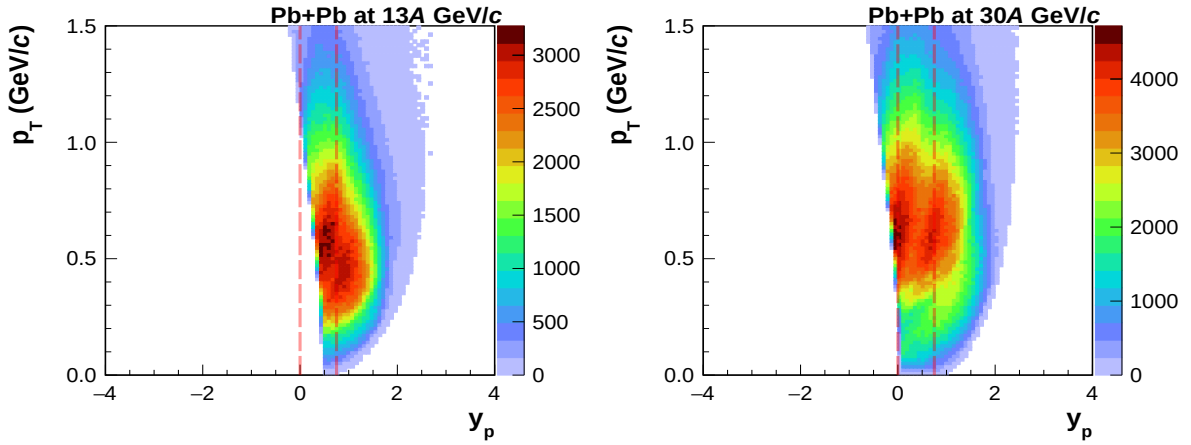

Figure 5.16 Distributions of y_p versus p_T for ^{208}Pb + ^{208}Pb collisions at 13A GeV/c (*left*) and 30A GeV/c (*right*), see text for details.

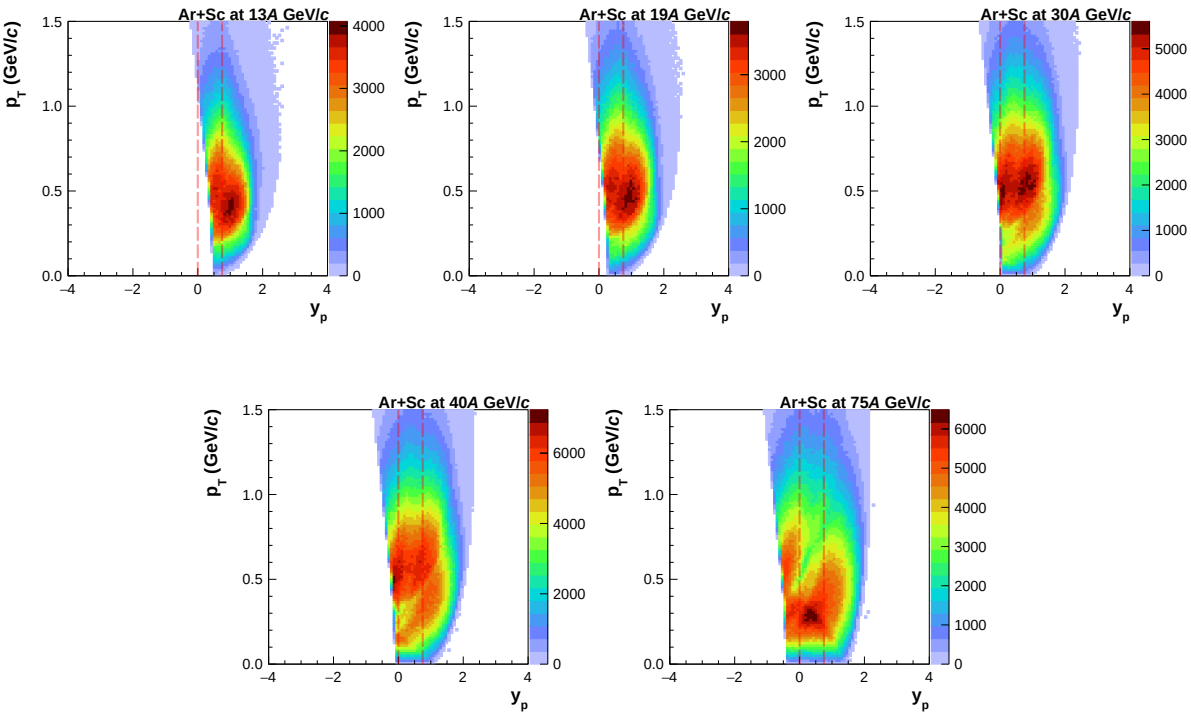

Figure 5.17 Distributions of y_p versus p_T for ^{40}Ar + ^{45}Sc collisions at 13A–75A GeV/c, see text for details.

5.3 Single-particle acceptance maps

A three-dimensional (y_p, p_x and p_y) acceptance map [142] was created to describe the momentum region selected for the analysis. The map was created by comparing the number of Monte Carlo-generated mid-rapidity protons before and after detector simulation and reconstruction. Only bins from the regions with at least 70% reconstructed particles are included in the acceptance map. An example map for proton intermittency analysis of ^{40}Ar + ^{45}Sc collisions at 75*A* GeV/*c* is shown in Fig. 5.18. Single-particle acceptance maps used for proton intermittency analysis for other analyzed ^{208}Pb + ^{208}Pb and ^{40}Ar + ^{45}Sc data sets are given in Ref. [135]. These maps are also used to calculate model predictions(see Chapter 7), and they are given in Ref. [142].

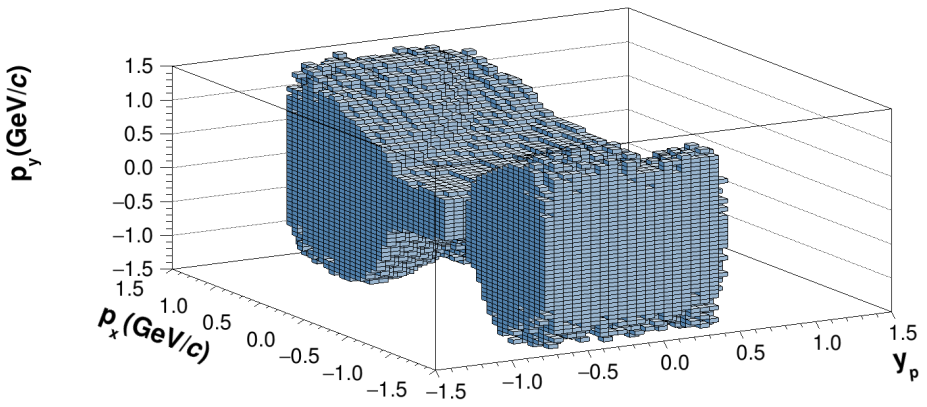

Figure 5.18 Example of single-particle acceptance map for ^{40}Ar + ^{45}Sc collisions at 75*A* GeV/*c* used for proton intermittency analysis, see text for details.

5.4 Two-particle acceptance map

The momentum-based Two Track Distance (mTTD) cut was introduced in Sec. 3.4 with the help of the new momentum coordinate system (see Eqs. 3.7). The mTTD cut defines the biased region where we don't have good efficiency for measuring two tracks and removes the remaining split tracks from the data after the potential point ratio cut. For each pair of selected proton candidates in both recorded and mixed events (see Sec. 3.1.1) for ^{208}Pb + ^{208}Pb collisions at

13*A* and 30*A* GeV/*c* and ^{40}Ar + ^{45}Sc collisions at 13*A*–75*A* GeV/*c*, the geometrical Two-Track Distance (gTTD) was calculated.

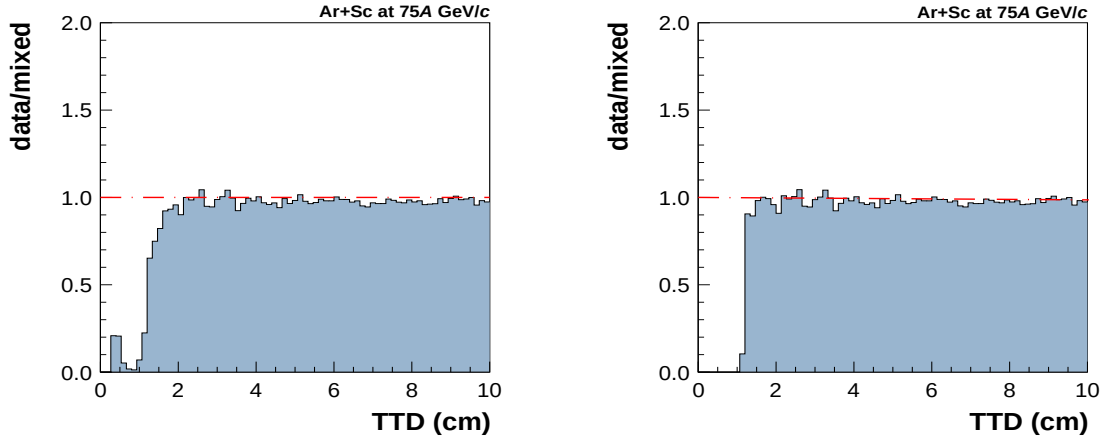

Figure 5.19 Example distributions of the TTD ratio of the experimental to mixed data before (*left*) and after (*right*) the mTTD cut for ^{40}Ar + ^{45}Sc collisions at 75*A* GeV/*c*.

It is the average distance of their tracks in x-y plane at eight different z planes (-506, -255, -201, -171, -125, 125, 352, and 742 cm). The TPC's limitation to recognizing close tracks is clearly visible in Fig 5.19 (*left*) for gTTD less than 2.2 cm for ^{40}Ar + ^{45}Sc collisions at 75*A* GeV/*c*. The gTTD cut values for each data set are listed in Table 5.6.

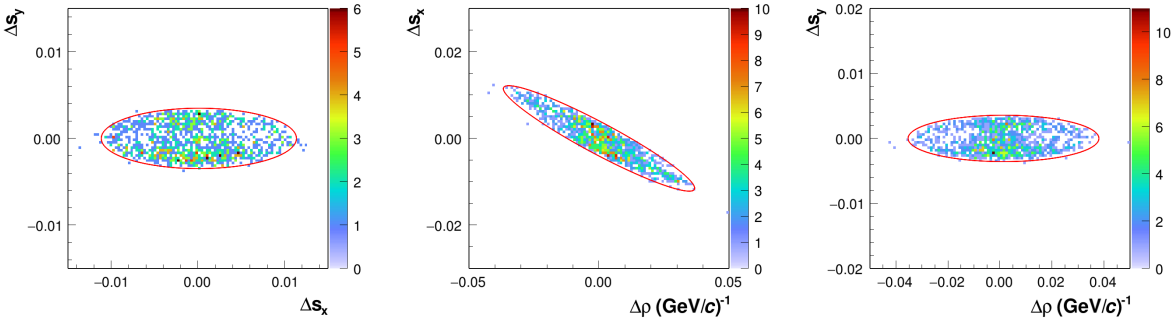

Figure 5.20 Example distributions of the rejected protons by the gTTD cut for ^{40}Ar + ^{45}Sc collisions at 75*A* GeV/*c*. Ellipses (see Eqs. 3.9) are drawn by a red color as a reference to tune the mTTD cut parameters (see Table 5.6).

Example distributions of the rejected protons by the gTTD cut for ^{40}Ar + ^{45}Sc collisions at

75*A* GeV/*c* are shown in Fig. 5.20. The ellipses were drawn by the red color used as a reference to tune the mTTD cut parameters. Proton pairs with momenta inside all the parameterized ellipses (see Eqs. 3.9) are rejected. The mTTD cut parameters, and the number of rejected protons by the mTTD cut for ^{208}Pb + ^{208}Pb and ^{40}Ar + ^{45}Sc data sets are summarized in Table 5.6.

Table 5.6 Numerical values of the mTTD cut parameters of the parameterized ellipses (see Eqs. 3.9) were used to analyze ^{40}Ar + ^{45}Sc collisions at 13*A*–75*A* GeV/*c*. Particle pairs with momenta inside all the ellipses are rejected.

p_{beam} (GeV/*c*)	gTTD cut (cm)	r_ρ	r_{s_y}	r_{s_x}	$r_{\rho s_x}$	$r_{s_x \rho}$	θ	# mTTD rejected tracks
^{208}Pb + ^{208}Pb								
13A	5	0.089	0.009	0.009	0.089	0.009	6	1258
30A	6	0.102	0.009	0.022	0.102	0.002	13	1694
^{40}Ar + ^{45}Sc								
13A	3.5	0.470	0.004	0.047	0.470	0.004	5	307
19A	2.8	0.121	0.003	0.010	0.121	0.003	8	371
30A	2.8	0.123	0.002	0.013	0.123	0.002	13	349
40A	2.2	0.043	0.002	0.010	0.043	0.002	15	306
75A	2.2	0.080	0.002	0.011	0.020	0.002	31	559

The two-particle acceptance used for proton intermittency analysis of ^{40}Ar + ^{45}Sc collisions at 75*A* GeV/*c* data analysis is shown in Fig. 5.19 (*right*) and for other analyzed ^{208}Pb + ^{208}Pb and ^{40}Ar + ^{45}Sc data sets are given in Ref. [135].

Due to its momentum-based definition, the mTTD cut can be used when comparing models with experimental results. The mTTD cut is used both for the data analysis (see Sec 6) and for calculating the model predictions (see Sec. 7).

Chapter Six

Intermittency analysis results

This Chapter presents results on second-order scaled factorial moments, $F_2(M)$ (see Eq. 2.1) of selected proton candidates (see Sec. 5.2.7) produced within the analysis acceptances (see Sec. 5.3) by strong and electromagnetic interactions in 0–10% *central* ^{208}Pb + ^{208}Pb collisions at 13*A*, and 30*A* GeV/*c* and ^{40}Ar + ^{45}Sc collisions at 13*A*, 19*A*, 30*A*, 40*A*, and 75*A* GeV/*c*. The results are shown as a function of the number of subdivisions (M^2) in transverse-momentum space — the so-called intermittency analysis (see Chapter 2). The analysis was performed for cumulative (see Sec. 3.1.2) and original (or non-cumulative) transverse-momentum components. Independent data sets were used to calculate results for each subdivision (see Sec. 3.2). Statistical uncertainties were calculated using statistical uncertainty propagation, Eq. 3.6 (see Sec. 3.3). The dependence of $F_2(M)$ on M^2 was obtained for the maximum subdivision number of M = 150 and M = 32. The latter, the coarse subdivision, was introduced to limit the effect of experimental momentum resolution [107].

Results for subdivisions in non-cumulative transverse-momentum space are shown in Sec. 6.3, and for subdivisions in cumulative transverse-momentum space are shown in Sec. 6.4. The final results were not corrected for possible biases. Their magnitude was estimated (see Chapter 7) by comparing results for pure Epos1.99 [143] and Epos1.99 subjected to the detector response simulation (see Sec. 4.3.2), reconstruction (see Sec. 4.3.1), and data-like analysis (see Chapter 5).

6.1 Proton pairs in each bin

Example distributions of proton pairs summed over all p_x–p_y bins and events, N_2 (see Eq. 3.1) within the analysis acceptance and after applying the mTTD cut for 0–10% *central* ^{40}Ar + ^{45}Sc collisions at 75*A* GeV/*c* for each *M* shown in Fig. 6.1. The sub-division number, *M* (for $1 \leq M \leq 32$), is indicated in plots. The distributions for all data sets (for $1 \leq M \leq 32$ and $1 \leq M \leq 150$) are documented in Ref. [135]. As expected $\langle N_2 \rangle$ decrease with increasing *M* for ^{40}Ar + ^{45}Sc collisions at 75*A* GeV/*c* from *M* = 1 to *M* = 32.

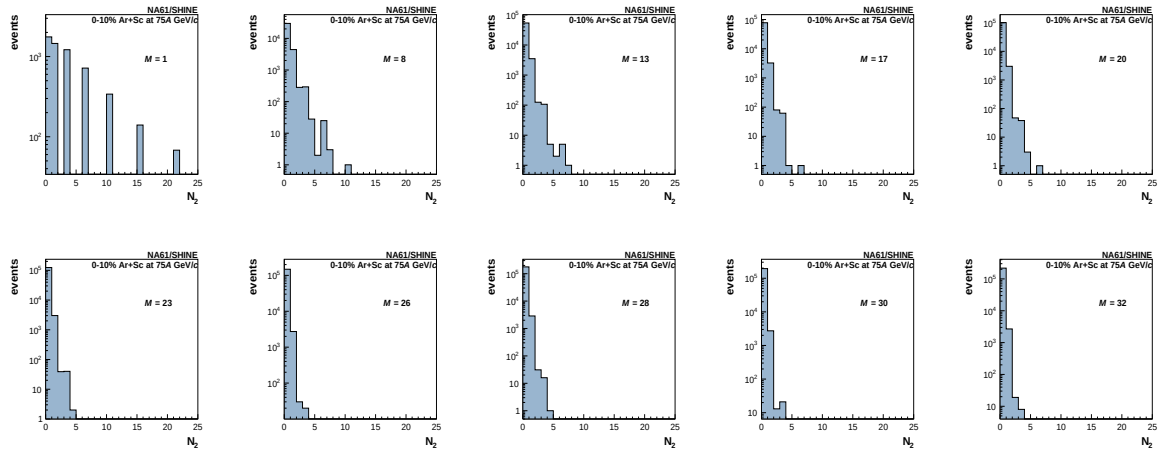

Figure 6.1 Example proton pair distributions in each bin ($1 \leq M \leq 32$) for ^{40}Ar + ^{45}Sc collisions at 75*A* GeV/*c*. The sub-division number, *M*, is indicated in plots.

6.2 Two-particle correlation function

The two-particle correlation function, Δp_T (see Appendix A.3) of selected proton candidates within the analysis acceptance for ^{208}Pb + ^{208}Pb collisions at 13*A* and 30*A* GeV/*c*, and ^{40}Ar + ^{45}Sc collisions at 13*A*–75*A* GeV/*c* are shown in Figs. 6.2 and 6.3. The correlation function is defined as the ratio of normalized Δp_T distributions for data and mixed events. The data distribution includes the mTTD cut, whereas the mixed one does not. The decrease of the correlation function at $\Delta p_T \approx 0$ is due to anti-correlation generated by the mTTD cut.

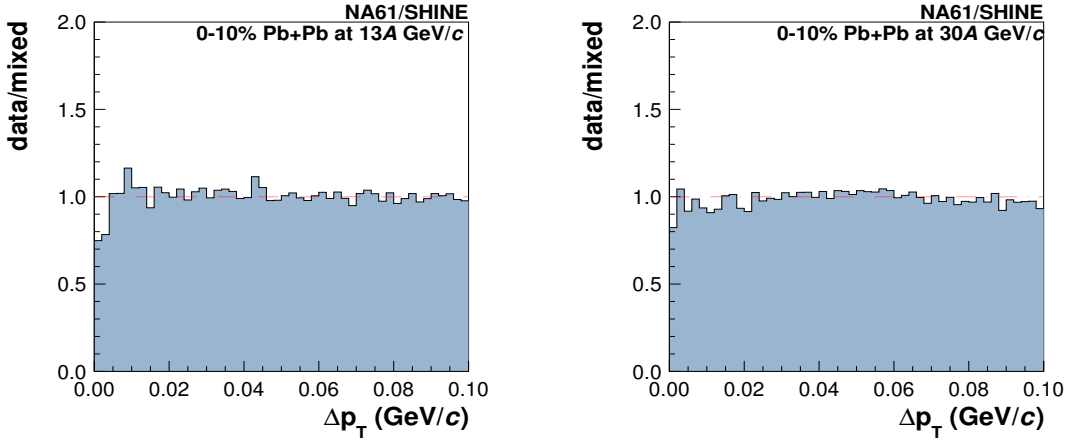

Figure 6.2 Examples two-particle correlation function in Δp_T for selected proton candidates within analysis acceptance for ^{208}Pb + ^{208}Pb collisions at 13*A* *left* and 30*A* GeV/*c* (*right*). The data distribution includes the mTTD cut, whereas the mixed one does not.

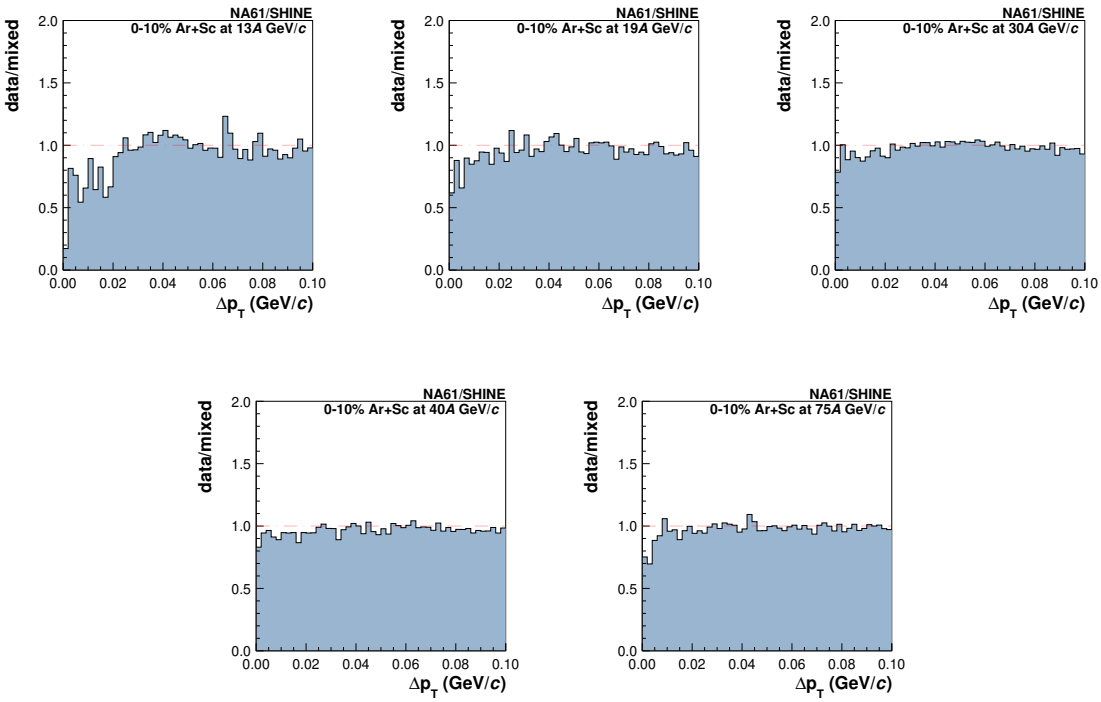

Figure 6.3 Examples two-particle correlation function in Δp_T for proton candidates within analysis acceptance for ^{40}Ar + ^{45}Sc collisions at 13*A*–75*A* GeV/*c*. The data distribution includes the mTTD cut, whereas the mixed one does not.

6.3 Results for subdivisions in non-cumulative transverse-momentum space

The results on $F_2(M)$ and $\Delta F_2(M)$ (see Eq. 3.2) for subdivisions in non-cumulative transverse-momentum space are shown in Figs. 6.4 - 6.10. The results shown in Figs. 6.4 and 6.8 correspond to fine binning (*M* up to 150), whereas the results shown in Figs. 6.6 and 6.10 correspond to coarse binning (*M* up to 32). The mTTD cut for both data and mixed events. The values of the cut parameters are given in Table 5.6.

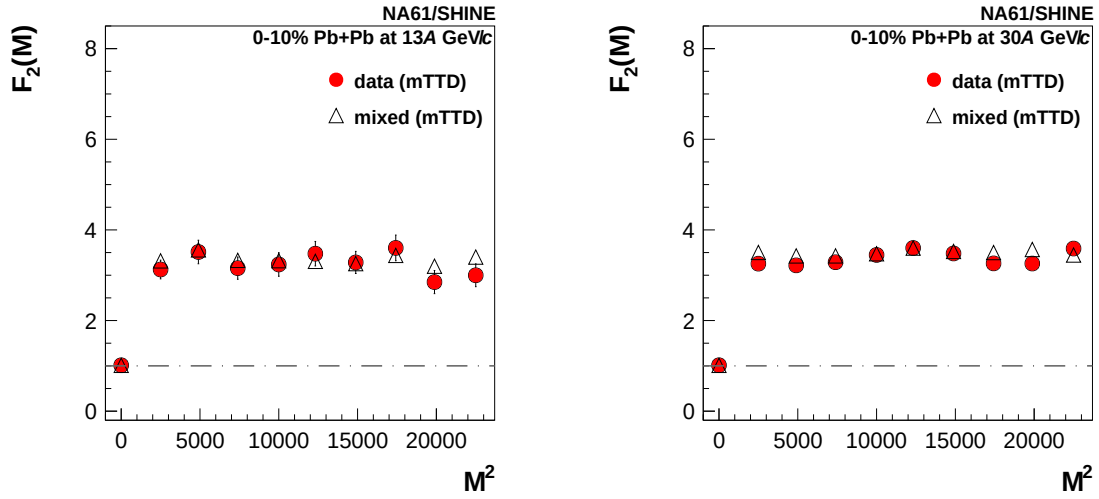

Figure 6.4 Results on the dependence of the scaled-factorial moment of proton multiplicity distribution on the number of subdivisions in transverse-momentum space M^2 for $1 \leq M \leq 150$. Results for 0–10% *central* ^{208}Pb + ^{208}Pb collisions at 13*A* (*left*) and 30*A* GeV/*c* (*right*). Closed red circles indicate the experimental data. Corresponding results for mixed events (open triangles) are also shown. Both the data and mixed events include the mTTD cut. Only statistical uncertainties are indicated.

The red closed circles indicate the experimental data. For comparison, corresponding results for mixed events (see Sec. 3.1.1) are shown by the grey triangles. Note that by construction, the multiplicity distribution of protons in mixed events for $M = 1$ equals the corresponding distribution for the data. In mixed events, the only correlation of particles in the transverse-momentum space is due to the mTTD cut. Both the data and mixed events include the mTTD cut. Only statistical uncertainties are indicated. The horizontal dotted line represents the reference line at $F_2(1)$.

By construction, $F_2(1)$ values are equal for subdivisions in cumulative transverse-momentum space and non-cumulative transverse-momentum space. But for the latter, $F_2(M)$ strongly depends on M^2. This dependence is primarily due to the non-uniform shape of the single-particle transverse-momentum distributions (see Sec. 3.1.2). It can be accounted for by comparing the experimental data results with those obtained for the mixed events (see Sec. 3.1.1) using $\Delta F_2(M) \approx F_2^{data}(M) - F_2^{mixed}(M)$ [110]. The dependence of $\Delta F_2(M)$ on the number of sub-divisions shown in Figs. 6.5, 6.9 and 6.7, 6.11 for fine and coarse binning.

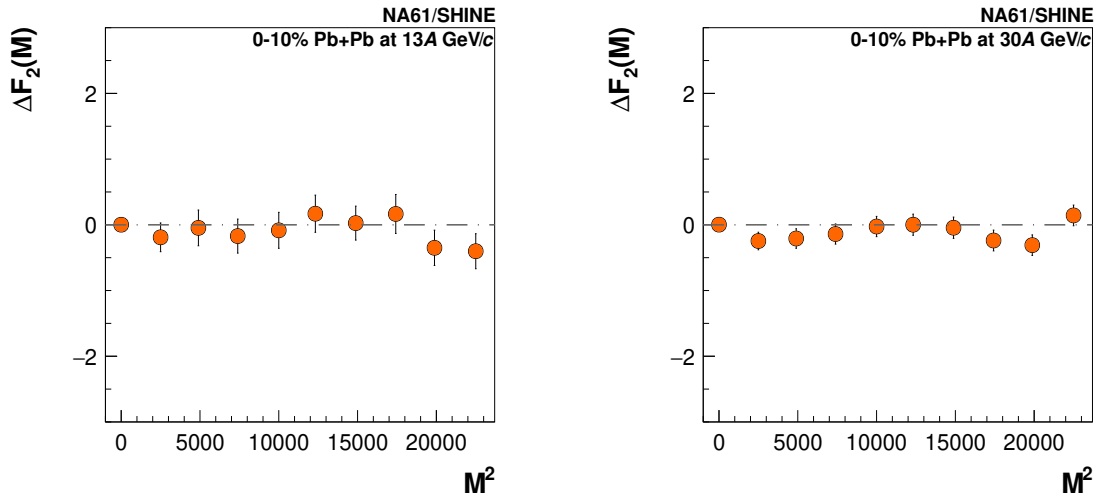

Figure 6.5 Results on the dependence of $\Delta F_2(M) \approx F_2^{data}(M) - F_2^{mixed}(M)$ of proton multiplicity distribution on the number of subdivisions in transverse-momentum space M^2 for $1 \leq M \leq 150$. Results for 0–10% *central* ^{208}Pb + ^{208}Pb collisions at 13*A* (*left*) and 30*A* GeV/*c* (*right*). Both the data and mixed events include the mTTD cut. Only statistical uncertainties are indicated.

The experimental results presented in Figs. 6.4 - 6.11 do not show any significant difference to the results for mixed events with the mTTD cut on M^2 ($\Delta F_2(M) \approx 0$). There is no indication of the critical fluctuations for selected protons. The numerical values of proton intermittency in transverse-momentum space for 0–10% *central* ^{208}Pb + ^{208}Pb collisions at 13*A* and 30*A* GeV/*c* and ^{40}Ar + ^{45}Sc collisions at 13*A*–75*A* GeV/*c* are presented in Tables 6.1 and 6.2.

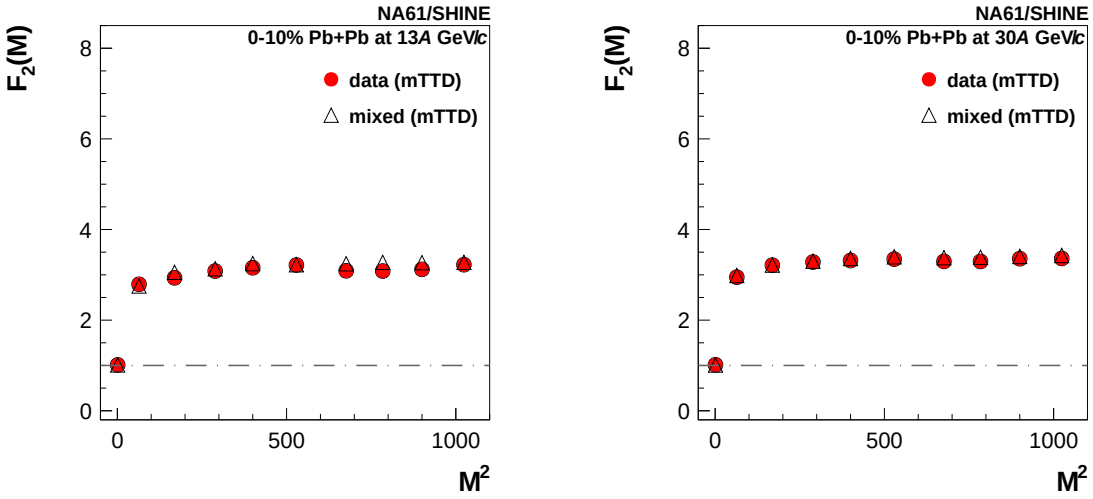

Figure 6.6 Results on the dependence of the scaled-factorial moment of proton multiplicity distribution on the number of subdivisions in transverse-momentum space M^2 for $1 \leq M \leq 32$. Results for 0–10% *centrality* selection of events are presented for ^{208}Pb + ^{208}Pb interaction at 13*A* (*left*) and 30*A* GeV/*c* (*right*). Closed red circles indicate the experimental data. Corresponding results for mixed events (open triangles) are also shown. Both the data and mixed events include the mTTD cut. Only statistical uncertainties are indicated.

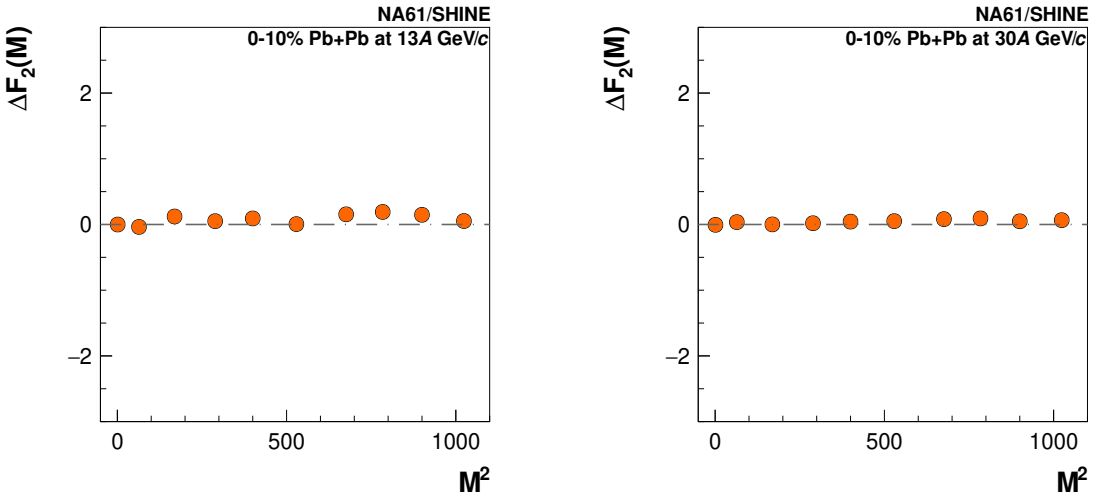

Figure 6.7 Results on the dependence of $\Delta F_2(M) \approx F_2^{data}(M) - F_2^{mixed}(M)$ of proton multiplicity distribution on the number of subdivisions in transverse-momentum space M^2 for $1 \leq M \leq 32$. Results for 0–10% *central* ^{208}Pb + ^{208}Pb collisions at 13*A* (*left*) and 30*A* GeV/*c* (*right*). Both the data and mixed events include the mTTD cut. Only statistical uncertainties are indicated.

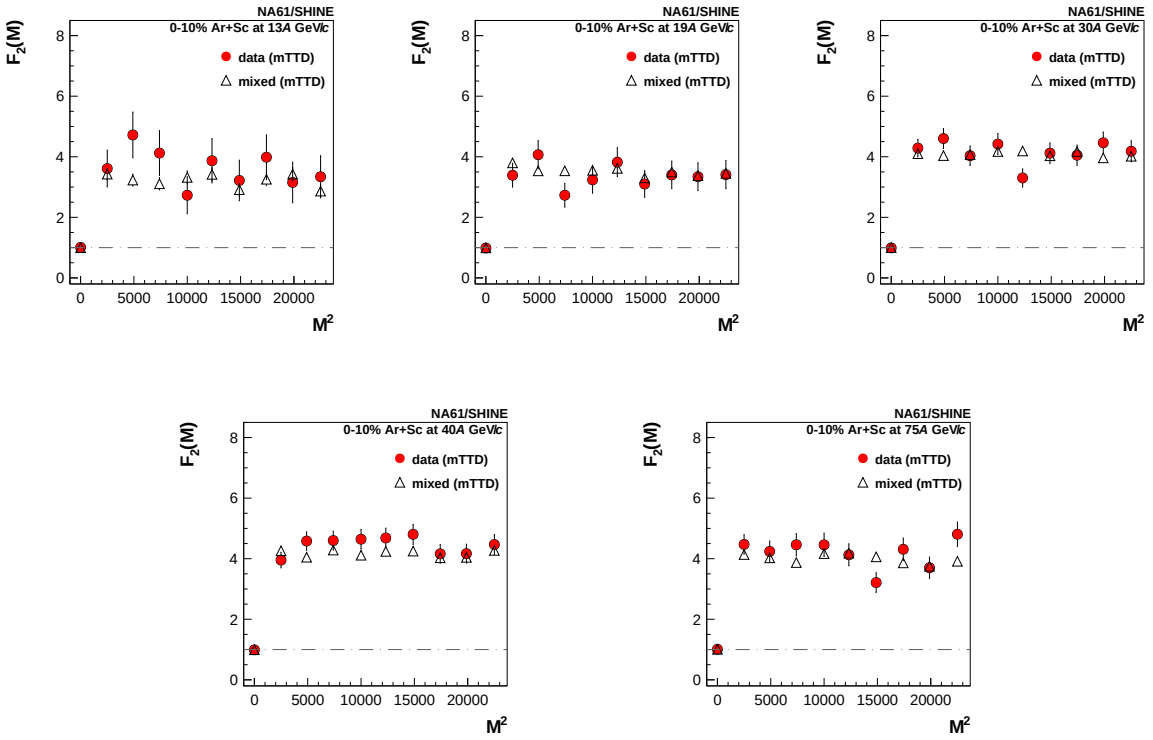

Figure 6.8 Results on the dependence of the scaled-factorial moment of proton multiplicity distribution on the number of subdivisions in transverse-momentum space M^2 for $1 \leq M \leq 150$. Results for 0–10% *central* ^{40}Ar + ^{45}Sc collisions at 13*A*–75*A* GeV/*c*. Closed red circles indicate the experimental data. Corresponding results for mixed events (open triangles) are also shown. Both the data and mixed events include the mTTD cut. Only statistical uncertainties are indicated.

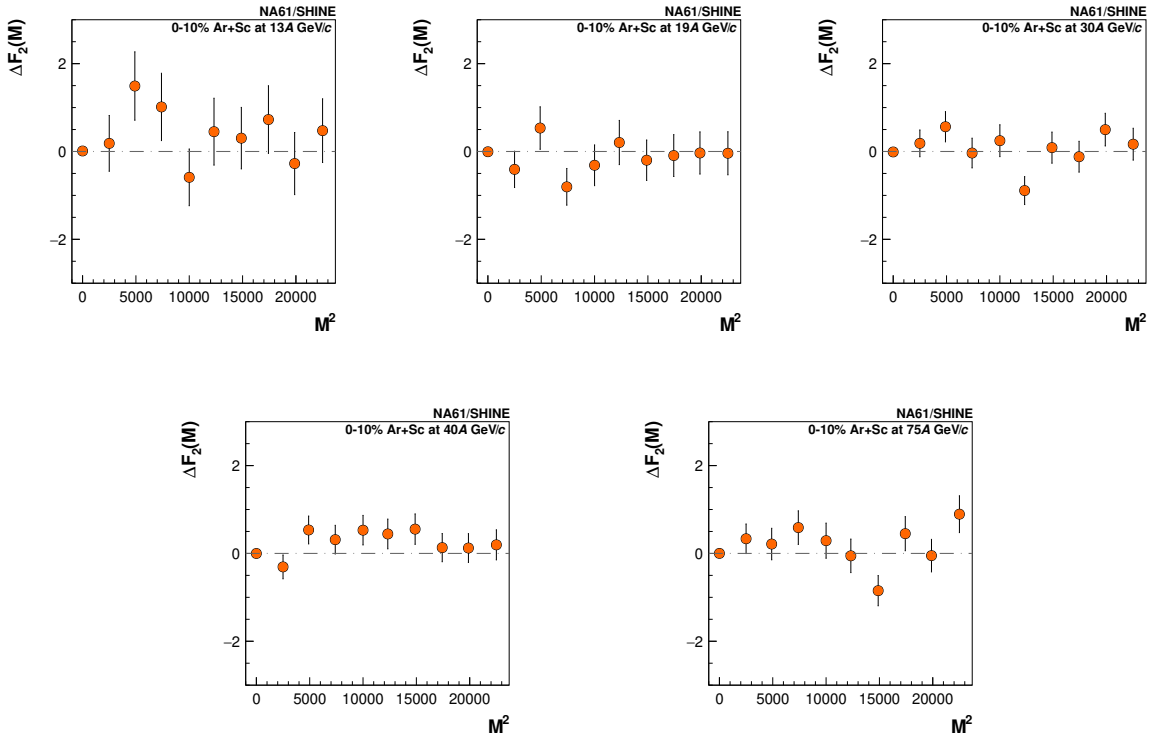

Figure 6.9 Results on the dependence of $\Delta F_2(M) \approx F_2^{data}(M) - F_2^{mixed}(M)$ of proton multiplicity distribution on the number of subdivisions in transverse-momentum space M^2 for $1 \leq M \leq 150$. Results for 0–10% *central* ^{40}Ar + ^{45}Sc collisions at 13*A*–75*A* GeV/*c*. Both the data and mixed events include the mTTD cut. Only statistical uncertainties are indicated.

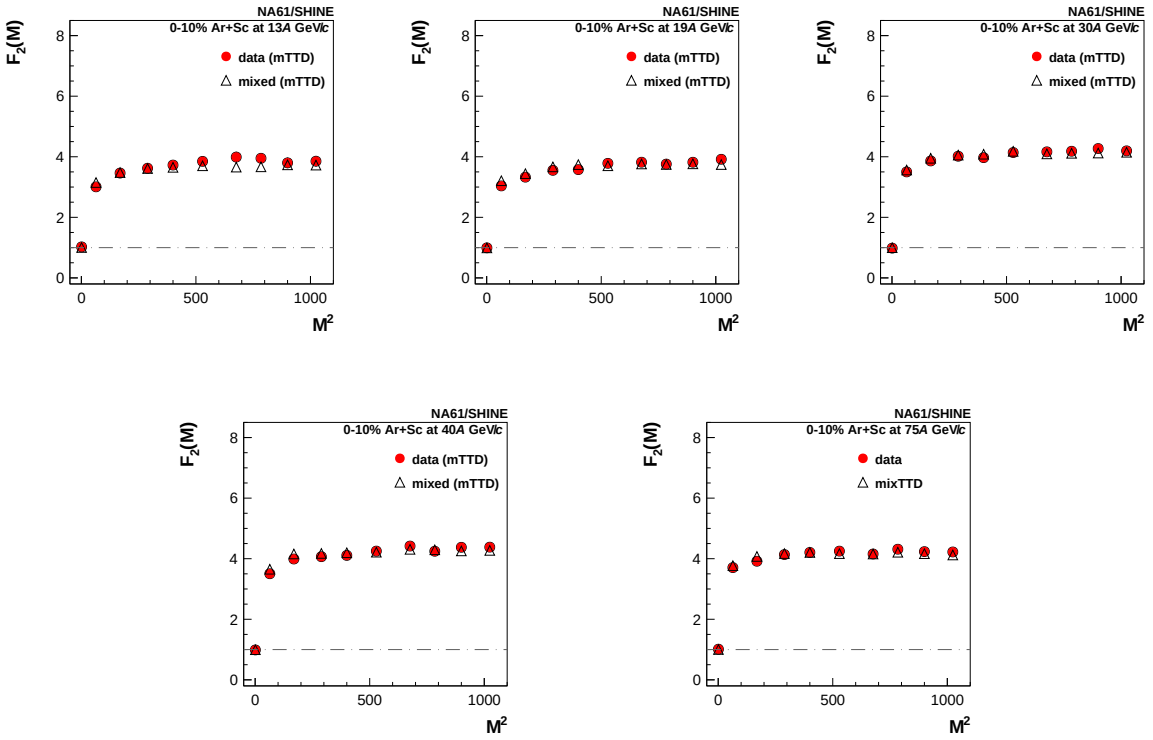

Figure 6.10 Results on the dependence of the scaled-factorial moment of proton multiplicity distribution on the number of subdivisions in transverse-momentum space M^2 for $1 \leq M \leq 32$. Results for 0–10% *central* ^{40}Ar + ^{45}Sc collisions at 13*A*–75*A* GeV/*c*. Closed red circles indicate the experimental data. Corresponding results for mixed events (open triangles) are also shown. Both the data and mixed events include the mTTD cut. Only statistical uncertainties are indicated.

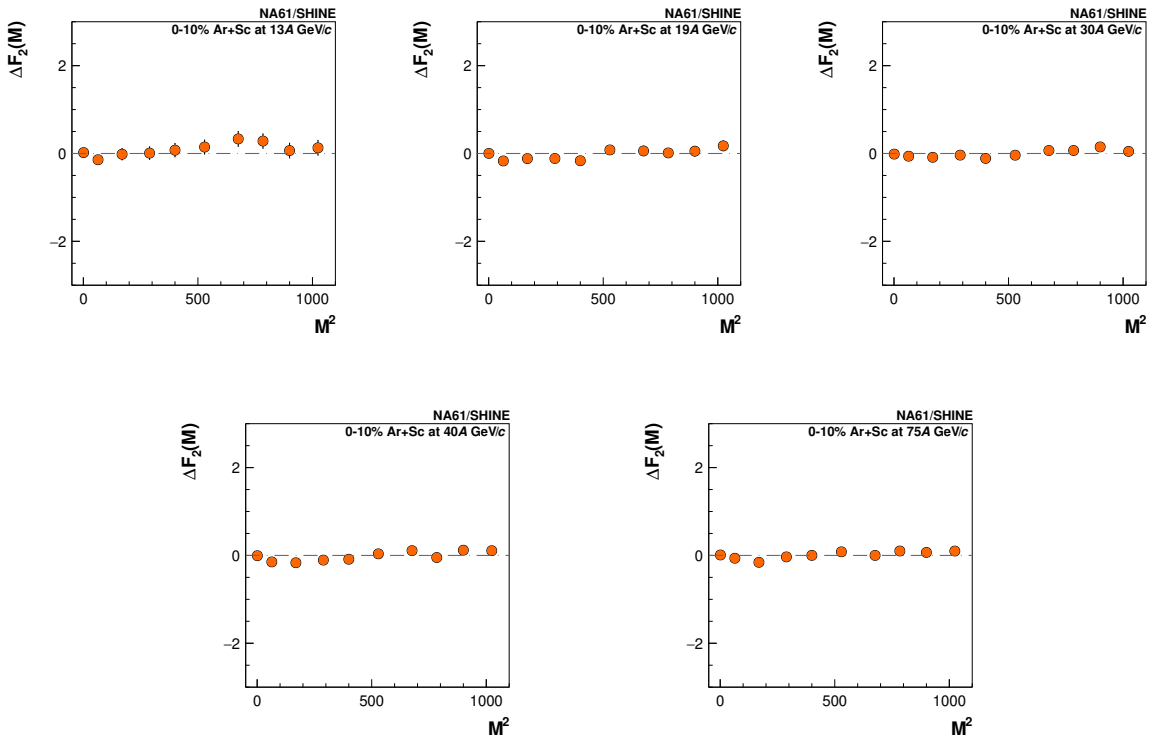

Figure 6.11 Results on the dependence of $\Delta F_2(M) \approx F_2^{data}(M) - F_2^{mixed}(M)$ of proton multiplicity distribution on the number of subdivisions in transverse-momentum space M^2 for $1 \leq M \leq 32$. Results for 0–10% *central* ^{40}Ar + ^{45}Sc collisions at 13*A*–75*A* GeV/*c*. Both the data and mixed events include the mTTD cut. Only statistical uncertainties are indicated.

6.4 Results for subdivisions in cumulative transverse-momentum space

Figures 6.12, 6.14 and 6.13, 6.15 present the dependence of $F_2(M)$ on M^2 in cumulative transverse-momentum space for the maximum subdivision number of M = 150 and M = 32. The experimental results are shown for 0–10% *central* ^{208}Pb + ^{208}Pb collisions at 13*A*, and 30*A* GeV/*c* and ^{40}Ar + ^{45}Sc collisions at 13*A*–75*A* GeV/*c*. As a reference, the corresponding results for mixed events are also shown. For the mixed events, the second scaled-factorial moment is independent of M^2, $F_2(M) = F_2(1)$. The numerical values of proton intermittency in cumulative transverse-momentum space for *central* ^{208}Pb + ^{208}Pb collisions at 13*A* and 30*A* GeV/*c* and ^{40}Ar + ^{45}Sc collisions at 13*A*–75*A* GeV/*c* are presented in Tables 6.3 and 6.4. The results for subdivisions in cumulative transverse-momentum space, $F_2(M)$ for $M > 1$, are systematically below $F_2(M = 1)$. It is probably due to the anti-correlation generated by the mTTD cut to the data. The effect of the mTTD cut on the results for mixed events is shown in Fig. 3.8 (see Chapter 3). Based on the findings, it is evident that when M^2 is greater than one, the values of $F_2(M)$ are systematically below $F_2(M = 1)$ in cumulative transverse-momentum space when the mTTD or gTTD cut is applied to the mixed events. Note that the mTTD cut is necessary to properly account for the detector losses of close-in-space tracks (see Sec. 3.4).

The experimental results show only a slight decrease of $F_2(M)$ with M^2. There is no indication of the critical fluctuations for selected proton candidates.

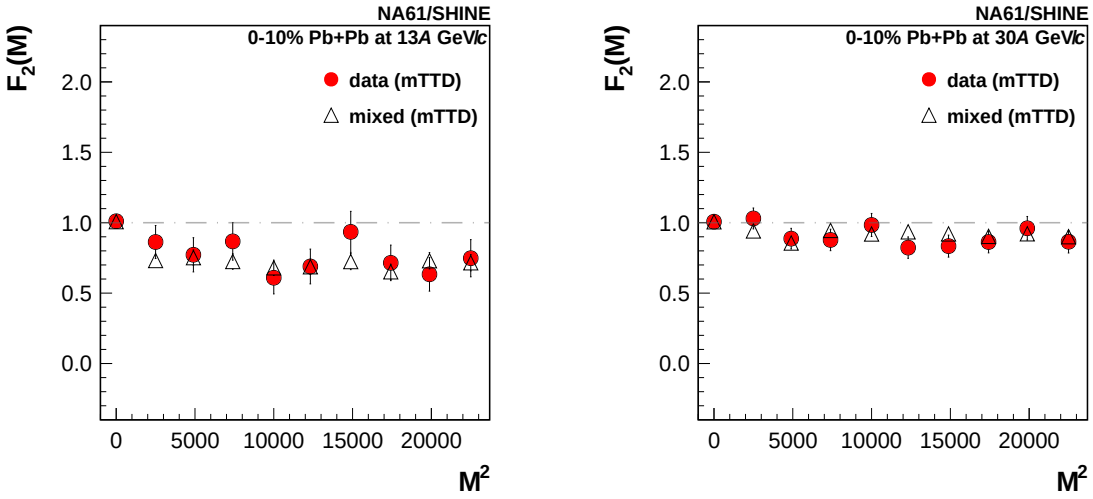

Figure 6.12 Results on the dependence of the scaled-factorial moment of proton multiplicity distribution on the number of subdivisions in cumulative transverse-momentum space M^2 for $1 \leq M \leq 150$. Results for 0–10% *central* ^{208}Pb + ^{208}Pb collisions at 13*A* (*left*) and 30*A* GeV/*c* (*right*). Closed red circles indicate the experimental data. Corresponding results for mixed events (open triangles) are also shown. Both the data and mixed events include the mTTD cut. Only statistical uncertainties are indicated.

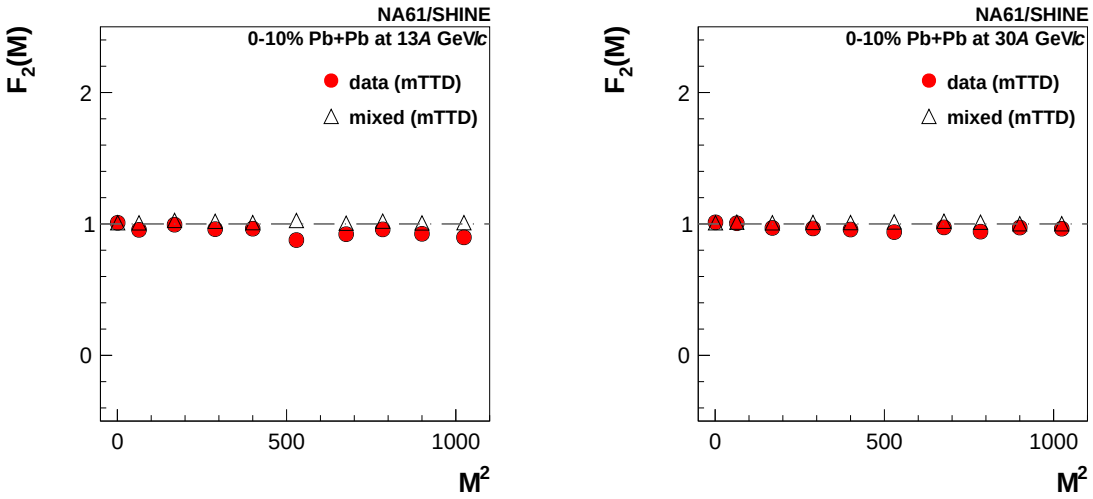

Figure 6.13 Results on the dependence of the scaled-factorial moment of proton multiplicity distribution on the number of subdivisions in cumulative transverse-momentum space M^2 for $1 \leq M \leq 32$. Results for 0–10% *central* ^{208}Pb + ^{208}Pb collisions at 13*A* (*left*) and 30*A* GeV/*c* (*right*). Closed red circles indicate the experimental data. Corresponding results for mixed events (open triangles) are also shown. Both the data and mixed events include the mTTD cut. Only statistical uncertainties are indicated.

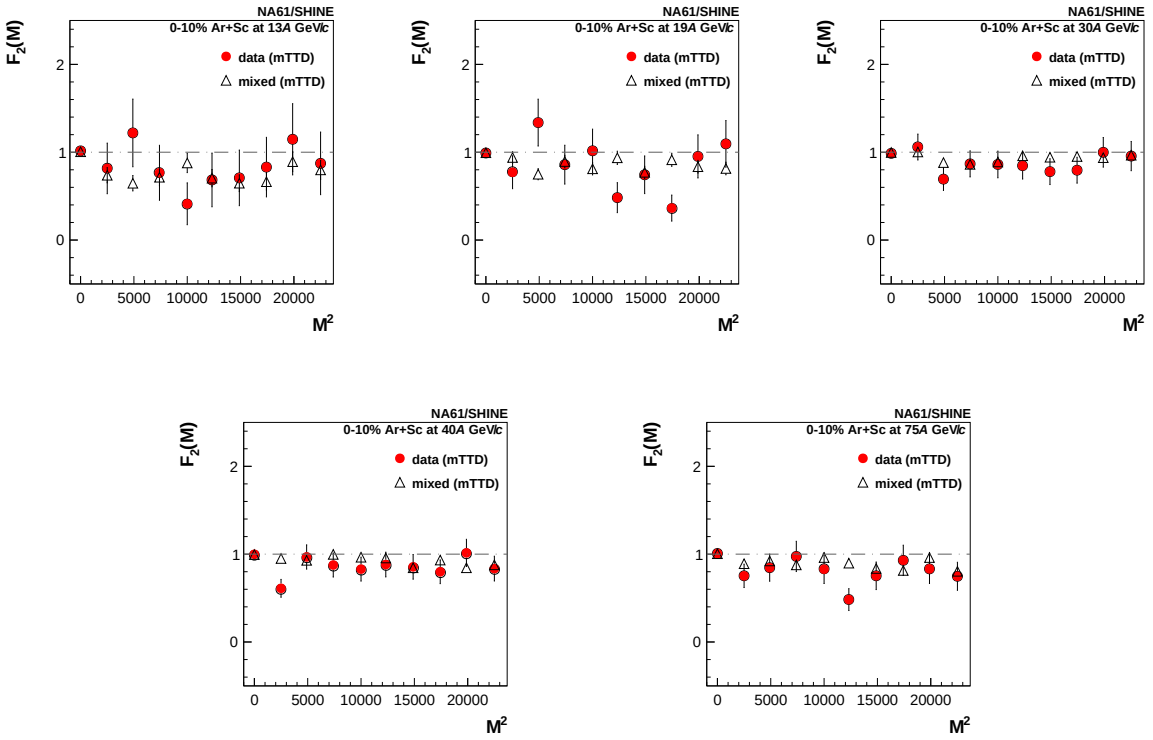

Figure 6.14 Results on the dependence of the scaled-factorial moment of proton multiplicity distribution on the number of subdivisions in cumulative transverse-momentum space M^2 for $1 \leq M \leq 150$. Results for 0–10% *central* ^{40}Ar + ^{45}Sc collisions at 13*A*–75*A* GeV/*c*. Closed red circles indicate the experimental data. Corresponding results for mixed events (open triangles) are also shown. Both the data and mixed events include the mTTD cut. Only statistical uncertainties are indicated.

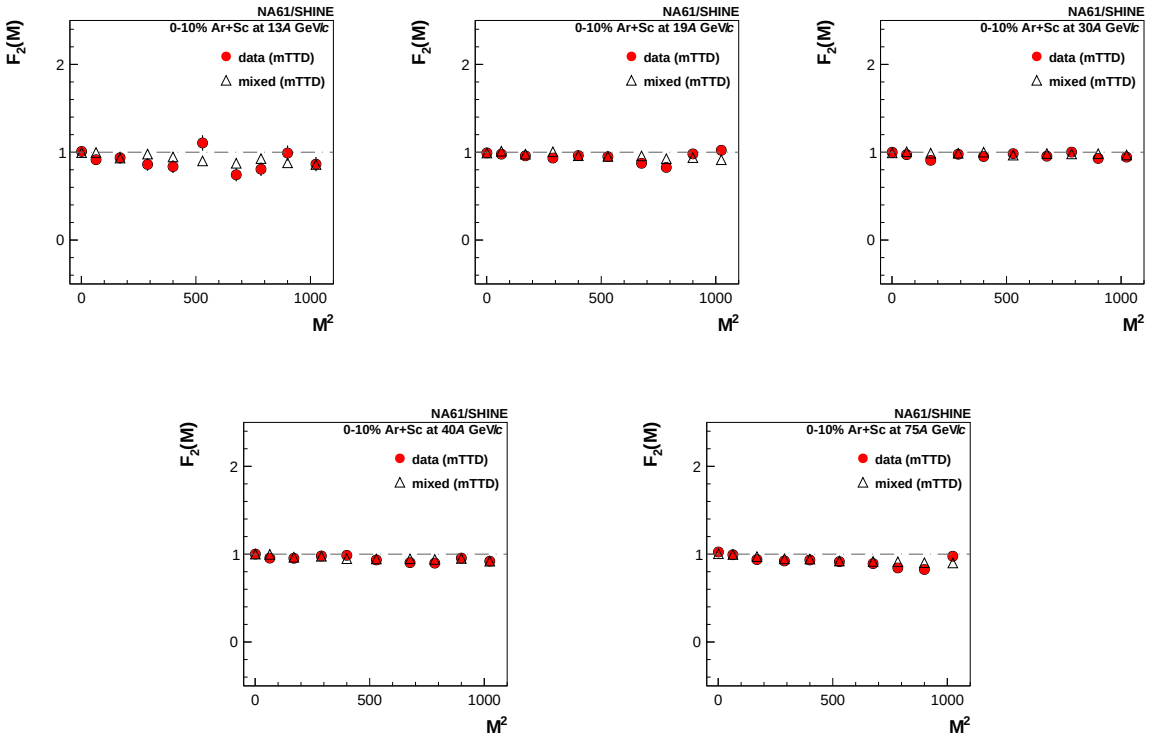

Figure 6.15 Results on the dependence of the scaled-factorial moment of proton multiplicity distribution on the number of subdivisions in cumulative transverse-momentum space M^2 for $1 \leq M \leq 32$. Results for 0–10% *central* ^{40}Ar + ^{45}Sc collisions at 13*A*–75*A* GeV/*c*. Closed red circles indicate the experimental data. Corresponding results for mixed events (open triangles) are also shown. Both the data and mixed events include the mTTD cut. Only statistical uncertainties are indicated.

Table 6.1 Numerical values of the results for 0–10% *central* ^{208}Pb + ^{208}Pb collisions at 13*A* GeV/*c* and 30*A* GeV/*c* presented in Figs. 6.4 and 6.6 are tabulated. The subdivisions are in non-cumulative transverse-momentum space. The *left* table corresponds to fine binning, $1 \leq M \leq 150$, and the right table corresponds to coarse binning, $1 \leq M \leq 32$. The statistical uncertainties, σ_{F_2} are also given.

non-cumulative and fine binning					non-cumulative and coarse binning				
	13*A* GeV/*c*		30*A* GeV/*c*			13*A* GeV/*c*		30*A* GeV/*c*	
M	$F_2(M)$	σ_{F_2}	$F_2(M)$	σ_{F_2}	*M*	$F_2(M)$	σ_{F_2}	$F_2(M)$	σ_{F_2}
1	1.0127	0.0069	1.0133	0.0041	1	1.0118	0.0068	1.0145	0.0046
50	2.5263	0.2062	3.2553	0.1267	8	2.7906	0.0380	2.9483	0.02409
70	3.5126	0.2595	3.2176	0.1414	13	2.9334	0.0459	3.2134	0.02831
86	2.9856	0.2601	3.2864	0.1461	17	3.0828	0.0509	3.2818	0.03034
100	3.2372	0.2455	3.1474	0.1463	20	3.1554	0.0529	3.3159	0.0312
111	3.4750	0.2701	3.3007	0.1530	23	3.2161	0.0553	3.3463	0.0323
122	2.7120	0.2440	3.3802	0.1540	26	3.0891	0.0571	3.2963	0.0332
132	3.6026	0.2834	3.2611	0.1502	28	3.0838	0.0555	3.2948	0.0330
141	2.8489	0.2551	3.0581	0.1479	30	3.1205	0.0577	3.3564	0.0335
150	2.7787	0.2515	2.9885	0.1492	32	3.2232	0.0586	3.3609	0.0342

Table 6.2 Numerical values of the results for 0–10% *central* ^{40}Ar + ^{45}Sc collisions at 13*A*–75*A* GeV/*c* presented in Figs. 6.8 and 6.10 are tabulated. The subdivisions are in non-cumulative transverse-momentum space. The *top* table corresponds to fine binning, $1 \leq M \leq 150$, and the *bottom* table corresponds to coarse binning, $1 \leq M \leq 32$. The statistical uncertainties, σ_{F_2} are also given.

	non-cumulative and fine binning									
	13*A* GeV/*c*		19*A* GeV/*c*		30*A* GeV/*c*		40*A* GeV/*c*		75*A* GeV/*c*	
M	$F_2(M)$	σ_{F_2}	$F_2(M)$	σ_{F_2}	$F_2(M)$	σ_{F_2}	$F_2(M)$	σ_{F_2}	$F_2(M)$	σ_{F_2}
1	1.0081	0.0162	0.9863	0.0102	0.9901	0.0065	0.9914	0.0063	1.0090	0.0082
50	3.6106	0.6074	3.3898	0.3917	4.2859	0.2912	3.9545	0.2582	4.4718	0.3221
70	4.7210	0.7543	4.0678	0.4649	4.6021	0.3295	4.5818	0.3047	4.2405	0.3427
86	4.1219	0.7393	2.7299	0.3934	4.0345	0.3232	4.5985	0.3119	4.4609	0.3671
100	2.7299	0.6100	3.2382	0.4402	4.4189	0.3474	4.6435	0.3229	4.4572	0.3840
111	3.8691	0.7306	3.8201	0.4807	3.3006	0.2997	4.6843	0.3250	4.1286	0.3644
122	3.2168	0.6703	3.1009	0.4382	4.1199	0.3393	4.8042	0.3327	3.2122	0.3242
132	3.9844	0.7394	3.4019	0.4542	4.0509	0.3348	4.1608	0.3064	4.3107	0.3720
141	3.1513	0.6715	3.3416	0.4586	4.4603	0.3567	4.1673	0.3130	3.7012	0.3527
150	3.3401	0.6962	3.4104	0.4681	4.1819	0.3469	4.4678	0.3273	4.8076	0.4031
	non-cumulative and coarse binning									
1	1.0241	0.0169	0.9924	0.0092	0.9823	0.0067	0.9877	0.0062	1.0119	0.0077
8	3.0068	0.0920	3.0378	0.0614	3.5003	0.0456	3.5035	0.0407	3.7058	0.0504
13	3.4613	0.1232	3.3261	0.0796	3.8625	0.0576	3.9894	0.0538	3.9157	0.0634
17	3.6205	0.1355	3.5516	0.0897	4.0170	0.0646	4.0664	0.0595	4.1359	0.0710
20	3.7256	0.1443	3.5753	0.0934	3.9707	0.0668	4.1082	0.0607	4.2068	0.0739
23	3.8482	0.1524	3.7829	0.1002	4.1394	0.0694	4.2511	0.0643	4.2496	0.0779
26	3.9897	0.1608	3.8198	0.1044	4.1624	0.0733	4.4173	0.0688	4.1551	0.0794
28	3.9498	0.1567	3.7577	0.1034	4.1818	0.0722	4.2456	0.0662	4.3129	0.0794
30	3.7991	0.1597	3.8186	0.1045	4.2715	0.0746	4.3761	0.0686	4.2335	0.0805
32	3.8528	0.1596	3.9164	0.1073	4.1952	0.0743	4.3811	0.0695	4.2220	0.0806

Table 6.3 Numerical values of the results presented in Figs. 6.12 and 6.13 are tabulated. The number of subdivisions in cumulative transverse-momentum space, *M*, for $1 \leq M \leq 150$ (fine binning) and $1 \leq M \leq 32$ (coarse binning). Results for 0–10% *central* ^{208}Pb + ^{208}Pb interaction at 13*A* and 30*A* GeV/*c*, the data points with an error for each *M* bin, are given here.

cumulative and fine binning					cumulative and coarse binning				
	13*A* GeV/*c*		30*A* GeV/*c*			13*A* GeV/*c*		30*A* GeV/*c*	
M	$F_2(M)$	σ_{F_2}	$F_2(M)$	σ_{F_2}	*M*	$F_2(M)$	σ_{F_2}	$F_2(M)$	σ_{F_2}
1	1.0116	0.0068	1.0089	0.0039	1	1.0084	0.0068	1.0119	0.0038
50	0.8629	0.1172	0.9287	0.0741	8	0.9550	0.0193	1.0050	0.0115
70	0.7721	0.1214	0.8273	0.0730	13	0.9941	0.0250	0.9696	0.0143
86	0.8674	0.1333	0.7435	0.0760	17	0.9604	0.0275	0.9659	0.0158
100	0.6091	0.1147	0.9633	0.0818	20	0.9637	0.0285	0.9574	0.0162
111	0.6890	0.1235	0.9484	0.0761	23	0.8772	0.0291	0.9380	0.0165
122	0.9348	0.1457	1.0630	0.0781	26	0.9220	0.0303	0.9413	0.01784
132	0.7148	0.1261	0.8927	0.0772	28	0.9585	0.0309	0.9737	0.0170
141	0.6327	0.1196	0.8165	0.0839	30	0.9248	0.0305	0.9724	0.0177
150	0.7479	0.1320	0.9525	0.0797	32	0.8979	0.0308	0.9637	0.0178

Table 6.4 Numerical values of the results for 0–10% *central* ^{40}Ar + ^{45}Sc collisions at 13*A*–75*A* GeV/*c* presented in Figs. 6.14 and 6.15 are tabulated. The subdivisions are in cumulative transverse-momentum space. The *top* table corresponds to fine binning, $1 \leq M \leq 150$, and the *bottom* table corresponds to coarse binning, $1 \leq M \leq 32$. The statistical uncertainties, σ_{F_2} are also given.

	cumulative and fine binning									
	13*A* GeV/*c*		19*A* GeV/*c*		30*A* GeV/*c*		40*A* GeV/*c*		75*A* GeV/*c*	
M	$F_2(M)$	σ_{F_2}	$F_2(M)$	σ_{F_2}	$F_2(M)$	σ_{F_2}	$F_2(M)$	σ_{F_2}	$F_2(M)$	σ_{F_2}
1	1.0154	0.0160	0.9909	0.0102	0.9868	0.0070	0.9984	0.0067	1.0078	0.0077
50	0.8156	0.2882	0.7718	0.1870	1.0588	0.1479	0.6108	0.1017	0.7529	0.1329
70	1.2198	0.3855	1.3373	0.2671	0.6935	0.1287	0.9677	0.1381	0.8461	0.1544
86	0.7659	0.3126	0.8582	0.2215	0.8672	0.1486	0.8760	0.1367	0.9742	0.1721
100	0.4129	0.2384	1.0163	0.2464	0.8606	0.1521	0.8293	0.1363	0.8284	0.1624
111	0.6845	0.3060	0.4828	0.1707	0.8463	0.1519	0.8816	0.1411	0.4828	0.1246
122	0.7079	0.3166	0.7433	0.2145	0.7789	0.1472	0.8553	0.1406	0.7538	0.1571
132	0.8303	0.3389	0.3639	0.1485	0.7951	0.1476	0.7994	0.1351	0.9295	0.1726
141	1.1472	0.4055	0.9522	0.2458	0.9987	0.1688	1.0143	0.1546	0.8325	0.1665
150	0.8732	0.3564	1.0950	0.2656	0.9560	0.1664	0.8354	0.1412	0.7479	0.1594
	cumulative and coarse binning									
1	1.0087	0.0158	0.9918	0.0097	0.9997	0.0070	1.0006	0.0067	1.0245	0.0084
8	0.9148	0.0482	0.9776	0.0338	0.9721	0.0231	0.9548	0.0200	0.9933	0.0245
13	0.9372	0.0620	0.9588	0.0416	0.9075	0.0274	0.9530	0.0253	0.9384	0.0304
17	0.8610	0.0652	0.9335	0.0463	0.9768	0.0313	0.9789	0.0285	0.9228	0.0331
20	0.8364	0.0673	0.9616	0.0481	0.9508	0.0320	0.9865	0.0297	0.9337	0.0346
23	1.1055	0.0819	0.9491	0.0499	0.9834	0.0343	0.9340	0.0302	0.9146	0.0355
26	0.7432	0.0691	0.8737	0.0493	0.9548	0.0348	0.9035	0.0307	0.8926	0.0362
28	0.8070	0.0706	0.8269	0.0474	1.0013	0.0351	0.8976	0.0303	0.8430	0.0349
30	0.9905	0.0801	0.9810	0.0530	0.9290	0.0348	0.9551	0.0320	0.8253	0.0352
32	0.8641	0.0753	1.0222	0.0545	0.9443	0.0352	0.9193	0.0317	0.9763	0.0388

Chapter Seven

Comparison with models

This Chapter presents a comparison of the experimental results with two models. The first one is a dynamical model, EPOS1.99 [144], taking into account numerous sources of particle correlations (see Sec. 7.1). The second one, the Power-law Model [145], produces particles correlated by the power law in the transverse-momentum difference together with fully uncorrelated particles (see Sec. 7.2). Particles produced by the model are injected into a detector simulation using the Geometry And Tracking (GEANT3) software [146]. This allows for the simulation of physical processes like particle decay and secondary interactions (see Sec. 4.3.2). The Detector Response Simulator generates TPC clusters with position and charge based on the output of GEANT3. Finally, the model events undergo the same reconstruction procedure as the experimental data (see Sec. 4.3.1). Such configuration allows comparison of MC-generated and reconstructed quantities. The output of the described procedure consists of two components:

(i) **pure EPOS:** A set of pure simulated events from the EPOS generator including information on particle momenta, mass, charge, and origin (primary interaction, decay, or secondary interaction).

(ii) **reconstructed EPOS:** Generated events are processed by GEANT3 and the detector response simulation, then reconstructed similarly to experimental data. Reconstructed EPOS data contains the same information as reconstructed experimental data.

A matching procedure links generated particles to reconstructed tracks. The procedure assigns each track with the most common points to the generated particle. It also estimates the number of secondary particles reconstructed as primary ones.

7.1 Comparison with EPOS model

The event generator Epos1.99 was chosen for its concordance with previous SHINE measurements [137] and consistent developer support. In Epos, particle correlations arise from conservation laws, and resonance decays, with no critical fluctuations.

To make a comparison, about 20 million minimum bias ^{40}Ar + ^{45}Sc events were generated using Epos1.99. The same set of event selection criteria is applied to the reconstructed Epos data as experimental data (see Sec. 5.1). The number of forward spectators was used to select 0–10% *central* Epos1.99 events of ^{40}Ar + ^{45}Sc collisions at 13*A*–75*A* GeV/*c*. As the number of forward spectators is an integer number, the following procedure was followed to select 0–10% *central* events of ^{40}Ar + ^{45}Sc interactions at 13*A*–75*A* GeV/*c*:

(i) all events with the number of forward spectators less than or equal X were selected, where a fraction of X-events is $\leq 10\%$ and a fraction of $(X+1)$-events is $> 10\%$.

(ii) Y% of events with the number of forward spectators equal to X+1 were randomly selected to complete the fraction of selected events to 10%.

The values of X and Y are given in Table. 7.1.

Table 7.1 The parameters X and Y used in the selection of 10% most *central* ^{40}Ar + ^{45}Sc events generated by Epos; see text for details.

p_{beam} (GeV/*c*)	X	Y (%)
13*A*	19	11
19*A*	17	60
30*A*	15	73
40*A*	15	20
75*A*	14	35

After applying the selection criteria to Epos events, the event statistics are summarized in Table 7.1. The statistics of the pure Epos events are higher than those of the experimental data (see Table 7.1). Selected protons and proton pairs (matching to the generated particles was used for

identification) were subject to the same cuts as the experimental data (see Sec. 5.2). Protons and proton pairs within the single-particle (see Sec. 5.3) and two-particle acceptance (see Sec. 3.4) maps were selected. Moreover, ≈60% of accepted protons were randomly selected for the analysis to consider the effect of the proton selection from the data.

Table 7.2 Event statistics of 0–10% *central* Epos1.99 and experimental data for ^{40}Ar + ^{45}Sc collisions at 13*A*–75*A* GeV/*c*.

p_{beam}(GeV/*c*)	13*A*	19*A*	30*A*	40*A*	75*A*
Experimental data	497k	524k	913k	1290k	1161k
Epos1.99	543k	648k	1169k	1408k	1308k

In the case of the critical correlations, the impact of the momentum resolution may be significant [107]. Thus, a comparison with models including short-range correlations in the transverse-

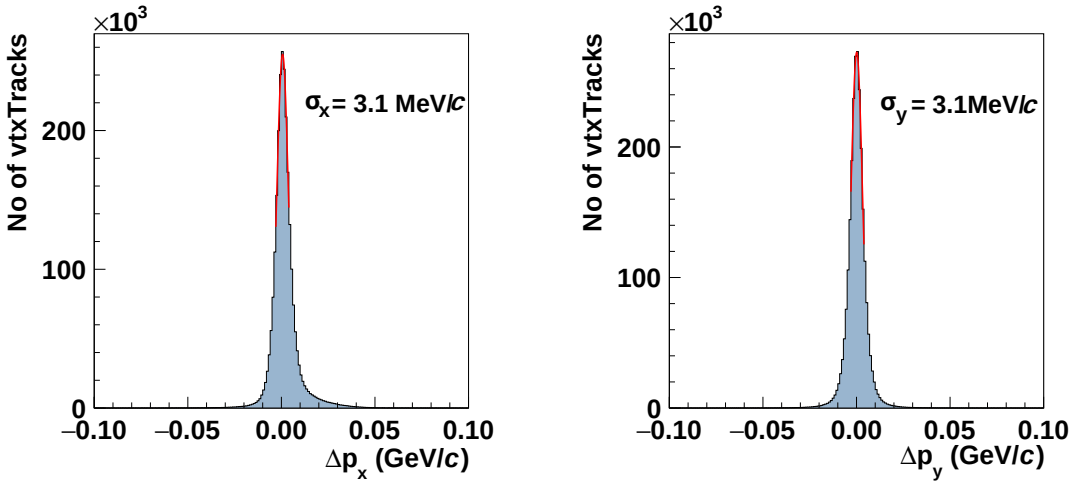

Figure 7.1 Example distribution of $\Delta p_x = p_x^{pureEPOS} - p_x^{recEPOS}$ (*left*) and $\Delta p_y = p_y^{pureEPOS} - p_y^{recEPOS}$ (*right*) for the selected proton candidates within the analysis acceptance from pure Epos and reconstructed Epos for 0–10% *central* ^{40}Ar + ^{45}Sc interactions at 75*A* GeV/*c* is shown here. Both the distributions are fitted by the Gaussian distribution with σ_x, and σ_y values.

momentum space requires smearing of momenta according to the experimental resolution, which

can be approximately parameterized as:

$$\begin{aligned} p_x^{\text{smeared}} &= p_x^{\text{original}} + \delta p_x \quad \text{and} \\ p_y^{\text{smeared}} &= p_y^{\text{original}} + \delta p_y, \end{aligned} \tag{7.1}$$

where δp_x, and δp_y were randomly drawn from a Gaussian distribution with σ_x, and σ_y (see Fig. 7.1) values for ^{40}Ar + ^{45}Sc collisions at beam momenta 13*A*–75*A* GeV/*c* from Table. 7.3.

Table 7.3 The σ_x and σ_y parameters, see text for details, used for smearing of proton transverse momentum in simulated ^{40}Ar + ^{45}Sc collisions at 13*A*–75*A* GeV/*c*.

p_{beam} (GeV/*c*)	σ_x (MeV/*c*)	σ_y (MeV/*c*)
13*A*	4.8	3.5
19*A*	4.6	3.4
30*A*	4.0	3.2
40*A*	3.5	3.1
75*A*	3.1	3.1

The pure (smeared) and reconstructed Epos events results are compared in Fig. 7.2 for 0–10% *central* ^{40}Ar + ^{45}Sc collisions at 13*A*–75*A* GeV/*c*. Closed black circles represent reconstructed Epos, and open rectangles indicate pure (smeared) Epos. No significant differences were found. One concludes that for the Epos-like physics, the biases of the experimental data are significantly smaller than the statistical uncertainties of the data.

The experimental results compared with the pure (smeared) Epos predictions for 0–10% *central* ^{40}Ar + ^{45}Sc collisions at 13*A*–75*A* GeV/*c* are shown in Fig. 7.3. The pure Epos and experimental results include the mTTD cut (see Table 5.6). The differences are significantly smaller than the statistical uncertainties of the experimental data. Protons generated by Epos do not show a significant correlation in the transverse-momentum space. In this case, the momentum resolution does not affect the results significantly [107].

Currently, no high statistics Epos1.99 data is available for ^{208}Pb + ^{208}Pb collisions at 13*A* and 30*A* GeV/*c* to compare with the proton intermittency results of the corresponding experimental data sets.

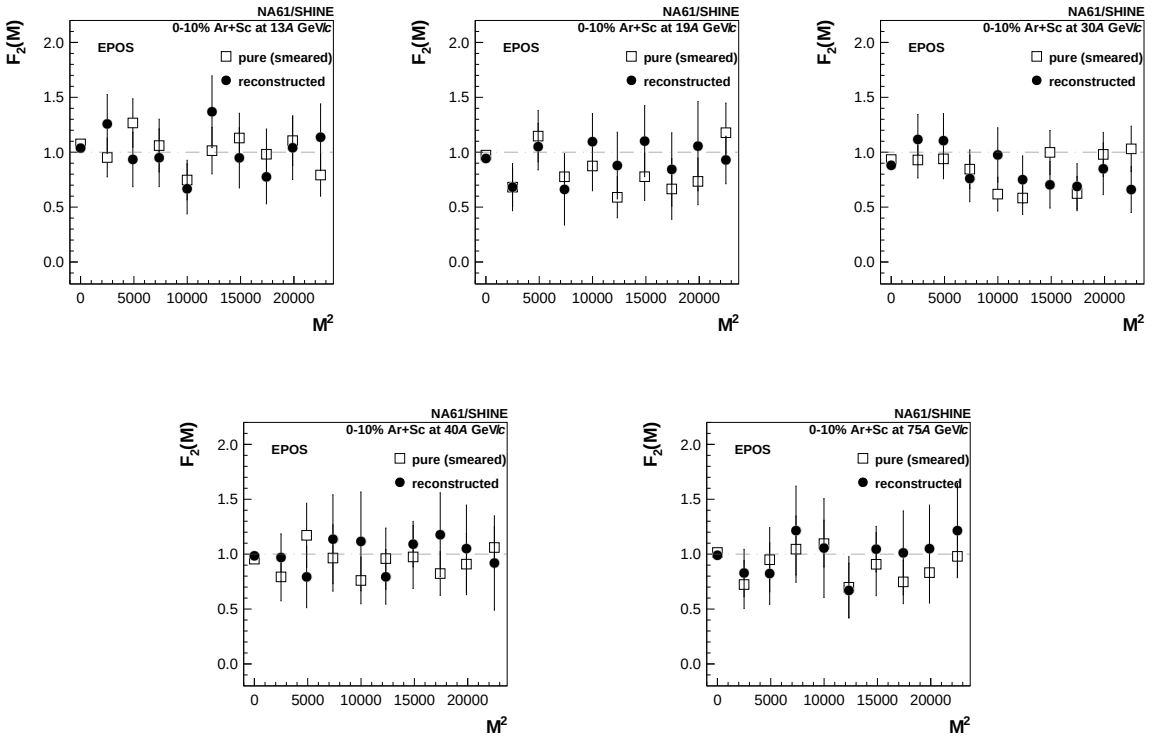

Figure 7.2 Results on the dependence of the scaled factorial moment of proton multiplicity distribution on the number of subdivisions in cumulative transverse-momentum space for events generated with Epos1.99. Results for 0–10% *central* ^{40}Ar + ^{45}Sc collisions at 13*A*–75*A* GeV/*c* are shown. Closed black circles represent reconstructed Epos, and open rectangles indicate pure (smeared) Epos. Both pure and reconstructed Epos include the mTTD cut. Only statistical uncertainties are indicated.

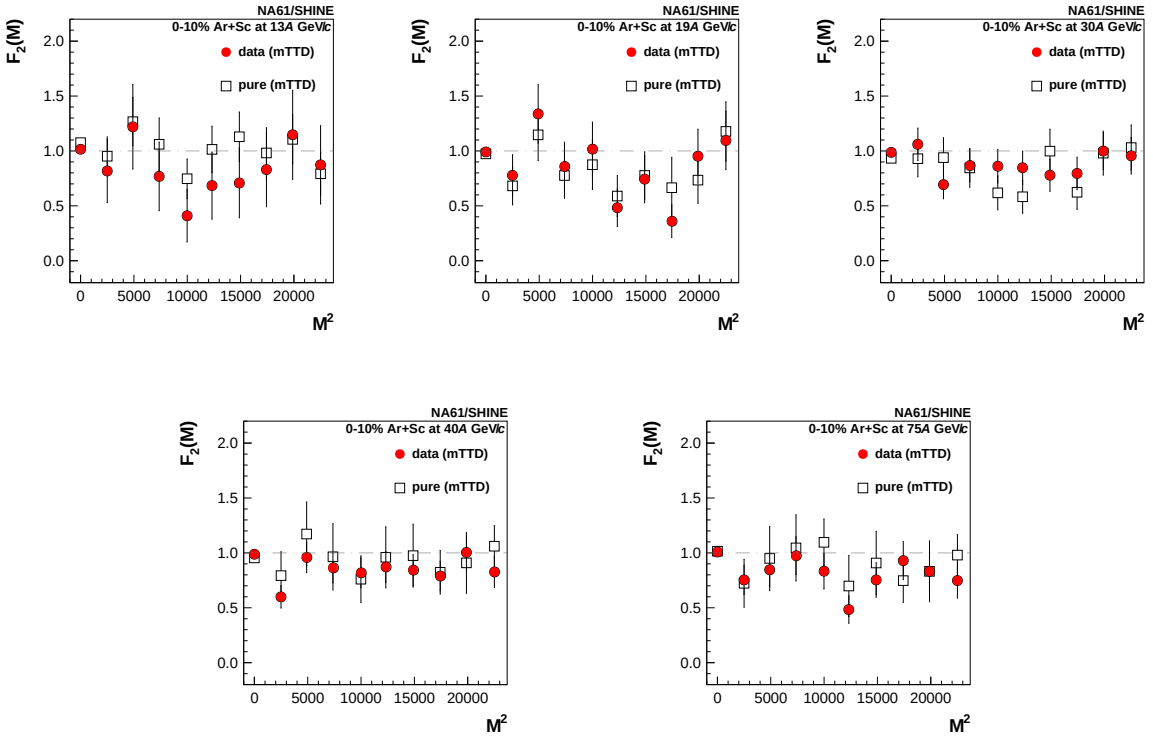

Figure 7.3 Results on the dependence of the scaled factorial moment of proton multiplicity distribution on the number of subdivisions in cumulative transverse-momentum space M for $1 \leq M \leq 150$. Closed circles indicate the experimental data. Corresponding results for mixed events (open triangles) and the EPOS1.99 model (open squares) were also shown for comparison. Results for 0–10% *central* ^{40}Ar + ^{45}Sc collisions at 13*A*–75*A* GeV/*c*, respectively. Results for data and EPOS were obtained using the mTTD cut. Only statistical uncertainties are indicated.

7.2 Comparison with Power-law Model

Inspired by the power-law correlations between particles near the critical point, the Power-law Model [79] compares with experimental results. Given single-particle transverse momentum and multiplicity distributions, it generates momenta of correlated and uncorrelated protons.

The model has two controllable parameters:

(i) fraction of correlated particles, *r*,

(ii) strength of the correlation (the power-law exponent), ϕ_2.

The transverse momentum of particles is sampled from a data-based distribution, while the azimuthal-angle distribution is assumed to be uniform. The momentum component along the beamline, p_z, is calculated assuming a uniform proton rapidity distribution from 0 to 0.75. Correlated-particle pairs have a transverse-momentum difference that follows a power-law distribution:

$$\rho(|\Delta\overrightarrow{p_T}|) \sim |\Delta\overrightarrow{p_T}|^{-\phi_2}, \tag{7.2}$$

where the exponent $0 \leq \phi_2 < 1$. For $r = 0$ or $\phi_2 = 0$, the Power-Law model results correspond to the mixed events results.

High-statistics data sets have been produced using the model for a given pair of model parameters, *r* and ϕ_2. The following effects have been included:

(i) Gaussian smearing of momentum components to mimic reconstruction resolution of the momentum (see Eq. 7.1),

(ii) single-particle acceptance map (see Sec. 5.3),

(iii) random exchange of 40% of correlated particles with uncorrelated particles to simulate 60% acceptance of protons (see Sec. 5.2.7),

(iv) two-particle acceptance map (see Sec. 3.4).

The influence of each of the above effects separately and all of them applied together on $F_2(M)$ is shown in Fig. 7.4 for *r* = 0.03 and ϕ_2 = 0.8 and fine subdivisions (M = 1, 50, ..., 150).

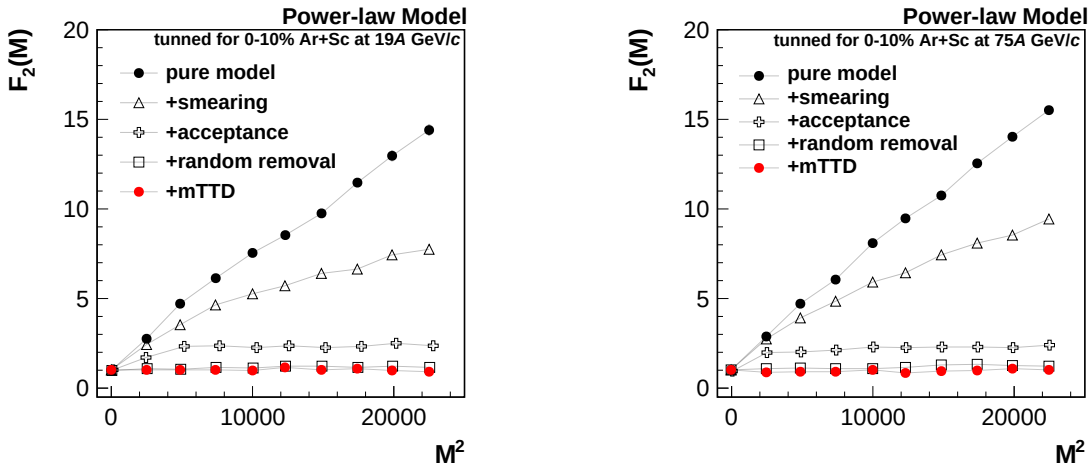

Figure 7.4 Example scaled-factorial moment's dependence on the number of subdivisions in the cumulative transverse momentum for ^{40}Ar + ^{45}Sc at 19*A* GeV/*c* (*left*) and 75*A* GeV/*c* (*right*) are shown for the Power-law Model with a power-law exponent of 0.80 and 3% correlated particles. Each line presents a result with a separate effect, and the red circles represent all of them combined.

The model data sets with all the above effects were analyzed similarly to the experimental data. The obtained $F_2(M)$ results were compared to corresponding experimental results, and χ^2 and p-value were calculated. Statistical uncertainties from a model with similar statistics to the data were used for the calculation. Examples of such comparison of results for two Power-law Model data sets with experimental data for ^{40}Ar + ^{45}Sc collisions at 19*A* GeV/*c* (*top*) and 75*A* GeV/*c* (*bottom*) are shown in Fig. 7.5. The *left* panel assumes only uncorrelated protons, whereas the *right* panel shows predictions for 2% of correlated protons with power-law exponent, $\phi_2 = 0.80$.

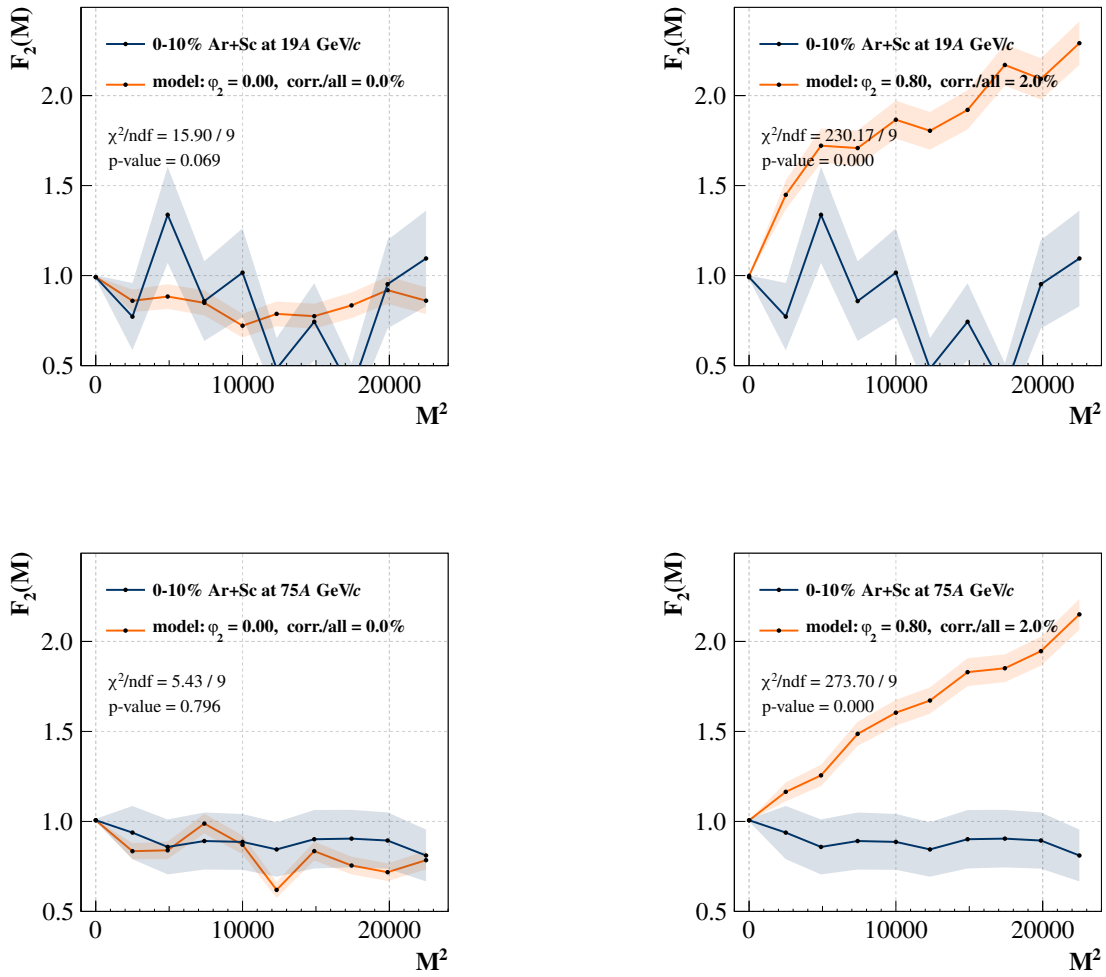

Figure 7.5 Example comparison of results for two Power-law Model data sets with experimental data for ^{40}Ar + ^{45}Sc collisions at 19*A* GeV/*c* (*top*) and 75*A* GeV/*c* (*bottom*) are shown. The *left* panel assumes only uncorrelated protons, whereas the *right* panel shows predictions for 2% of correlated protons with power-law exponent, $\phi_2 = 0.80$.

Figures 7.6 and 7.7 present the p-values obtained based on r and ϕ_2 for ^{208}Pb + ^{208}Pb collisions at 13A GeV/c and ^{40}Ar + ^{45}Sc collisions at 13A–75A GeV/c. White areas indicate a p-value of less than 1% and are excluded (for this model). For ^{208}Pb + ^{208}Pb 30A GeV/c, experimental results have low statistical uncertainties, but deviations from expected behavior (due to conservation laws, resonance decays, quantum statistics, and possible experimental biases) may lead to a significant decrease in p-values.

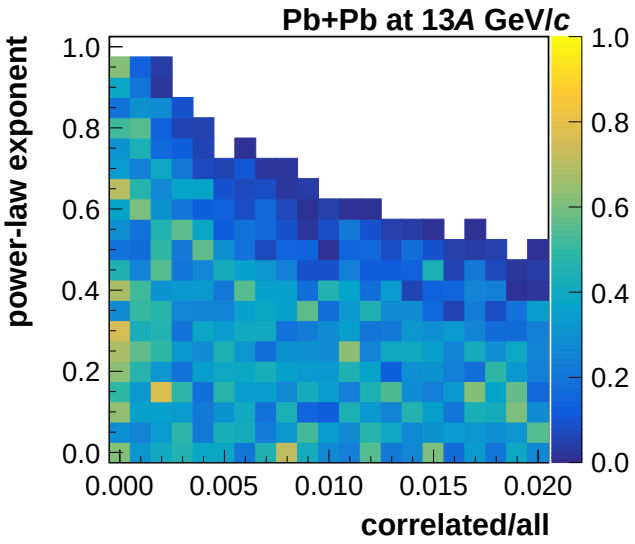

Figure 7.6 For the fine subdivisions ($1 \leq M \leq 150$), the exclusion plots for central ^{208}Pb + ^{208}Pb collisions at 13A GeV/c is shown using the Power-law Model parameters, including r and ϕ_2. The white areas correspond to p-values less than 1%.

At low energy ^{40}Ar + ^{45}Sc experimental data, $F_2(M)$ values were highly fluctuating, which increases χ^2–values to compare with the Power-law Model (see Fig. 7.5). As a result, exclusion plots at low energy are not very conclusive, particularly for ^{40}Ar + ^{45}Sc collisions at 19A GeV/c. The intermittency index, ϕ_2 for an infinite system at QCD CP is expected to be ϕ_2 = 5/6 [88], assuming that the latter belongs to the 3-D Ising universality class. If this value is set as the power-law exponent of the Power-law Model with fine subdivisions (see Fig. 7.6 and 7.7), for 0–10% *central* ^{208}Pb + ^{208}Pb collisions at 13A GeV/c and ^{40}Ar + ^{45}Sc collisions at 13A–75A GeV/c, an upper limit on the fraction of critical proton pairs ranges approximately from 0.1% to 0.3% depending on the collision energy (see Table 7.4).

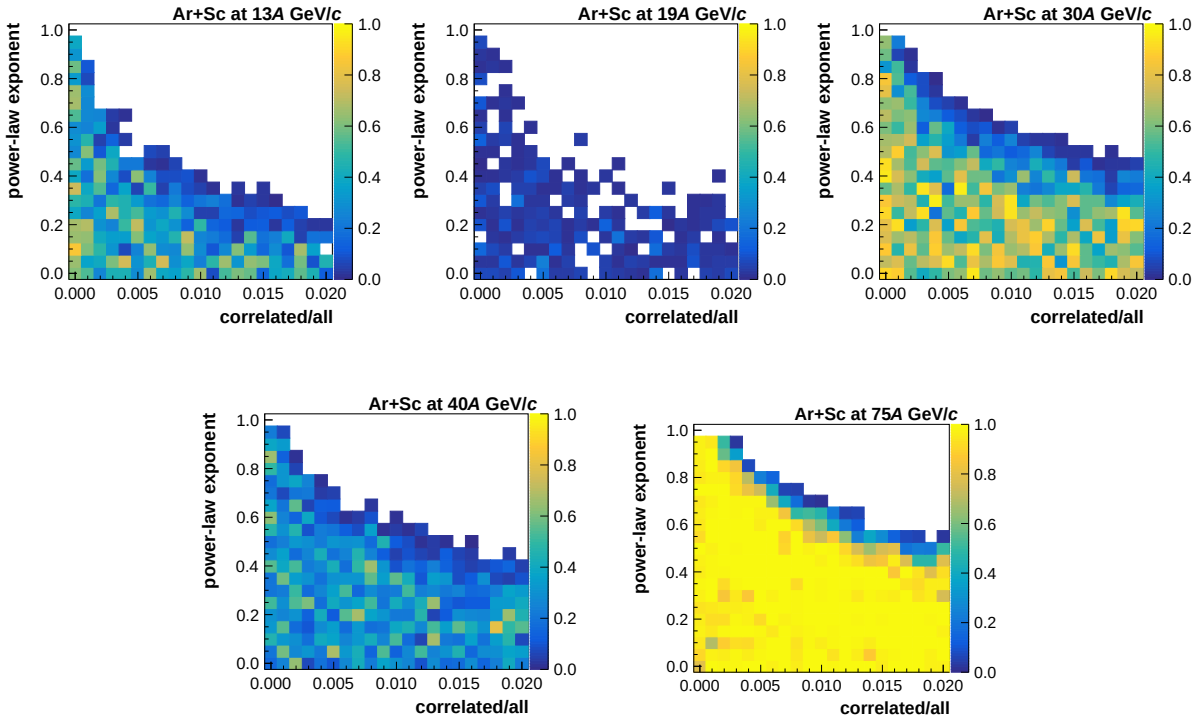

Figure 7.7 For the fine subdivisions ($1 \leq M \leq 150$), the exclusion plots for central ^{40}Ar + ^{45}Sc collisions at 13*A*–75*A* GeV/*c* are shown using the Power-law Model parameters, including r and ϕ_2. The white areas correspond to p-values less than 1%.

Table 7.4 An upper limit on the fraction of critical proton pairs for central ^{208}Pb + ^{208}Pb collisions at 13*A* GeV/*c* and ^{40}Ar + ^{45}Sc collisions at 13*A*–75*A* GeV/*c* considering ϕ_2 = 5/6 of the Power-law Model.

p_{beam} (GeV/*c*)	upper limit of critical proton pairs (%)
Pb+Pb	
13*A*	0.2
Ar+Sc	
13*A*	0.1
19*A*	≈0.2
30*A*	0.2
40*A*	0.2
75*A*	0.3

Chapter Eight

Summary

This thesis reports on the search for the critical point of strongly interacting matter in 0–10% *central* ^{208}Pb + ^{208}Pb collision at 13*A* and 30*A* GeV/*c*, and ^{40}Ar + ^{45}Sc collisions at beam momenta of 13*A*, 19*A*, 30*A*, 40*A*, and 75*A* GeV/*c* recorded by the NA61/SHINE experiment at the CERN SPS. It includes a brief review of the field, methodology, results, and comparison with models. The search was conducted using intermittency analysis in transverse momentum space applied to protons produced at mid-rapidity. In particular,

(i) Proton intermittency analysis in high energy physics to search for the critical point of strongly interacting matter was discussed in Chapter 2.

(ii) New approaches to the proton intermittency analysis to search for the critical point using cumulative variables and statistically independent data points were discussed in Chapter 3.

(iii) The NA61/SHINE experimental facility was discussed in Chapter 4.

(iv) The event and track selection was discussed in Chapter 5. Proton candidates were selected by the single and two-particle acceptance maps.

(v) Results on second scaled-factorial moments of proton multiplicity distribution in transverse-momentum space at mid-rapidity were presented in Chapter 6. Possible biases of the experimental results were estimated using the Epos1.99 model, and they are smaller than the statistical uncertainties of the experimental data.

(vi) Experimental results were compared with Epos1.99, and no significant differences were observed as discussed in Chapter 7.

(vii) The experimental data are consistent with the mixed events subject to the analysis acceptance maps. An upper limit on the fraction of critical proton pairs and the power of the correlation function was obtained based on a comparison with the Power-law Model discussed in Chapter 7.

The key physics result of the thesis is the absence of any indication of the critical point in 0–10% *central* ^{208}Pb + ^{208}Pb collisions at 13*A* and 30*A* GeV/*c*, and ^{40}Ar + ^{45}Sc collisions at 13*A*, 19*A*, 30*A*, 40*A*, and 75*A* GeV/*c*. The corresponding experimental results are summarized in Figs. 8.1 and 8.2, where second scaled-factorial moments for mid-rapidity protons are plotted as a function of the number of subdivisions in cumulative transverse-momentum space. These results allowed us to obtain the exclusion plots for the power-law correlated protons. Assuming, ϕ_2 = 5/6 as suggested by the QCD-inspired model [88], and using the Power-law Model [79] an upper limit on the fraction of critical proton pairs ranges from 0.1% to 0.3% depending on the data set (see Table 7.4).

The status of the NA61/SHINE critical point search via proton intermittency is summarized on the diagram of chemical freeze-out temperature and baryon-chemical potential [58] in Fig. 8.3.

The search for the critical point of strongly interacting matter in the NA61/SHINE data recorded within its system-size and energy scan continues. In particular, the results for Xe+La collisions are still to be obtained.

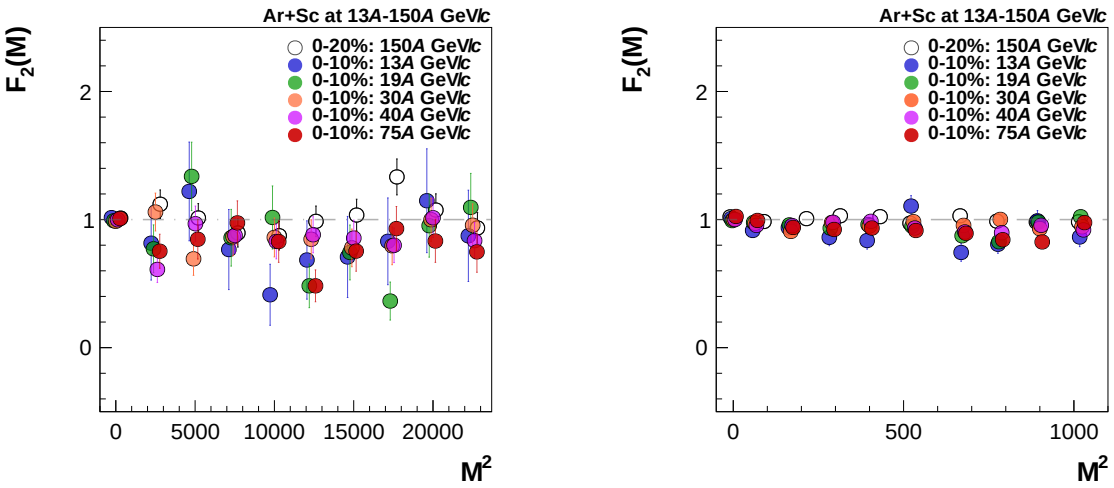

Figure 8.1 Summary of the proton intermittency results from the NA61/SHINE Ar+Sc energy scan. Results on the dependence of the second scaled-factorial moment of proton multiplicity distribution on the number of subdivisions in cumulative transverse momentum space M for $1 \leq M \leq 150$ (*left*) and $1 \leq M \leq 32$ (*right*) are shown. The open circles represent results on $0-20\%$ *central* ^{40}Ar + ^{45}Sc collisions at 150*A* GeV/*c* [79]. Closed circles indicate the experimental data results obtained within this work for 0–10% *central* ^{40}Ar + ^{45}Sc collisions at 13*A*–75*A* GeV/*c*. Only statistical uncertainties are indicated. Points for different energies are slightly shifted horizontal axis to increase readability.

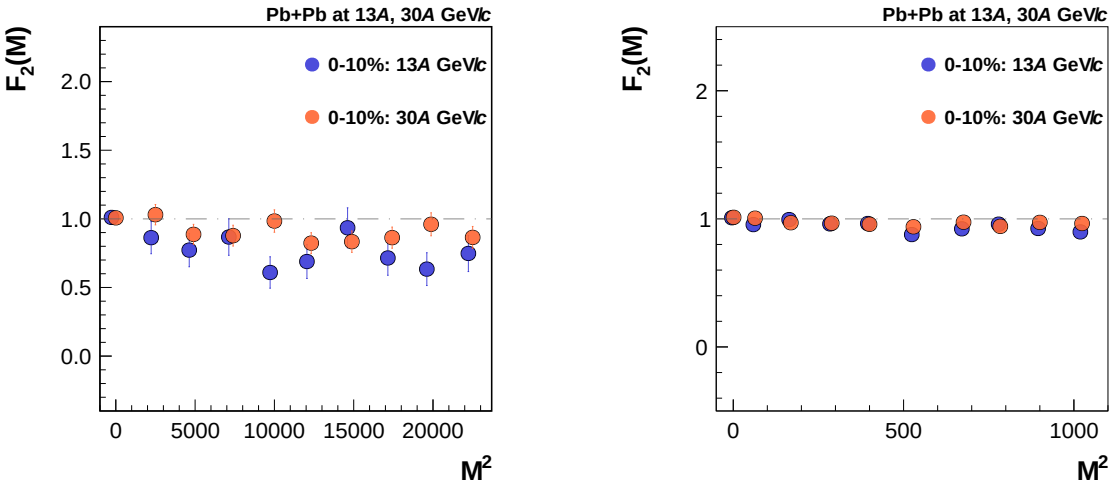

Figure 8.2 Summary of the proton intermittency results from the NA61/SHINE Pb+Pb energy scan. Results on the dependence of the second scaled-factorial moment of proton multiplicity distribution on the number of subdivisions in cumulative transverse momentum space M for $1 \leq M \leq 150$ (*left*) and $1 \leq M \leq 32$ (*right*) are shown. Closed circles indicate the experimental data results for 0–10% *central* ^{208}Pb + ^{208}Pb collisions at 13*A* and 30*A* GeV/*c*, obtained within this work. Only statistical uncertainties are indicated. Points for different energies are slightly shifted horizontal axis to increase readability.

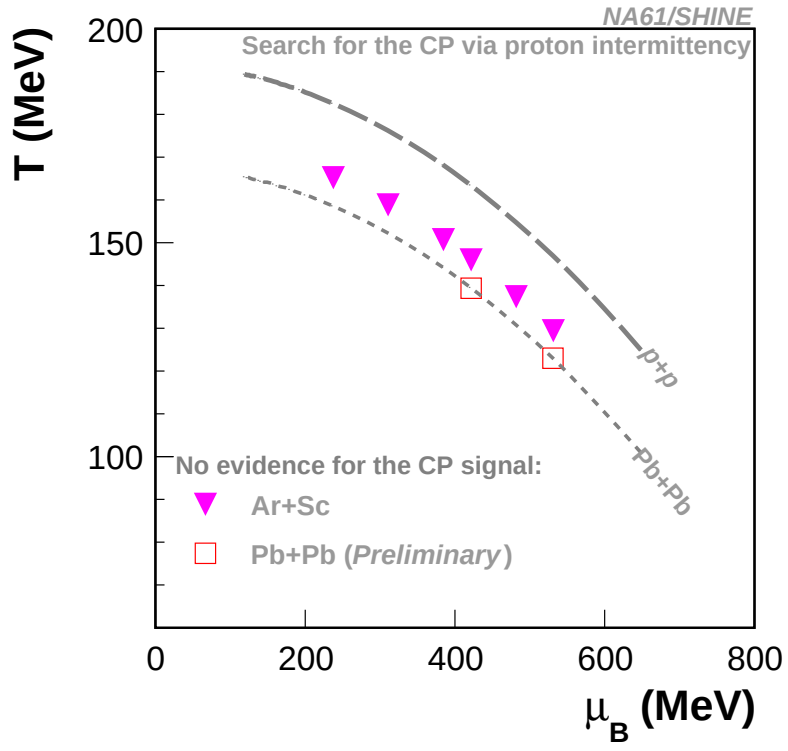

Figure 8.3 Diagram of chemical freeze-out temperature and baryon-chemical potential. The dashed line indicates parameters in *p*+*p* interactions and the dotted line in the *central* Pb+Pb collisions [58]. The colored points mark reactions for which the search for the critical point was conducted, and no evidence for the critical point was found.

APPENDIXES

Appendix A

Kinematic variables

A.1 NA61/SHINE coordinate system

In Chapter 2 Fig. 4.2 provides an overview of the NA61/SHINE detector and its coordinates. The system's origin is located at the beamline's center in the VTX-2 magnet. The system is right-handed, with the z axis coinciding with the beamline axis. The y axis is vertical and parallel to the electron drift velocity in TPCs, while the x axis is horizontal.

The azimuthal angle is defined as:

$$\phi = \arctan \frac{p_y}{p_x} \,. \tag{A.1}$$

The polar angle, denoted by $\theta = \arcsin \frac{p_\mathrm{T}}{p}$, measures the angle between a particle's direction and the z axis. When $\theta = 0$, the particle moves parallel to the beamline. The θ range between 0 and 2π.

A.2 Total momentum and transverse momentum variables

The total momentum is defined as the square root of momentum components in the coordinate system described in Section A.1 added in quadrature:

$$p = \sqrt{p_x^2 + p_y^2 + p_z^2} \,. \tag{A.2}$$

The z axis is considered parallel to the beamline, which means that the transverse variables are determined by their x and y components.The transverse momentum is:

$$p_\mathrm{T} = \sqrt{p_x^2 + p_y^2} \,. \tag{A.3}$$

A.3 Two-particle transverse momentum difference

The two-particle transverse momentum difference, Δp_T is defined as:

$$\Delta p_T = \sqrt{(p_{x_1} - p_{x_2})^2 + (p_{y_1} - p_{y_2})^2} \,, \tag{A.4}$$

where p_{x_1}, p_{x_2} and p_{y_1}, p_{y_2} are x and y component of the transverse momentum of particle 1 and 2 respectively.

A.4 Collision energy

The energy available in the center of mass is described by the Lorentz-invariant Mandelstam variable:

$$\sqrt{s} = \sqrt{(E_{\text{beam}} + E_{\text{target}})^2 - (p_{\text{beam}} + p_{\text{target}})^2 c^2} \,. \tag{A.5}$$

Typically, the energy per pair of nucleons at the center of mass is represented as $\sqrt{s_{NN}}$, where m_{beam}, m_{target}, and m_N all have the same value. In experiments using a fixed target, p_{target} equals zero, and E_{target} equals the mass of the ion utilized as the target.

$$\sqrt{s_{NN}} = \sqrt{\left(E_{\text{beam}} + m_N\right)^2 - p_{\text{beam}}^2 c^2} \,. \tag{A.6}$$

The kinematic variable values for every analyzed beam momentum are listed in Table A.1.

Table A.1 The values of the kinematic variables for each analyzed beam momentum.

p_{beam} (GeV/c)	E_{beam} (GeV)	$y_{\text{CMS}} = y_{\text{beam}}$	$\sqrt{s_{\text{NN}}}$ (GeV)
13.00	13.03	1.66	5.13
19.00	19.02	1.85	6.13
30.00	30.01	2.08	7.63
40.00	40.01	2.22	8.77
75.00	75.01	2.54	11.95

A.5 Rapidity

Rapidity is a measure of velocity in the realm of relativity due to its properties under Lorentz transformation. When multiple Lorentz boosts are performed in the same direction, they can be represented by a single boost. The transformation of velocity is given by:

$$\beta'' = |v/c|'' = \frac{\beta + \beta'}{1 + \beta\beta'} \,, \tag{A.7}$$

The velocity transformations is a non-linear. To address this issue, we use "rapidity" which is defined as $\beta = tanhy$ or $y = \frac{1}{2}\frac{1+\beta}{1-\beta}$. The rapidity is linear, $y'' = y + y'$ when undergoing a longitudinal Lorentz boost.

Alternatively one expresses particle's rapidity by its energy (*E*) and momentum component (p_z) parallel to the transformation direction:

$$y = \frac{1}{2} \ln \frac{E + p_z c}{E - p_z c} \,. \tag{A.8}$$

Inversely one can gets:

$$E = m_T cosh y, \; p_z = m_T sinh y \,, \tag{A.9}$$

where $m_T = \sqrt{m^2 + p_T^2}$. Rapidity can be easily transformed from the laboratory to the center of mass (CMS) frame:

$$y_{\text{CMS, frame}} = y_{\text{LAB, frame}} + y_{\text{CMS}} \,, \tag{A.10}$$

where y_{CMS} is defined as:

$$y_{\text{CMS}} = \arctan \frac{p_{\text{beam}} c}{E_{\text{beam}} + m_N} \,, \tag{A.11}$$

p_{beam} is the beam momentum, $E_{\text{beam}} = \sqrt{p_{\text{beam}}^2 c^2 + m_N^2}$ is the beam energy with m_N as the mass of a nucleon. In this thesis, rapidity is given in the center-of-mass frame.

In this thesis, the term "mid-rapidity" refers to a region in the y-axis that is close to y=0, specifically between y=0 and y=0.75. This refers to particles that are approximately perpendicularly to the beamline direction in the center of the mass system. The areas above $y = 0$ and below $y = 0$ are commonly known as the *forward* and *backward* rapidity regions, respectively.

In experimental particle physics, pseudo-rapidity, η, is a commonly used spatial coordinate describing the angle of a particle relative to the beam axis. It is defined as:

$$\eta = -ln \left[tan \left(\frac{\theta}{2} \right) \right] \,. \tag{A.12}$$

Appendix B

Critical point search observables

B.1 Extensive quantities

In the Wounded Nucleon Model [67] (WNM) or the Ideal Boltzmann Grand Canonical Ensemble (IB-GCE), an extensive quantity is directly proportional to either the number of Wounded Nucleons (W) or the volume (V). The following are the most popular extensive quantities:

$$\begin{aligned} \kappa_1 &= \langle N \rangle \,, \\ \kappa_2 &= \left\langle (\Delta N)^2 \right\rangle = \sigma^2 \,, \\ \kappa_3 &= \left\langle (\Delta N)^3 \right\rangle = S\sigma^3 \,, \\ \kappa_4 &= \left\langle (\Delta N)^4 \right\rangle - 3\left\langle (\Delta N)^2 \right\rangle^2 = \kappa\sigma^4 \,, \end{aligned} \tag{B.1}$$

where N is particle multiplicity, ΔN is $N - \langle N \rangle$, S is skewness, and κ is kurtosis.

Intensive quantities

When considering an event sample with a fixed value for either W (within WNM) or V (within IB-GCE), the ratio of any two extensive quantities is independent of W(N) when averages are calculated for events with the same W(N). This is an intensive quantity. To clarify, if A and B are two extensive event quantities, with $\langle A \rangle \sim W$ and $\langle B \rangle \sim W$, then their ratio is independent of W (or V).

$\langle A \rangle / \langle A \rangle = W \cdot \langle a \rangle / W \cdot \langle b \rangle = \langle a \rangle / \langle b \rangle$, where $\langle a \rangle = \langle A \rangle$ and $\langle b \rangle = \langle B \rangle$ for W = 1. Popular examples of intensive quantities are:

$$\begin{aligned} \kappa_2/\kappa_1 &= \omega[N] = \frac{\sigma^2[N]}{\langle N \rangle} = \frac{W \cdot \sigma^2[n]}{W \cdot \langle n \rangle} = \omega[n] \,, \\ \kappa_3/\kappa_2 &= S\sigma \,, \\ \kappa_4/\kappa_2 &= \kappa\sigma^2 \,, \end{aligned} \tag{B.2}$$

When comparing fluctuations for systems of different sizes, it's preferred to use intensive quantities.

B.1.1 SSFMs in the Wounded Nucleon Model

In the Wounded Nucleon Model (WNM), $N = \sum_{i=1}^{W} n_i$, where W is number of wounded nucleons, assumed to be constant. Then for an event, $\langle N \rangle = W \cdot \langle N \rangle$ and $\omega[N] = \omega[n]$. Considering second scaled-factorial moments, one gets:

$$F_2[N] = \frac{1}{W} F_2[n] + 1 - \frac{1}{W} . \tag{B.3}$$

In the WNM, the scaled-factorial moments are neither extensive ($\approx W$) nor intensive, but in the case $W \gg 1$ and $F_2[n]/W \gg 1$:

$$F_2[N] = \frac{1}{W} F_2[n] . \tag{B.4}$$

The scaled-factorial moments are inversely extensive [81].

B.1.2 Strongly intensive quantities

It is possible to create fluctuation measures that are not affected by fluctuations within the ideal Boltzmann gas in the grand canonical ensemble formulation (SM(IB-GCE)) and WNM. Using the second and first moments of the distribution of two extensive quantities, strongly intensive quantities [65] can be written as:

$$\Sigma^{AB} = \langle C \rangle^{-1} \left[\langle B \rangle \omega_A + \langle A \rangle \omega_B - 2 \left(\langle AB \rangle - \langle A \rangle \langle B \rangle \right) \right], \tag{B.5}$$

$$\Delta^{AB} = \langle C \rangle^{-1} \left[\langle B \rangle \omega_A - \langle A \rangle \omega_B \right], \tag{B.6}$$

where A and B are two extensive quantities and $\langle C_\Delta \rangle$ or $\langle C_\Sigma \rangle$ are the averages of any extensive quantity, e.g., $\langle A \rangle$ or $\langle B \rangle$.

For the study of transverse momentum fluctuations, one uses:

$$A = p_T = \sum_{i=1}^{N} p_{T_i}, \; B = N, \tag{B.7}$$

where p_{T_i} is the transverse momentum of particle *i*. There is an important difference between $\Delta[P_T, N]$ and $\Sigma[P_T, N]$. To calculate $\Delta[P_T, N]$ only the first two moments: $\langle P_T \rangle$, $\langle N \rangle$, and

$\left\langle P_T^2 \right\rangle$, $\left\langle N^2 \right\rangle$ are required to calculate but to calculate $\Sigma\left[P_T, N\right]$ needs $\langle P_T N\rangle - \langle P_T\rangle \langle N\rangle$. The quantity $\Sigma\left[P_T, N\right]$ and $\Delta\left[P_T, N\right]$ can be expressed as:

$$\Sigma\left[P_T, N\right] = \frac{1}{C_\Sigma}\left[\langle N\rangle \omega_{P_T} + \langle P_T\rangle \omega_N - 2\left(\langle P_T N\rangle - \langle P_T\rangle \langle N\rangle\right)\right], \tag{B.8}$$

$$\Delta\left[P_T, N\right] = \frac{1}{\langle C_\Delta\rangle}\left[\langle N\rangle \omega_{P_T} - \langle P_T\rangle \omega_N\right], \tag{B.9}$$

where ω is the scaled variance of a given variable (e.g., $\omega[N] = \frac{\left\langle N^2\right\rangle - \langle N\rangle^2}{\langle N\rangle}$). The quantities are constructed to be zero when there are no fluctuations (when P_T and N remain constant) and one when there is independent particle production.

B.1.3 Short-range correlations

The two-particle correlation function, $C(q)$ can be parameterized via Levy-shaped source (1-D) as [71]:

$$C(q) \simeq 1 + \lambda \cdot e^{(-qR)^\alpha}, \tag{B.10}$$

The formula for calculating the distance between two points, represented by p_1 and p_2, in the LCMS system is given by $q = |p_1 - p_2|_{LCMS}$. The variable $lambda$ describes the correlation length, while the length of homogeneity is determined by R. The value of the Levy exponent α determines the shape of the source. When $\alpha = 2$, the predicted source shape is Gaussian, which is a simple hydro. For $\alpha < 2$, there is anomalous diffusion and a generalized central limit theorem applies. The conjectured value at the critical point is $\alpha = 0.5$.

Appendix C

Sc and Pb Target specifications

NA61/SHINE has collected data using Be, C, Sc, La, and Pb targets, with thickness between 1 cm and 2 cm, and transverse dimensions of around 2.5×2.5 cm^2. Specifications of ^{208}Pb and ^{45}Sc targets are given in Table C.1.

Table C.1 Specification of ^{208}Pb + ^{208}Pb and ^{40}Ar+^{45}Sc 7Sc target.

Material name	Material Z	Material A	Material density (g/cm^3)	Material inter-action length (g/cm^2)	Cross-section shape	Length (cm)	Center z (cm)	Material molar mass (g/mol)
Pb	82	208	11.34	199.6	square	0.1	-591.90	207.977
Sc	21	45	2.985	123.9	square	0.6	-580.00	45.956

The target samples are checked for possible contamination using a Wavelength Dispersive X-Ray Fluorescence (WDXRF) [128]. WDXRF measurements are used to estimate the biases to cross-section calculations caused by impurities in the target. The ^{208}Pb and ^{45}Sc target impurities studies [128] done at Jan Kochanowski University at Kielce are summarized in Table C.2.

Table C.2 Measurement of the ^{45}Sc and ^{208}Pb target impurities using WDXRF technique [128]

	^{45}Sc sample (ϕ = 40nm)	^{208}Pb sample (ϕ = 40nm)
Element	concentration$\pm$ error (%)	concentration$\pm$ error (%)
Al	0.144	0.006
Bi	0.028	–
Ca	0.008	0.026
Cl	0.011	–
Cu	0.073	0.045
Fe	0.130	0.147
Hg	–	0.044
Mg	0.008	–
Nd	–	0.049
Ni	0.027	0.027
Pb	0.003	99.45$\pm$0.99
Rb	–	0.129
S	0.006	0.128
Sc	99.29$\pm$1.00	–
Si	0.034	0.191
Ta	0.065	–
Ti	0.0157	–
W	0.017	–
Y	0.020	–

Appendix D

Theoretical Bethe-Bloch formula

Using the Bethe-Bloch formula [130], particle identification is possible through energy loss per unit length, $\left\langle -\frac{dE}{dx} \right\rangle$ and momentum measurements in TPCs:

$$\left\langle -\frac{dE}{dx} \right\rangle = Kz^2 \frac{Z}{A} \frac{1}{\beta^2} \left[\frac{1}{2} ln \frac{2m_e c^2 \beta^2 \gamma^2 W_{max}}{I^2} - \beta^2 - \frac{\delta(\beta\gamma)}{2} \right]. \tag{D.1}$$

In the formula K = 0.307 MeV mol^{-1} cm^2, z represents the charge of the incident particle, while Z and A denote the absorber's atomic number and atomic mass. Additionally, $\beta = v/c$ signifies the velocity of the particle, m_e represents the mass of an electron, I denotes the mean excitation energy of the absorber, W_{max} indicates the maximum possible energy transfer in a single collision, and $\delta(\beta\gamma)$ refers to the density effect correction to ionization energy loss.

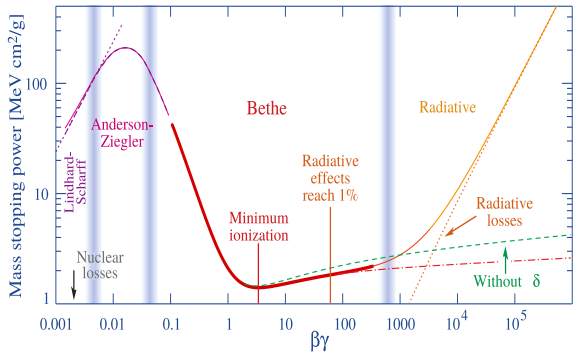

Figure D.1 The energy loss per unit length, denoted as $\left\langle -\frac{dE}{dx} \right\rangle$, as function of $\beta\gamma$. A thick red line indicates the relevant region for TPC operation in a typical high-energy physics experiment. The figure is taken from Ref. [130].

Figure D.1 illustrates the dependence of mass stopping power for muons traversing a copper medium, as a function of $\beta\gamma$. The red line highlighted in the curve corresponds to the region described by formula D.1. Particle velocity directly influences energy loss per unit length. Thus,

determining particle momentum and mean energy loss independently allows for determining particle mass.

Appendix E

Data-based centrality selection

Centrality selection for the model-based and data-based methods was made for ^{208}Pb + ^{208}Pb collisions at 13*A* and 30*A* GeV/*c*. The model-based method was discussed in Sec. 5.1.3. The data-based method will be briefly discussed in this Appendix, as an example events recorded at 13*A* GeV/*c* are used.

The data were taken using two target configurations: target inserted (target IN) and target removed (target R). A summary of target IN and target R statistics of the collected Pb+Pb data is given in Table. 4.3. The target R data was collected to correct for interactions of beam particles with the material surrounding the target (off-target interactions). The fitted z vertex position of primary interactions at 13*A* GeV/*c* for the target IN and target R data using T1 trigger in a broad range and an explanation of the origin of different peaks is present in Fig. E.1. The distribution for the data recorded with the ^{208}Pb target removed was scaled by a normalization factor,

$$\epsilon = N_{\mathrm{I}}[-685 < z < -610 \text{ cm}]/N_{\mathrm{R}}[-685 < z < -610 \text{ cm}] \ , \tag{E.1}$$

where $N_{\mathrm{I}}[-685 < z < -610 \text{ cm}]$ and $N_{\mathrm{R}}[685 < z < -610 \text{ cm}]$ are the numbers of events with the T1 trigger for the ^{45}Sc target inserted and removed data sets, respectively. The normalization region $-685 < z < -610$ cm was selected. The resulting normalization factors is $\epsilon = 6.0$.

The PSD energy distribution of target R is scaled by the normalization factor and subtracted from the target IN PSD energy to correct for off-target interactions. The normalized subtracted PSD energy distribution is shown in Fig. E.2 (*left*). The normalized subtracted PSD energy distribution was transformed into a cumulative distribution to calculate E_{PSD} limits for 0-10% of the central events. The desired centrality and corresponding E_{PSD} limits are mentioned in Fig. E.2 (*right*). The lowest values of E_{PSD} for different centrality intervals from the model-based (see Sec. 5.1.3) and the data-based method are given in Table E.1

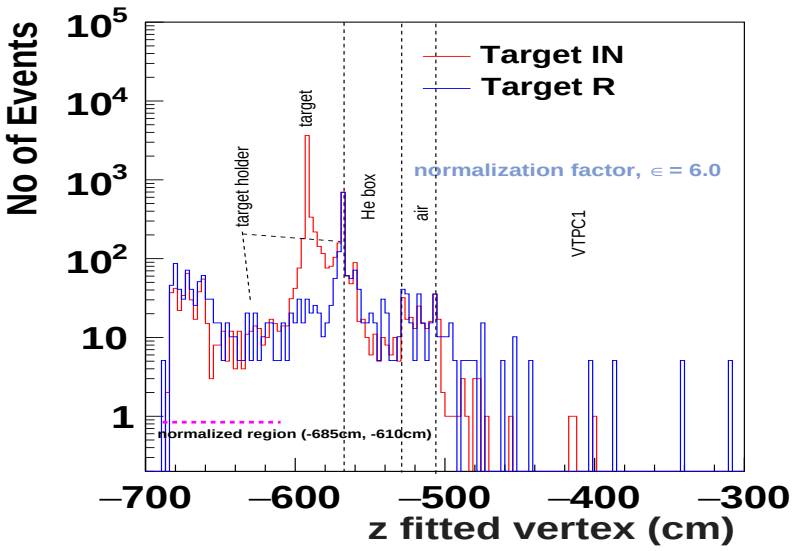

Figure E.1 An example distribution of fitted vertex z coordinate for ^{208}Pb + ^{208}Pb collisions at 13*A* GeV/*c* with ^{208}Pb target inserted and target removed (scaled as explained in the text) for the T1 trigger. Sources of peaks coming from beam interactions with experimental setup are explained.

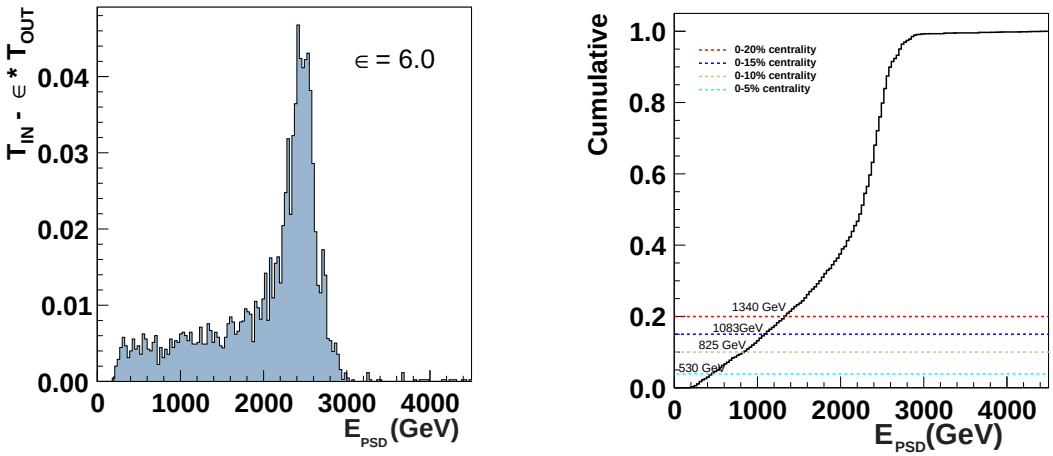

Figure E.2 *Left:* The normalized subtracted PSD energy distribution for ^{208}Pb + ^{208}Pb collisions at 13*A* GeV/*c*. The PSD energy distribution of the target R data set was scaled by the normalization factor and subtracted from the target IN PSD energy distribution. *Right:* The normalized subtracted PSD energy distribution transformed into cumulative distribution to calculate E_{PSD} limits for 0-10% of the central events.

Table E.1 The lowest value of E_{PSD} for 5%, 10%, 15%, 20% centrality interval from the model-based and the data-based method for ^{208}Pb + ^{208}Pb collisions at 13*A* GeV/*c* beam-momentum data set.

	data-based method	model-based method
centrality interval	E_{PSD} (GeV) limits	E_{PSD} (GeV) limits
5%	498	530
10%	720	825
15%	915	1083
20%	1120	1340

Bibliography

[1] P. Braun-Munzinger and J. Wambach. "The Phase Diagram of Strongly-Interacting Matter". In: Rev. Mod. Phys. 81 (2009), pp. 1031–1050. DOI: 10.1103/RevModPhys.81.1031. arXiv: 0801.4256 [hep-ph].

[2] M. E. Fisher. "The theory of condensation and the critical point". In: Physics Physique Fizika 3.5 (1967), pp. 255–283. DOI: 10.1103/PhysicsPhysiqueFizika.3.255.

[3] Miklos Gyulassy. "The QGP discovered at RHIC". In: Structure and Dynamics of Elementary Matter. Mar. 2004, pp. 159–182. arXiv: nucl-th/0403032.

[4] Mark I. Gorenstein, V. K. Petrov, and G. M. Zinovev. "Phase Transition in the Hadron Gas Model". In: Phys. Lett. B 106 (1981), pp. 327–330. DOI: 10.1016/0370-2693(81)90546-3.

[5] Edward V. Shuryak. "Quantum Chromodynamics and the Theory of Superdense Matter". In: Phys. Rept. 61 (1980), pp. 71–158. DOI: 10.1016/0370-1573(80)90105-2.

[6] Misha A. Stephanov, K. Rajagopal, and Edward V. Shuryak. "Event-by-event fluctuations in heavy ion collisions and the QCD critical point". In: Phys. Rev. D 60 (1999), p. 114028. DOI: 10.1103/PhysRevD.60.114028. arXiv: hep-ph/9903292.

[7] Mikhail A. Shifman, A. I. Vainshtein, and Valentin I. Zakharov. "QCD and Resonance Physics. Theoretical Foundations". In: Nucl. Phys. B 147 (1979), pp. 385–447. DOI: 10.1016/0550-3213(79)90022-1.

[8] David J. Gross and Frank Wilczek. "Ultraviolet Behavior of Nonabelian Gauge Theories". In: Phys. Rev. Lett. 30 (1973). Ed. by J. C. Taylor, pp. 1343–1346. DOI: 10.1103/PhysRevLett.30.1343.

[9] H. David Politzer. “Reliable Perturbative Results for Strong Interactions?” In: Phys. Rev. Lett. 30 (1973). Ed. by J. C. Taylor, pp. 1346–1349. DOI: 10.1103/PhysRevLett.30.1346.

[10] V. N. Gribov. “The Theory of quark confinement”. In: Eur. Phys. J. C 10 (1999). Ed. by J. Nyiri, pp. 91–105. DOI: 10.1007/s100529900052. arXiv: hep-ph/9902279.

[11] Mikhail A. Stephanov. “QCD phase diagram and the critical point”. In: Prog. Theor. Phys. Suppl. 153 (2004). Ed. by Berndt Muller and C. I. Tan, pp. 139–156. DOI: 10.1142/S0217751X05027965. arXiv: hep-ph/0402115.

[12] Kenji Fukushima and Chihiro Sasaki. “The phase diagram of nuclear and quark matter at high baryon density”. In: Prog. Part. Nucl. Phys. 72 (2013), pp. 99–154. DOI: 10.1016/j.ppnp.2013.05.003. arXiv: 1301.6377 [hep-ph].

[13] Stefan B. Ruester et al. “The Phase diagram of neutral quark matter: Self-consistent treatment of quark masses”. In: Phys. Rev. D 72 (2005), p. 034004. DOI: 10.1103/PhysRevD.72.034004. arXiv: hep-ph/0503184.

[14] C. Greiner, P. Koch, and Horst Stoecker. “Separation of Strangeness from Antistrangeness in the Phase Transition from Quark to Hadron Matter: Possible Formation of Strange Quark Matter in Heavy Ion Collisions”. In: Phys. Rev. Lett. 58 (1987), pp. 1825–1828. DOI: 10.1103/PhysRevLett.58.1825.

[15] Edward V. Shuryak. “Multiparticle production in high energy particle collisions.” In: Yad.Fiz. 16 (1972), pp. 395–405.

[16] F. Becattini et al. “Chemical equilibrium in nucleus nucleus collisions at relativistic energies”. In: Phys. Rev. C 69 (2004), p. 024905. DOI: 10.1103/PhysRevC.69.024905. arXiv: hep-ph/0310049.

[17] Subhasis Samanta, Sandeep Chatterjee, and Bedangadas Mohanty. “Exploring the hadron resonance gas phase on the QCD phase diagram”. In: J. Phys. G 46.6 (2019), p. 065106. DOI: 10.1088/1361-6471/ab1a6b. arXiv: 1803.03844 [hep-ph].

[18] Ulrich W. Heinz and Maurice Jacob. “Evidence for a new state of matter: An Assessment of the results from the CERN lead beam program”. In: (Jan. 2000). arXiv: nucl-th/0002042.

[19] Miklos Gyulassy and Larry McLerran. “New forms of QCD matter discovered at RHIC”. In: Nucl. Phys. A 750 (2005). Ed. by D. Rischke and G. Levin, pp. 30–63. DOI: 10.1016/j.nuclphysa.2004.10.034. arXiv: nucl-th/0405013.

[20] John W. Harris and Berndt Müller. “”QGP Signatures” Revisited”. In: (Aug. 2023). arXiv: 2308.05743 [hep-ph].

[21] D. H. Rischke et al. “Phase Transition From Hadron Gas to Quark Gluon Plasma: Influence of the Stiffness of the Nuclear Equation of State”. In: J. Phys. G 14 (1988), p. 191. DOI: 10.1088/0305-4616/14/2/011.

[22] Adam Bzdak et al. “Mapping the Phases of Quantum Chromodynamics with Beam Energy Scan”. In: Phys. Rept. 853 (2020), pp. 1–87. DOI: 10.1016/j.physrep.2020.01.005. arXiv: 1906.00936 [nucl-th].

[23] H. Sazdjian. “Introduction to chiral symmetry in QCD”. In: EPJ Web Conf. 137 (2017). Ed. by Y. Foka, N. Brambilla, and V. Kovalenko, p. 02001. DOI: 10.1051/epjconf/201713702001. arXiv: 1612.04078 [hep-ph].

[24] Krishna Rajagopal and Frank Wilczek. “The Condensed matter physics of QCD”. In: At the frontier of particle physics. Handbook of QCD. Vol. 1-3. Ed. by M. Shifman and Boris Ioffe. Nov. 2000, pp. 2061–2151. DOI: 10.1142/9789812810458_0043. arXiv: hep-ph/0011333.

[25] Robert D. Pisarski and Frank Wilczek. “Remarks on the Chiral Phase Transition in Chromodynamics”. In: Phys. Rev. D 29 (1984), pp. 338–341. DOI: 10.1103/PhysRevD.29.338.

[26] A. Bazavov et al. “Equation of state in (2+1)-flavor QCD”. In: Phys. Rev. D 90 (2014), p. 094503. DOI: 10.1103/PhysRevD.90.094503. arXiv: 1407.6387 [hep-lat].

[27] N. Cabibbo and G. Parisi. “Exponential Hadronic Spectrum and Quark Liberation”. In: Phys. Lett. B 59 (1975), pp. 67–69. DOI: 10.1016/0370-2693(75)90158-6.

[28] Tom Banks and A. Casher. “Chiral Symmetry Breaking in Confining Theories”. In: Nucl. Phys. B 169 (1980), pp. 103–125. DOI: 10.1016/0550-3213(80)90255-2.

[29] Kenji Fukushima. “Chiral Symmetry and Heavy-Ion Collisions”. In: J. Phys. G 35 (2008). Ed. by Jan-e Alam et al., p. 104020. DOI: 10.1088/0954-3899/35/10/104020. arXiv: 0806.0292 [hep-ph].

[30] P. Castorina, R. V. Gavai, and H. Satz. “The QCD Phase Structure at High Baryon Density”. In: Eur. Phys. J. C 69 (2010), pp. 169–178. DOI: 10.1140/epjc/s10052-010-1358-7. arXiv: 1003.6078 [hep-ph].

[31] Frank R. Brown et al. “On the existence of a phase transition for QCD with three light quarks”. In: Phys. Rev. Lett. 65 (1990), pp. 2491–2494. DOI: 10.1103/PhysRevLett.65.2491.

[32] David J. Gross, Robert D. Pisarski, and Laurence G. Yaffe. “QCD and Instantons at Finite Temperature”. In: Rev. Mod. Phys. 53 (1981), p. 43. DOI: 10.1103/RevModPhys.53.43.

[33] Y. Aoki et al. “The Order of the quantum chromodynamics transition predicted by the standard model of particle physics”. In: Nature 443 (2006), pp. 675–678. DOI: 10.1038/nature05120. arXiv: hep-lat/0611014.

[34] V. A. Goy et al. “Sign problem in finite density lattice QCD”. In: PTEP 2017.3 (2017), p. 031D01. DOI: 10.1093/ptep/ptx018. arXiv: 1611.08093 [hep-lat].

[35] M. Asakawa and K. Yazaki. “Chiral Restoration at Finite Density and Temperature”. In: Nucl. Phys. A 504 (1989), pp. 668–684. DOI: 10.1016/0375-9474(89)90002-X.

[36] A. Barducci et al. “Chiral Phase Transitions in QCD for Finite Temperature and Density”. In: Phys. Rev. D 41 (1990), p. 1610. DOI: 10.1103/PhysRevD.41.1610.

[37] Juergen Berges and Krishna Rajagopal. “Color superconductivity and chiral symmetry restoration at nonzero baryon density and temperature”. In: Nucl. Phys. B 538 (1999), pp. 215–232. DOI: 10.1016/S0550-3213(98)00620-8. arXiv: hep-ph/9804233.

[38] Adam Miklos Halasz et al. “On the phase diagram of QCD”. In: Phys. Rev. D 58 (1998), p. 096007. DOI: 10.1103/PhysRevD.58.096007. arXiv: hep-ph/9804290.

[39] N. G. Antoniou and A. S. Kapoyannis. “Bootstraping the QCD critical point”. In: Phys. Lett. B 563 (2003), pp. 165–172. DOI: 10.1016/S0370-2693(03)00654-3. arXiv: hep-ph/0211392.

[40] Yoshitaka Hatta and Takashi Ikeda. “Universality, the QCD critical / tricritical point and the quark number susceptibility”. In: Phys.Rev. D67 (2003), p. 014028. DOI: 10.1103/PhysRevD.67.014028. arXiv: hep-ph/0210284 [hep-ph].

[41] Z. Koba, Holger Bech Nielsen, and P. Olesen. “Scaling of multiplicity distributions in high-energy hadron collisions”. In: Nucl. Phys. B 40 (1972), pp. 317–334. DOI: 10.1016/0550-3213(72)90551-2.

[42] Z. Fodor and S. D. Katz. “Lattice determination of the critical point of QCD at finite T and mu”. In: JHEP 03 (2002), p. 014. DOI: 10.1088/1126-6708/2002/03/014. arXiv: hep-lat/0106002.

[43] Philippe de Forcrand and Owe Philipsen. “The QCD phase diagram for three degenerate flavors and small baryon density”. In: Nucl. Phys. B 673 (2003), pp. 170–186. DOI: 10.1016/j.nuclphysb.2003.09.005. arXiv: hep-lat/0307020.

[44] Shinji Ejiri et al. “Study of QCD thermodynamics at finite density by Taylor expansion”. In: Prog. Theor. Phys. Suppl. 153 (2004). Ed. by A. Nakamura et al., pp. 118–126. DOI: 10.1143/PTPS.153.118. arXiv: hep-lat/0312006.

[45] Frithjof Karsch. “Lattice QCD at non-zero temperature and density”. In: (Dec. 2022). arXiv: 2212.03015 [hep-lat].

[46] Philippe de Forcrand and Owe Philipsen. “The QCD phase diagram for small densities from imaginary chemical potential”. In: Nucl. Phys. B 642 (2002), pp. 290–306. DOI: 10.1016/S0550-3213(02)00626-0. arXiv: hep-lat/0205016.

[47] D. Bollweg et al. “Taylor expansions and Padé approximants for cumulants of conserved charge fluctuations at nonvanishing chemical potentials”. In: Phys. Rev. D 105.7 (2022), p. 074511. DOI: 10.1103/PhysRevD.105.074511. arXiv: 2202.09184 [hep-lat].

[48] Peter Braun-Munzinger and Benjamin Dönigus. “Loosely-bound objects produced in nuclear collisions at the LHC”. In: Nucl. Phys. A 987 (2019), pp. 144–201. DOI: 10.1016/j.nuclphysa.2019.02.006. arXiv: 1809.04681 [nucl-ex].

[49] K. Shigaki et al. “A forward magnetic spectrometer system for high-energy heavy ion experiments”. In: Nucl. Instrum. Meth. A 438 (1999), pp. 282–301. DOI: 10.1016/S0168-9002(99)00680-4.

[50] John Adams et al. “Experimental and theoretical challenges in the search for the quark gluon plasma: The STAR Collaboration’s critical assessment of the evidence from RHIC collisions”. In: Nucl. Phys. A 757 (2005), pp. 102–183. DOI: 10.1016/j.nuclphysa.2005.03.085. arXiv: nucl-ex/0501009.

[51] V. D. Kekelidze. “NICA project at JINR: status and prospects”. In: JINST 12.06 (2017). Ed. by Lev Shekhtman, p. C06012. DOI: 10.1088/1748-0221/12/06/C06012.

[52] T. Ablyazimov et al. “Challenges in QCD matter physics –The scientific programme of the Compressed Baryonic Matter experiment at FAIR”. In: Eur. Phys. J. A 53.3 (2017), p. 60. DOI: 10.1140/epja/i2017-12248-y. arXiv: 1607.01487 [nucl-ex].

[53] D. Krämer. “Current Status of the FAIR project”. In: Conf. Proc. C 070625 (2007). Ed. by C. Petit-Jean-Genaz, p. 2598. DOI: 10.1109/PAC.2007.4440721.

[54] H. Sako. “Studies of extremely dense matter in heavy-ion collisions at J-PARC”. In: Nucl. Phys. A 982 (2019). Ed. by Federico Antinori et al., pp. 959–962. DOI: 10.1016/j.nuclphysa.2018.11.027.

[55] S. Afanasiev et al. “The NA49 large acceptance hadron detector”. In: Nucl. Instrum. Meth. A 430 (1999), pp. 210–244. DOI: 10.1016/S0168-9002(99)00239-9.

[56] N. Abgrall et al. “NA61/SHINE facility at the CERN SPS: beams and detector system”. In: JINST 9 (2014), P06005. DOI: 10.1088/1748-0221/9/06/P06005. arXiv: 1401.4699 [physics.ins-det].

[57] A. Andronic, P. Braun-Munzinger, and J. Stachel. “Hadron production in central nucleus-nucleus collisions at chemical freeze-out”. In: Nucl. Phys. A 772 (2006), pp. 167–199. DOI: 10.1016/j.nuclphysa.2006.03.012. arXiv: nucl-th/0511071.

[58] F. Becattini, J. Manninen, and M. Gazdzicki. “Energy and system size dependence of chemical freeze-out in relativistic nuclear collisions”. In: Phys. Rev. C73 (2006), p. 044905. DOI: 10.1103/PhysRevC.73.044905. arXiv: hep-ph/0511092 [hep-ph].

[59] Katarzyna Grebieszkow. “NA49 and NA61/SHINE experiments: Results and perspectives”. In: Acta Phys. Polon. B 41 (2010). Ed. by Marek Pfutzner and Tomasz Matulewicz, pp. 427–440. arXiv: 0911.1902 [nucl-ex].

[60] J. Cleymans et al. “Comparison of chemical freeze-out criteria in heavy-ion collisions”. In: Phys. Rev. C 73 (2006), p. 034905. DOI: 10.1103/PhysRevC.73.034905. arXiv: hep-ph/0511094.

[61] N. Abgrall et al. “NA61/SHINE facility at the CERN SPS: beams and detector system”. In: JINST 9.CERN-PH-EP-2014-003. CERN-PH-EP-2014-003 (Jan. 2014), P06005. 55 p. DOI: 10.1088/1748-0221/9/06/P06005. URL: https://cds.cern.ch/record/1642156.

[62] M. Gazdzicki. “The Mixed Phase Collision Energy Range from the Experimental Data”. In: Acta Phys. Polon. B 45.12 (2014). Ed. by Michal Praszalowicz, p. 2319. DOI: 10.5506/APhysPolB.45.2319.

[63] Marek Gazdzicki and Peter Seyboth. “Search for Critical Behaviour of Strongly Interacting Matter at the CERN Super Proton Synchrotron”. In: Acta Phys. Polon. B 47 (2016), p. 1201. DOI: 10.5506/APhysPolB.47.1201. arXiv: 1506.08141 [nucl-ex].

[64] Maja Maćkowiak-Pawłowska. “Higher order moments of net-charge and multiplicity distributions in $p+p$ interactions at SPS energies from NA61/SHINE”. In: Acta Phys. Polon. Supp. 10 (2017), pp. 657–661. DOI: 10.5506/APhysPolBSupp.10.657. arXiv: 1610.03838 [nucl-ex].

[65] M. I. Gorenstein and M. Gazdzicki. “Strongly Intensive Quantities”. In: Phys. Rev. C 84 (2011), p. 014904. DOI: 10.1103/PhysRevC.84.014904. arXiv: 1101.4865 [nucl-th].

[66] Henning Heiselberg and Anne-Marie Levy. “Elliptic flow and HBT in noncentral nuclear collisions”. In: Phys. Rev. C 59 (1999), pp. 2716–2727. DOI: 10.1103/PhysRevC.59.2716. arXiv: nucl-th/9812034.

[67] A. Bialas, M. Bleszynski, and W. Czyz. “Multiplicity Distributions in Nucleus-Nucleus Collisions at High-Energies”. In: Nucl. Phys. B 111 (1976), pp. 461–476. DOI: 10.1016/0550-3213(76)90329-1.

[68] Szymon Pulawski. “Highlights from the NA61/SHINE”. In: EPJ Web Conf. 276 (2023), p. 01004. DOI: 10.1051/epjconf/202327601004.

[69] T. Anticic et al. “Measurement of event-by-event transverse momentum and multiplicity fluctuations using strongly intensive measures $\Delta[P_T, N]$ and $\Sigma[P_T, N]$ in nucleus-nucleus collisions at the CERN Super Proton Synchrotron”. In: Phys. Rev. C 92.4 (2015), p. 044905. DOI: 10.1103/PhysRevC.92.044905. arXiv: 1509.04633 [nucl-ex].

[70] A. Aduszkiewicz et al. “Multiplicity and transverse momentum fluctuations in inelastic proton–proton interactions at the CERN Super Proton Synchrotron”. In: Eur. Phys. J. C 76.11 (2016), p. 635. DOI: 10.1140/epjc/s10052-016-4450-9. arXiv: 1510.00163 [hep-ex].

[71] H. Adhikary et al. “Measurements of two-pion HBT correlations in Be+Be collisions at 150A GeV/c beam momentum, at the NA61/SHINE experiment at CERN”. In: (Feb. 2023). arXiv: 2302.04593 [nucl-ex].

[72] J. C. Vassilicos, ed. Intermittency in Turbulent Flows. Nov. 2000.

[73] A. Bialas and Robert B. Peschanski. “Moments of Rapidity Distributions as a Measure of Short Range Fluctuations in High-Energy Collisions”. In: Nucl. Phys. B 273 (1986), pp. 703–718. DOI: 10.1016/0550-3213(86)90386-X.

[74] Helmut Satz. “Intermittency and Critical Behavior”. In: Nucl. Phys. B 326 (1989), pp. 613–618. DOI: 10.1016/0550-3213(89)90546-4.

[75] N. G. Antoniou et al. “Intermittency, Kadanoff Scaling and Hadronization”. In: Phys. Lett. B 245 (1990), pp. 619–623. DOI: 10.1016/0370-2693(90)90701-7.

[76] A. Bialas and R.C. Hwa. “Intermittency parameters as a possible signal for quark - gluon plasma formation”. In: Phys.Lett. B253 (1991), pp. 436–438. DOI: 10.1016/0370-2693(91)91747-J.

[77] Wolfgang Ochs and Jacek Wosiek. “Intermittency and Other Correlation Phenomena in High-energy Collisions”. In: Phys. Lett. B 232 (1989), pp. 271–277. DOI: 10.1016/0370-2693(89)91700-0.

[78] T. Anticic et al. “Critical fluctuations of the proton density in A+A collisions at 158A GeV”. In: Eur. Phys. J. C 75.12 (2015), p. 587. DOI: 10.1140/epjc/s10052-015-3738-5. arXiv: 1208.5292 [nucl-ex].

[79] H. Adhikary et al. “Search for the critical point of strongly-interacting matter in ^{40}Ar + ^{45}Sc collisions at 150A GeV/c using scaled factorial moments of protons”. In: (May 2023). arXiv: 2305.07557 [nucl-ex].

[80] Haradhan Adhikary. “Search for the critical point of strongly interacting matter (Intermittency analysis by NA61/SHINE at CERN SPS)”. In: EPJ Web Conf. 274 (2022), p. 06008. DOI: 10.1051/epjconf/202227406008. arXiv: 2211.10504 [hep-ex].

[81] Haradhan Adhikary. “Search for the QCD critical point by NA61/SHINE at the CERN SPS”. In: 10th International Conference on New Frontiers in Physics. Aug. 2023. arXiv: 2308.04254 [nucl-ex].

[82] Benoit B. Mandelbrot. “Intermittent turbulence in self-similar cascades: divergence of high moments and dimension of the carrier”. In: J. Fluid Mech. 62.2 (1974), pp. 331–358. DOI: 10.1017/s0022112074000711.

[83] J Wosiek. “Intermittency in the Ising systems”. In: Acta Physica Polonica, Series B 19.10 (1988), pp. 863–866.

[84] Tobiasz Czopowicz. “Search for critical point via intermittency analysis in NA61/SHINES”. In: PoS CPOD2021 (2021), p. 039. DOI: 10.22323/1.400.0039.

[85] A. Bialas and M. Gazdzicki. “A New variable to study intermittency”. In: Phys. Lett. B 252 (1990), pp. 483–486. DOI: 10.1016/0370-2693(90)90575-Q.

[86] Won-Gi Paeng et al. “Scale-invariant hidden local symmetry, topology change, and dense baryonic matter. II.” In: Phys. Rev. D 96.1 (2017), p. 014031. DOI: 10.1103/PhysRevD.96.014031. arXiv: 1704.02775 [nucl-th].

[87] E. A. De Wolf, I. M. Dremin, and W. Kittel. “Scaling laws for density correlations and fluctuations in multiparticle dynamics”. In: Phys. Rept. 270 (1996), pp. 1–141. DOI: 10.1016/0370-1573(95)00069-0. arXiv: hep-ph/9508325.

[88] N. G. Antoniou et al. “Critical opalescence in baryonic QCD matter”. In: Phys. Rev. Lett. 97 (2006), p. 032002. DOI: 10.1103/PhysRevLett.97.032002. arXiv: hep-ph/0602051 [hep-ph].

[89] I. Derado et al. “Investigation of Intermittency in Muon - Proton Scattering at 280-GeV”. In: Z. Phys. C 47 (1990), pp. 23–30. DOI: 10.1007/BF01551907.

[90] I. V. Ajinenko et al. “Intermittency Effects in π^+P and K^+P Collisions at 250-GeV/c”. In: Phys. Lett. B 235 (1990), pp. 373–378. DOI: 10.1016/0370-2693(90)91981-G.

[91] Roman Holynski et al. “Evidence for Intermittent Patterns of Fluctuations in Particle Production in High-Energy Interactions in Nuclear Emulsion”. In: Phys. Rev. Lett. 62 (1989), pp. 733–736. DOI: 10.1103/PhysRevLett.62.733.

[92] R. Holynski et al. “One-dimensional and Two-dimensional Analysis of the Factorial Moments in 200-GeV/nucleon P, ^{16}O and ^{32}S Interactions With Ag / Br Nuclei”. In: Phys. Rev. C 40 (1989), R2449–R2453. DOI: 10.1103/PhysRevC.40.R2449.

[93] A. Bialas and J. Seixas. “Strong intermittency in momentum space”. In: Phys. Lett. B 250 (1990), pp. 161–163. DOI: 10.1016/0370-2693(90)91172-8.

[94] K. H. Kampert et al. “Recent results from the WA80 experiment at CERN”. In: Nucl. Phys. A 544 (1992). Ed. by T. C. Awes et al., pp. 183C–196C. DOI: 10.1016/0375-9474(92)90573-3.

[95] Marek Gaździcki et al. “Recent results from NA35”. In: Nucl. Phys. A 590 (1995). Ed. by Arthur M. Poskanzer, J. W. Harris, and L. S. Schroeder, pp. 197C–213C. DOI: 10.1016/0375-9474(95)00236-T.

[96] R. Albrecht et al. “Intermittency and correlations in 200-GeV/nucleon S + S and S + Au collisions”. In: Phys. Rev. C 50 (1994), pp. 1048–1064. DOI: 10.1103/PhysRevC.50.1048.

[97] J. Bächler et al. “An Investigation of intermittency in proton - gold, oxygen - gold, sulfur - gold and sulfur-sulfur interactions at 200-GeV per nucleon”. In: Z. Phys. C 61 (1994), pp. 551–562. DOI: 10.1007/BF01552621.

[98] M. A. Stephanov. "Non-Gaussian fluctuations near the QCD critical point". In: Phys. Rev. Lett. 102 (2009), p. 032301. DOI: 10.1103/PhysRevLett.102.032301. arXiv: 0809.3450 [hep-ph].

[99] Jacek Wosiek. "Intermittency in the Ising Systems". In: Acta Phys. Polon. B19 (1988), pp. 863–866.

[100] N. G. Antoniou et al. "Critical QCD in nuclear collisions". In: Nucl. Phys. A 761 (2005), pp. 149–161. DOI: 10.1016/j.nuclphysa.2005.07.003. arXiv: hep-ph/0505185.

[101] Michael Buballa. "NJL model analysis of quark matter at large density". In: Phys. Rept. 407 (2005), pp. 205–376. DOI: 10.1016/j.physrep.2004.11.004. arXiv: hep-ph/0402234.

[102] Mark G. Alford, Krishna Rajagopal, and Frank Wilczek. "QCD at finite baryon density: Nucleon droplets and color superconductivity". In: Phys. Lett. B 422 (1998), pp. 247–256. DOI: 10.1016/S0370-2693(98)00051-3. arXiv: hep-ph/9711395.

[103] Y. Hatta and M. A. Stephanov. "Proton number fluctuation as a signal of the QCD critical endpoint". In: Phys. Rev. Lett. 91 (2003). [Erratum: Phys.Rev.Lett. 91, 129901 (2003)], p. 102003. DOI: 10.1103/PhysRevLett.91.102003. arXiv: hep-ph/0302002.

[104] Misha A. Stephanov, K. Rajagopal, and Edward V. Shuryak. "Signatures of the tricritical point in QCD". In: Phys. Rev. Lett. 81 (1998), pp. 4816–4819. DOI: 10.1103/PhysRevLett.81.4816. arXiv: hep-ph/9806219.

[105] P. Bozek and M. Ploszajczak. "Finite size effect in intermittency". In: Phys. Lett. B 264 (1991), pp. 204–206. DOI: 10.1016/0370-2693(91)90728-9.

[106] N. G. Antoniou et al. "Locating the QCD critical endpoint through finite-size scaling". In: Phys. Rev. D 97.3 (2018), p. 034015. DOI: 10.1103/PhysRevD.97.034015. arXiv: 1705.09124 [hep-ph].

[107] Subhasis Samanta, Tobiasz Czopowicz, and Marek Gazdzicki. "Impact of momentum resolution on factorial moments due to power–law correlations between particles". In: J. Phys. G 48.10 (2021), p. 105106. DOI: 10.1088/1361-6471/ac2312. arXiv: 2105.01763 [nucl-th].

[108] Wolfgang Ochs and Jacek Wosiek. “Intermittency and Jets”. In: Phys. Lett. B 214 (1988), pp. 617–620. DOI: 10.1016/0370-2693(88)90131-1.

[109] Wolfgang Ochs. “The importance of phase space dimension in the intermittency analysis of multi - hadron production”. In: Phys. Lett. B 247 (1990), pp. 101–106. DOI: 10.1016/0370-2693(90)91056-H.

[110] T. Anticic et al. “Search for the QCD critical point in nuclear collisions at the CERN SPS”. In: Phys. Rev. C 81 (2010), p. 064907. DOI: 10.1103/PhysRevC.81.064907. arXiv: 0912.4198 [nucl-ex].

[111] “Energy Dependence of Intermittency for Charged Hadrons in Au+Au Collisions at RHIC”. In: (Jan. 2023). arXiv: 2301.11062 [nucl-ex].

[112] Jin Wu et al. “Probing QCD critical fluctuations from intermittency analysis in relativistic heavy-ion collisions”. In: Phys. Lett. B 801 (2020), p. 135186. DOI: 10.1016/j.physletb.2019.135186. arXiv: 1901.11193 [nucl-th].

[113] Jin Wu et al. “Intermittency analysis of proton numbers in heavy-ion collisions at energies available at the BNL Relativistic Heavy Ion Collider”. In: Phys. Rev. C 104.3 (2021), p. 034902. DOI: 10.1103/PhysRevC.104.034902. arXiv: 2104.11524 [nucl-th].

[114] Jin Wu. “Measurement of Intermittency for Charged Particles in Au + Au Collisions at $\sqrt{s_{\mathrm{NN}}}$ = 7.7-200 GeV from STAR”. In: SciPost Phys. Proc. 10 (2022), p. 041. DOI: 10.21468/SciPostPhysProc.10.041. arXiv: 2110.09794 [nucl-ex].

[115] Pengcheng Li et al. “Proton correlations and apparent intermittency in the UrQMD model with hadronic potentials”. In: Phys. Lett. B 818 (2021), p. 136393. DOI: 10.1016/j.physletb.2021.136393. arXiv: 2104.08483 [nucl-th].

[116] Somen Gope and Buddhdeb Bhattacharjee. “Signature of intermittency in hybrid UrQMD-hydro data at 10 AGeV Au+Au collisions”. In: Eur. Phys. J. A 57.2 (2021), p. 44. DOI: 10.1140/epja/s10050-021-00361-7. arXiv: 2008.01943 [nucl-th].

[117] Salman Khurshid Malik and Ramni Gupta. “Intermittency analysis of charged hadrons generated in Pb-Pb collisions at $\sqrt{s_{NN}}$= 2.76 TeV and 5.02 TeV using PYTHIA8/Angantyr”. In: 51st International Symposium on Multiparticle Dynamics. Oct. 2022. arXiv: 2210.07942 [nucl-ex].

[118] Pranjal Sarma and Buddhadeb Bhattacharjee. “Color reconnection as a possible mechanism of intermittency in the emission spectra of charged particles in PYTHIA-generated high-multiplicity pp collisions at energies available at the CERN Large Hadron Collider”. In: Phys. Rev. C 99.3 (2019), p. 034901. DOI: 10.1103/PhysRevC.99.034901. arXiv: 1902.09124 [hep-ph].

[119] B. Efron. “Bootstrap Methods: Another Look at the Jackknife”. In: Annals Statist. 7.1 (1979), pp. 1–26. DOI: 10.1214/aos/1176344552.

[120] Subhasis Samanta, Tobiasz Czopowicz, and Marek Gazdzicki. “Scaling of factorial moments in cumulative variables”. In: Nucl. Phys. A 1015 (2021), p. 122299. DOI: 10.1016/j.nuclphysa.2021.122299. arXiv: 2105.00344 [nucl-th].

[121] B. Wosiek. “Intermittency analysis of correlated data”. In: Acta Phys. Polon. B 21 (1990), pp. 1021–1030.

[122] Marek Gazdzicki et al. Hadron production in hadron-nucleus and nucleus-nucleus collisions. Tech. rep. Geneva: CERN, Nov. 2006. URL: http://cds.cern.ch/record/995681.

[123] K. Abe et al. “The T2K Experiment”. In: Nucl. Instrum. Meth. A 659 (2011), pp. 106–135. DOI: 10.1016/j.nima.2011.06.067. arXiv: 1106.1238 [physics.ins-det].

[124] Michael Unger. “New Results from the Cosmic-Ray Program of the NA61/SHINE facility at the CERN SPS”. In: PoS ICRC2019 (2020), p. 446. DOI: 10.22323/1.358.0446. arXiv: 1909.07136 [astro-ph.HE].

[125] A Aduszkiewicz. Report from the NA61/SHINE experiment at the CERN SPS. Tech. rep. CERN-SPSC-2018-029. SPSC-SR-239. Geneva: CERN, Oct. 2018. URL: https://cds.cern.ch/record/2642286.

[126] PIOTR PODLASKI PhD Thesis at https://edms.cern.ch/document/2680143/1.

[127] A Aduszkiewicz. Report from the NA61/SHINE experiment at the CERN SPS. Tech. rep. CERN-SPSC-2016-038 ; SPSC-SR-197. Geneva: CERN, Oct. 2016. URL: http://dx.doi.org/10.17181/CERN.SD0Z.RJ9V.

[128] D. Banas et al. "Influence of target material impurities on physical results in relativistic heavy-ion collisions". In: Eur. Phys. J. Plus 134.1 (2019), p. 44. DOI: 10.1140/epjp/i2019-12465-9. arXiv: 1808.10377 [nucl-ex].

[129] Diego Victor Babos, Vinicius Câmara Costa, and Edenir Rodrigues Pereira-Filho. "Wavelength dispersive X-ray fluorescence (WD-XRF) applied to speciation of sulphur in mineral supplement for cattle: Evaluation of the chemical and matrix effects". In: Microchemical Journal 147 (2019), pp. 628–634. ISSN: 0026-265X. DOI: https://doi.org/10.1016/j.microc.2019.03.077. URL: https://www.sciencedirect.com/science/article/pii/S0026265X18315303.

[130] P. A. Zyla et al. "Review of Particle Physics". In: PTEP 2020.8 (2020), p. 083C01. DOI: 10.1093/ptep/ptaa104.

[131] M. Golubeva et al. "Hadron Calorimeter (Projectile Spectator Detector—PSD) of NA61/SHINE experiment at CERN". In: KnE Energ. Phys. 3 (2018), pp. 379–384. DOI: 10.18502/ken.v3i1.1770.

[132] A. Seryakov. PSD acceptance maps for event selection. https://edms.cern.ch/document/1867336/1. note. CERN EDMS. 2017.

[133] Sergey Morozov et al. "Forward hadron calorimeter (PSD) of NA61/SHINE for heavy ion studies and its upgrade for experiments beyond 2020". In: PoS CORFU2018 (2019). Ed. by Konstantinos Anagnostopoulos et al., p. 195. DOI: 10.22323/1.347.0195.

[134] N. Abgrall et al. "Calibration and analysis of the 2007 data". In: (July 2008).

[135] Haradhan Adhikary. Proton intermittency analysis note (under review to submit CERN EDMS). Tech. rep. Geneva: NA61/SHINE at CERN SPS. URL: https://indico.cern.ch/event/1318414/.

[136] A. Acharya et al. “Measurements of π^- production in ^{7}Be+^{9}Be collisions at beam momenta from 19A to 150AGeV/c in the NA61/SHINE experiment at the CERN SPS”. In: Eur. Phys. J. C 80.10 (2020). [Erratum: Eur.Phys.J.C 81, 144 (2021)], p. 961. DOI: 10.1140/epjc/s10052-020-08514-6. arXiv: 2008.06277 [nucl-ex].

[137] A. Acharya et al. “Spectra and mean multiplicities of π^- in central^{40}Ar+^{45}Sc collisions at 13A, 19A, 30A, 40A, 75A and 150A Ge V/c beam momenta measured by the NA61/SHINE spectrometer at the CERN SPS”. In: Eur. Phys. J. C 81.5 (2021), p. 397. DOI: 10.1140/epjc/s10052-021-09135-3. arXiv: 2101.08494 [hep-ex].

[138] ANDREY SERYAKOV. PSD acceptance maps for event selection. Tech. rep. Geneva: CERN. URL: https://edms.cern.ch/document/1867336/1.

[139] Piotr Bożek et al. “GLISSANDO 3: GLauber Initial-State Simulation AND mOre..., ver. 3”. In: Comput. Phys. Commun. 245 (2019), p. 106850. DOI: 10.1016/j.cpc.2019.07.014. arXiv: 1901.04484 [nucl-th].

[140] H. Adhikary et al. “Measurements of $\pi^{\pm}$, $K^{\pm}$, p and $\bar{p}$ spectra in ^{40}Ar+^{45}Sc collisions at 13A to 150A GeV/c”. In: (Aug. 2023). arXiv: 2308.16683 [nucl-ex].

[141] N. G. Antoniou et al. “Critical events and intermittency in nuclear collisions”. In: Phys. Lett. B 432 (1998), pp. 8–14. DOI: 10.1016/S0370-2693(98)00629-7.

[142] NA61/SHINE acceptance map available at https://edms.cern.ch/document/2778197.

[143] K. Werner et al. “The Physics of EPOS”. In: EPJ Web Conf. 52 (2013), p. 05001. DOI: 10.1051/epjconf/20125205001.

[144] Klaus Werner. “The hadronic interaction model EPOS”. In: Nucl. Phys. Proc. Suppl. 175-176 (2008), pp. 81–87. DOI: 10.1016/j.nuclphysbps.2007.10.012.

[145] T. Czopowicz, in preparation.

[146] R. Brun et al. “GEANT3”. In: (Sept. 1987).